Spring 2014

Impact of fracture spacing and mechanical parameter anisotropy on fracture width in horizontal wells in shales

Deepak Gokaraju

Department:

Recommended Citation

Gokaraju, Deepak, "Impact of fracture spacing and mechanical parameter anisotropy on fracture width in horizontal wells in shales" (2014). *Masters Theses*. 7253.
https://scholarsmine.mst.edu/masters_theses/7253

IMPACT OF FRACTURE SPACING AND MECHANICAL PARAMETER ANISOTROPY ON FRACTURE WIDTH IN HORIZONTAL WELLS IN SHALES

by

DEEPAK GOKARAJU

A THESIS

Presented to the Faculty of the Graduate School of the

MISSOURI UNIVERSITY OF SCIENCE AND TECHNOLOGY

In Partial Fulfillment of the Requirements for the Degree

MASTER OF SCIENCE IN MECHANICAL ENGINEERING

2014

Approved by

Andreas Eckert, Advisor
Runnar Nygaard
Shari Dunn-Norman

ABSTRACT

The success of economically viable production of oil and gas from ultra-low permeability shale reservoirs depends on the creation of an extensive fracture network through hydraulic fracture stimulation. Multiple hydraulic fractures are created simultaneously in each stage to increase the surface area of contact between the wellbore and reservoir. The spacing between fractures is an important component to consider when developing an optimum stimulation design. An important aspect of shale rock properties is that shales are inherently anisotropic with a horizontal plane of isotropy (transversely isotropic) due to their finely layered structure. This study aims to provide an insight into the controlling effects of fracture spacing and different levels of rock property anisotropy on the fracture aperture during simultaneous fracture initiation and propagation. Multiple fracture propagation is simulated using 3-dimensional [3D] finite element models [FEM].

All simulations in this study include simultaneous propagation of four fractures in pre-defined planes using cohesive elements in a linear elastic medium. Numerous FEMs with varying spacing between fractures and varying levels of anisotropy are generated to analyze the effect of spacing and rock anisotropy on the fracture apertures. The modeling results show that there is a significant fracture width reduction in the center fractures when compared to the edge fractures across the entire range of fracture spacing included in the study. Previous studies present analyses on the effect of anisotropy on fractures whereas this study further investigates the individual effect of anisotropy on the edge fractures and center fractures. It can be taken further to simulate production rates and cumulative production over time and hence can be used as a guideline for different shale plays.

ACKNOWLEDGMENTS

I would like to express my gratitude to my advisor, Dr. Andreas Eckert, for his excellent guidance, support, patience and above all his belief in me. I would like to thank him for accepting me into his geomechanical modeling research group which has been a great learning experience over the past few years. His advice that often extends to practical issues beyond textbooks and financial support proved to be invaluable for the successful completion of this study. I would also like to extend my thanks to Dr. Nygaard and Dr. Dunn-Norman.

I would like to thank everyone in the geomechanical modeling group particularly Nevan Himmelberg, Xiaolong Liu, Amin Amirlatifi, Mengke Li for the many intellectually stimulating discussions and for their assistance both at work and outside of it. I am grateful to this modeling group for creating an inspiring research environment.

My deepest heartfelt appreciation goes to my brother, Ravi Gokaraju for his continuous guidance, motivation and for standing by me at all times. Without his support, a graduate degree would still remain a dream for me. I would also like to thank my parents, Indira and G.S.N. Raju, for their contribution. I would also like to thank all my friends, particularly Chaitanya Tanna who made my stay in Rolla enjoyable and very memorable.

TABLE OF CONTENTS

LIST OF ILLUSTRATIONS

Figure Page

LIST OF TABLES

1. INTRODUCTION

1.1. BACKGROUND AND LITERATURE REVIEW

Commercial production of hydrocarbons from tight shale reservoirs was considered to not be economically viable until recent advances in drilling technology and hydraulic fracturing. Hydraulic fracturing is a method of stimulating production from the well by perforating the formation at an intended depth and pumping fluid into the wellbore at a high volume rate until the perforated cracks propagate into large fractures to increase contact surface area for flow into the wellbore. The injection volume rate is maintained for a certain period of time until the fracture reaches the intended size and geometry. A good understanding of fracture mechanics based on the knowledge of reservoir rock properties, fracturing fluid and in-situ stress conditions is required to accurately predict the dimensions (height, width and length) of a hydraulically induced fracture (Warpinski, 1991). Predicting the fracture dimensions accurately is an integral part of a successful and effective fracture design. A hydraulic fracture creates a pathway for fluids in a low or ultra-low permeability reservoir to freely flow into the wellbore which otherwise would have posed a challenge. A successful fracture design not only enhances production rates but also increases the cumulative production of hydrocarbons produced from shale formations.

Unconventional oil and gas reservoirs like shale formations are developed by creating multiple fractures in a horizontal well that could extend up to several thousand feet. Usually, four to six fractures are created simultaneously in each stage and there could be up to 40 – 50 stages to fully develop the reservoir as shown in Figure 1.1. The created fractures may be longitudinal or transverse with respect to the horizontal wellbore (Wei and Economides, 2005). This study focuses on transverse fractures as they are more effective in draining low permeability reservoirs compared to longitudinal fractures because of the increased contact area with the reservoir (Economides, 2007). Previous studies proposed that there is a direct relation between the number of fractures and ultimate production (Soliman et al., 1999) and that decreasing fracture spacing (thereby increasing the number of fractures) increases the overall productivity of the well although the productivity of each fracture is reduced (Ozkan, 2011). However, there is no substantial evidence to back these studies. In fact, recent work on stimulation monitoring using micro-seismic monitoring, fiber optics temperature and strain sensing observe that multiple fractures do not grow and develop as expected and that more than 25% of the fractures created in general are ineffective to production (Sierra 2008; Molenaar et al. 2012). There is a need to better understand the interaction between multiple fractures to optimize the fracture design and to provide better value for the costs involved.

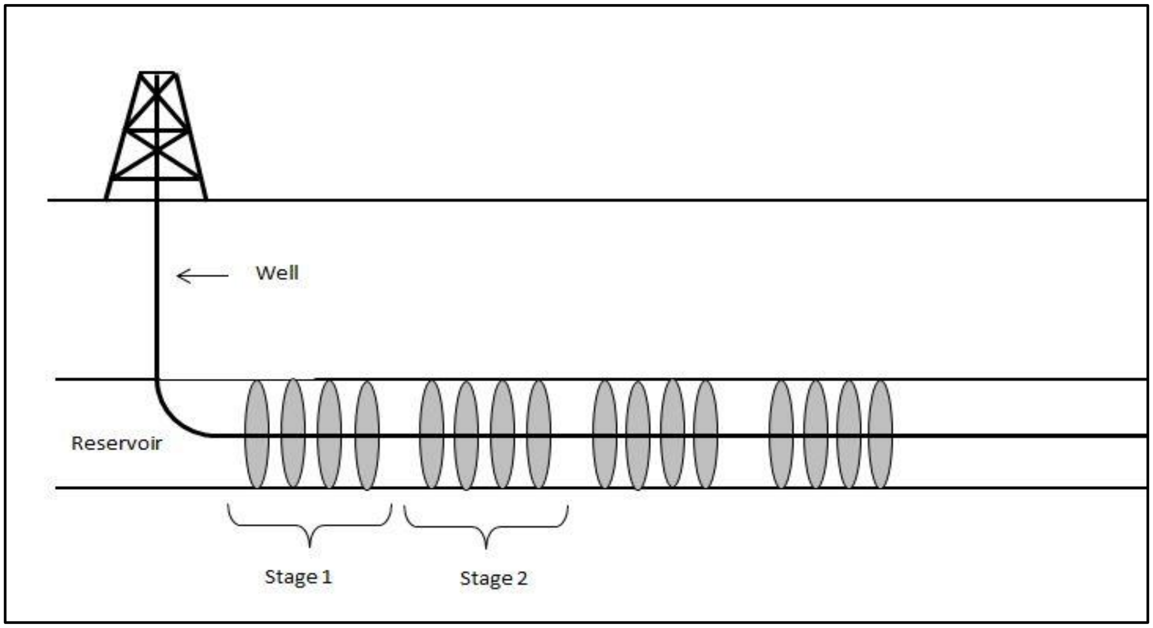

Figure 1.1. Multiple fractures are created in stages where four to six fractures are created per stage

1.1.1. Fracture Spacing. Each fracture has an effect on the stress conditions around it. One of the early works provides an analytical solution to the stress changes around an elliptical induced fracture (Green and Sneddon 1950). The subsurface stress change in the surrounding area of a single fracture was studied based on the rock properties and the geometry of the fracture (Wood and Junki 1970). The formation stress change caused by a fracture is also called as a ‘stress shadow’ (Figure 1.2). The geometry of fractures formed within this ‘stress shadow’ is substantially affected. This phenomenon between multiple fractures was studied by several authors in various stages and scenarios of hydraulic fracturing (Soliman et al. 2008; Cheng 2009; Rafiee et al. 2012; Meyers et al. 2012). The formation stress change depends on the mechanical properties of the rock, the geometry of the rock and the pressure inside the fracture caused by the fracturing fluid (Warpinski 2004). The stress change is so profound in the near wellbore region around the fractures that in some cases, the directions of maximum and minimum horizontal stresses are reversed. This phenomenon is called the ‘stress reversal’ as shown in Figure 1.3. It means that any new fractures created in this area may be longitudinal before reorienting themselves away from the wellbore (Abass et al. 1996; Rafiee et al. 2012).

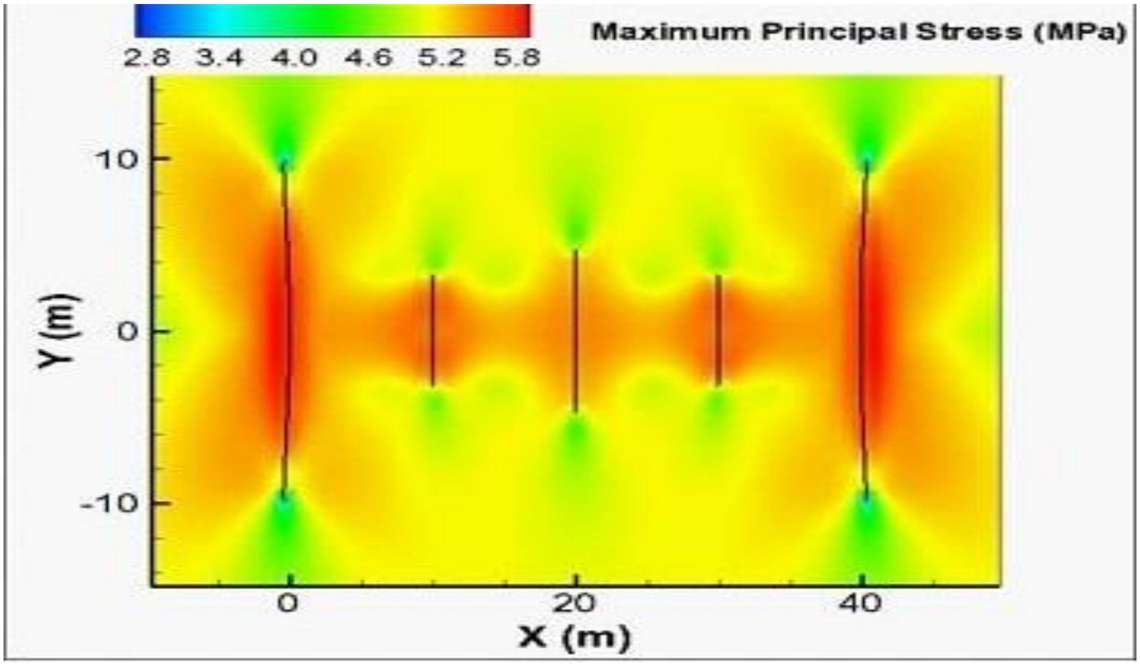

Figure 1.2. Areas around a fracture affected by stress called 'Stress Shadow' (after Ghassemi, 2013)

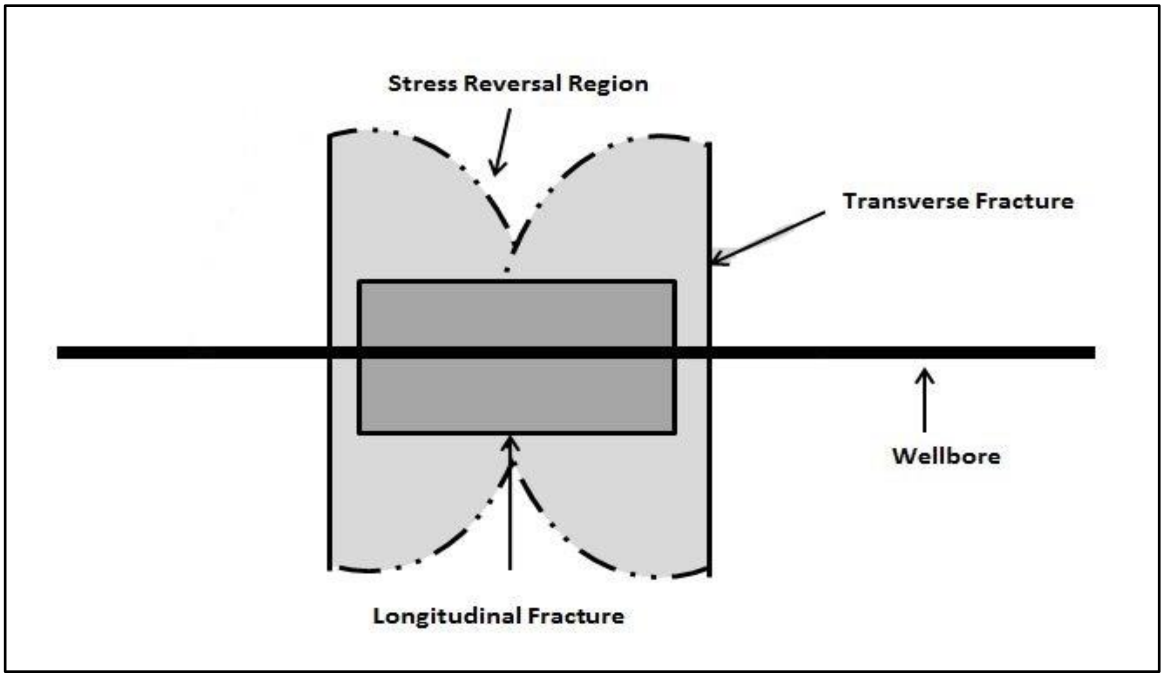

Figure 1.3. New fractures created in the 'stress reversal' region are of a different orientation

Fracture width is very important because the efficient transport of proppant, deep into the fracture, depends on it. Understanding the widths of simultaneously created transverse fracture is critical to the success of the fracture treatment design. Overestimating the fracture widths will result in choosing an oversized proppant that could lead to a premature screen out (Economides and Martin, 2007). Underestimating the fracture widths will result in choosing an undersized proppant. This affects the return on investment of the job as the created fracture width will not be propped effectively and due to the compressive horizontal subsurface stresses, the final fracture width ends up as a fraction of the initially created one.

The number of fractures in a horizontal wellbore section is closely related to the fracture spacing. Optimizing the fracture spacing is crucial as it affects the widths of each fracture and the number of fractures created. Cheng (2009) observes that when multiple fractures are created simultaneously, the edge fractures are relatively insensitive to fracture spacing and usually have the highest fracture widths as shown in Figures 1.4, 1.5 and 1.6. The center fracture widths are reduced significantly when compared to the edge fractures as shown in Figure 1.4. He performs an analysis on fracture width variations of both edge and center fractures depending on fracture spacing. Figure 1.5 and Figure 1.6 show the variations of fracture widths as observed by Cheng. In cases where five fractures are created simultaneously, the sub center fractures hold the smallest widths. The created fractures may not propagate in a single plane due to the stress interference caused by other fractures (Cheng, 2012).

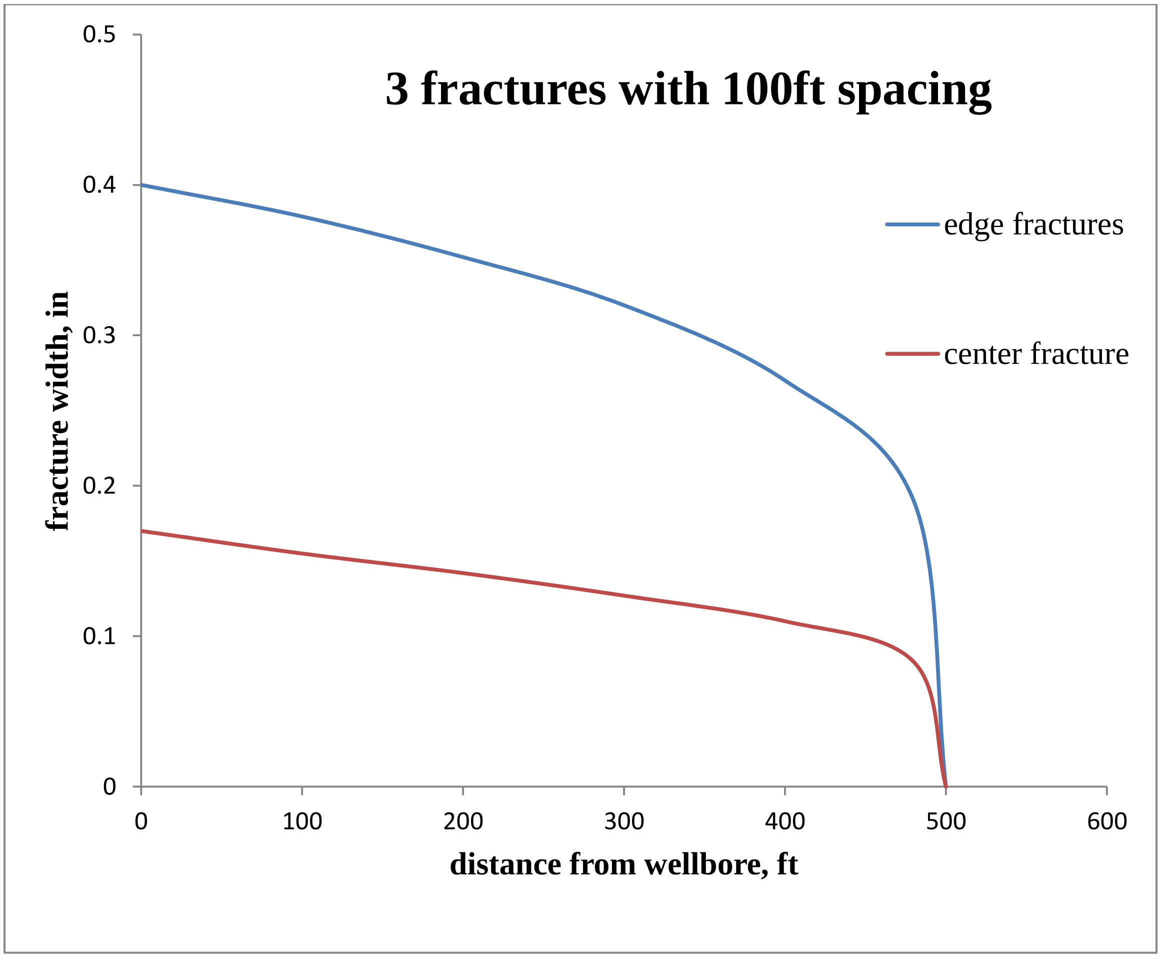

Figure 1.4. Fracture widths of three parallel fractures with a spacing of 100 ft (after Cheng, 2009)

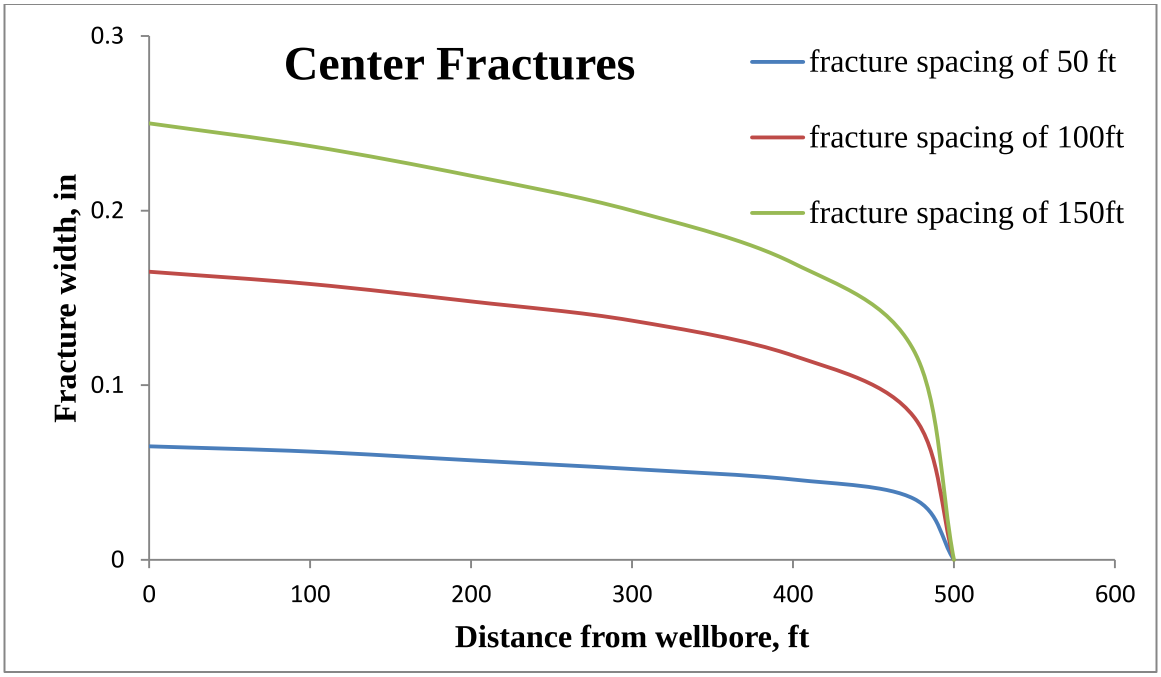

Figure 1.5. Comparison of center fracture widths of three parallel fractures with different spacing (after Cheng, 2009)

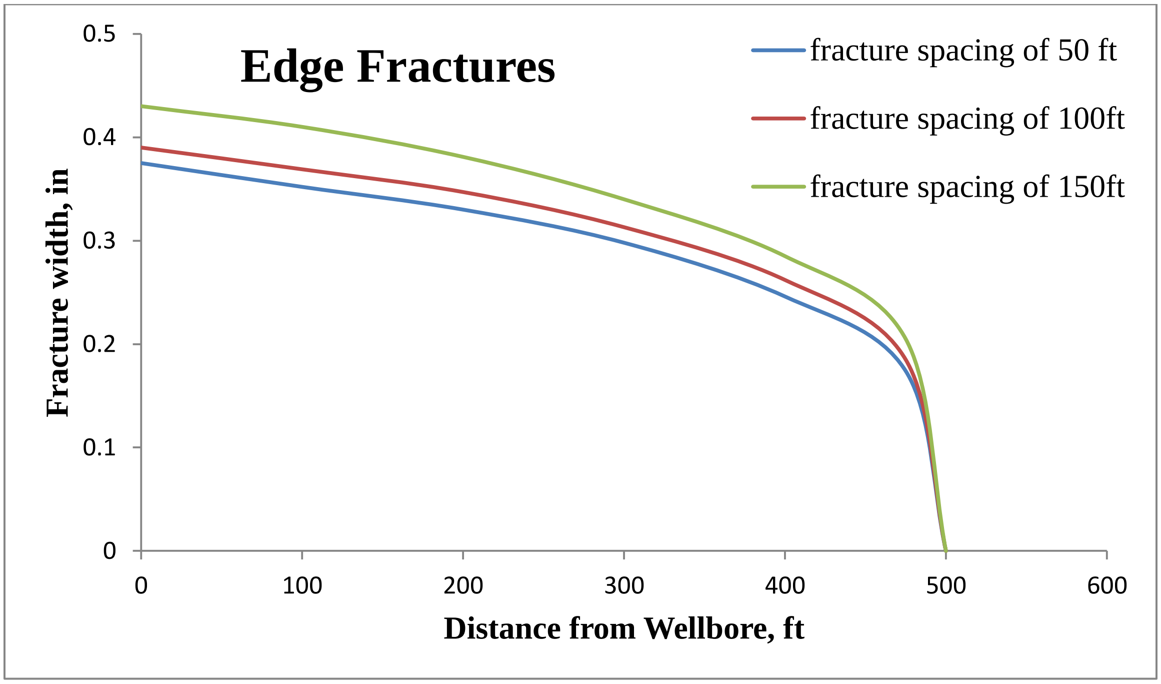

Figure 1.6. Comparison of edge fracture widths of three parallel fractures with different spacing (after Cheng, 2009)

1.1.2. Influence of Rock Anisotropy. Shales have an abundance of clay minerals in their matrix which are aligned by gravity as they are deposited. This alignment in clay and other minerals creates a fine scale layering. Due to this platy nature, shales are considered anisotropic where rock properties like permeability, acoustic velocity and elastic moduli vary with direction. If the shale formations are horizontal, the formations are described as transversely isotropic with a vertical axis of symmetry. Rock properties like permeability, Young's Modulus and Poisson's ratio are equal when measured in the horizontal directions but are different when measured in the vertical direction. Higgins (2008) and Sayers (2005) proposed an elastic tensor for transverse isotropy and a relationship between acoustic velocities and elastic moduli for transverse isotropy through the application of Hooks law. Waters (2011) notes that the transverse isotropy in shale formations depends on the clay type and clay content in its matrix.

Tight shales are strongly anisotropic and using isotropic models to predict fracture widths or fracture geometries could lead to inappropriate conclusions and poor production strategies (Suarez-Riviera et al., 2006, Khan, 2012). The permeability anisotropy effect on hydraulic fractures can be significant (Gatens, 1991; Holditch, 2005). Building a stress profile assuming isotropy would result in incorrectly predicting fracture barriers and fracture geometry used in overall completion design (Waters, 2011, Higgins, 2008) especially since anisotropic measurements are available from acoustical logging (Pabon, 2005). Khan (2012) uses a case study from the Horn River Basin in Canada to prove this point. Khan (2012) predicts the fracture geometry using both isotropic and anisotropic models and compares them with field data. The geometry predicted using anisotropic models are in line with the production data. The difference in the models is depicted in Figure 1.7. These results show that conventional equations related to hydraulic fracturing derived assuming isotropy are not adequate. Higher anisotropy ratios can be viewed as an advantage as they lower the fracture pressure and provide better fracture barriers (Khan, 2012). Chertov (2011) proposed an equation to predict the fracture width w based on net treating pressure taking anisotropy into account as shown in Equations 1 through 3.

$$w = h\sqrt{\frac{1-v_H^2}{2G_{VH}E_H}}\left(\sqrt{g_1 - h_1} + \sqrt{g_1 + h_1}\right) P_{net} \tag{1}$$

Where

$$g_1 = \left(1 - \frac{2G_{VH}}{E_V}(1 + v_H)v_V\right) \tag{2}$$

And

$$h_1 = \sqrt{1 - \frac{4G_{VH}}{E_V}(1 + v_H)v_V - \frac{4G_{VH}^2}{E_V E_H}(1 + v_H)\left(1 - v_H - 2\frac{E_H}{E_V}v_V^2\right)} \tag{3}$$

In comparison, the most commonly used equation to predict fracture widths in both the industry and academia is as mentioned in Equation 4.

$$w = \frac{2h(1 - v^2)}{E}P_{net} \tag{4}$$

Where w is the width of the fracture, h is the height of the fracture, E is the Young's Modulus, P_{net} is the net pressure, v is the Poisson's ratio, E_V is the Young's Modulus in the vertical direction, E_H is the Young's Modulus in the horizontal direction, G_{VH} is the shear modulus, v_H is the Poisson's ratio in the horizontal direction, v_V is the Poisson's ratio in the vertical direction. For calculations of fracture width when multiple fractures are present, the current practice is to divide the net treating pressure (P_{net}) by the number of fractures created simultaneously. This is because P_{net} is directly proportional to the volume of fluid injected (q) and equal fluid distribution between all fractures is assumed. Suarez-Riviera (2011) observed that fracture widths are dependent solely on the horizontal to vertical Young's Modulus ratio and not on the magnitude of the individual values.

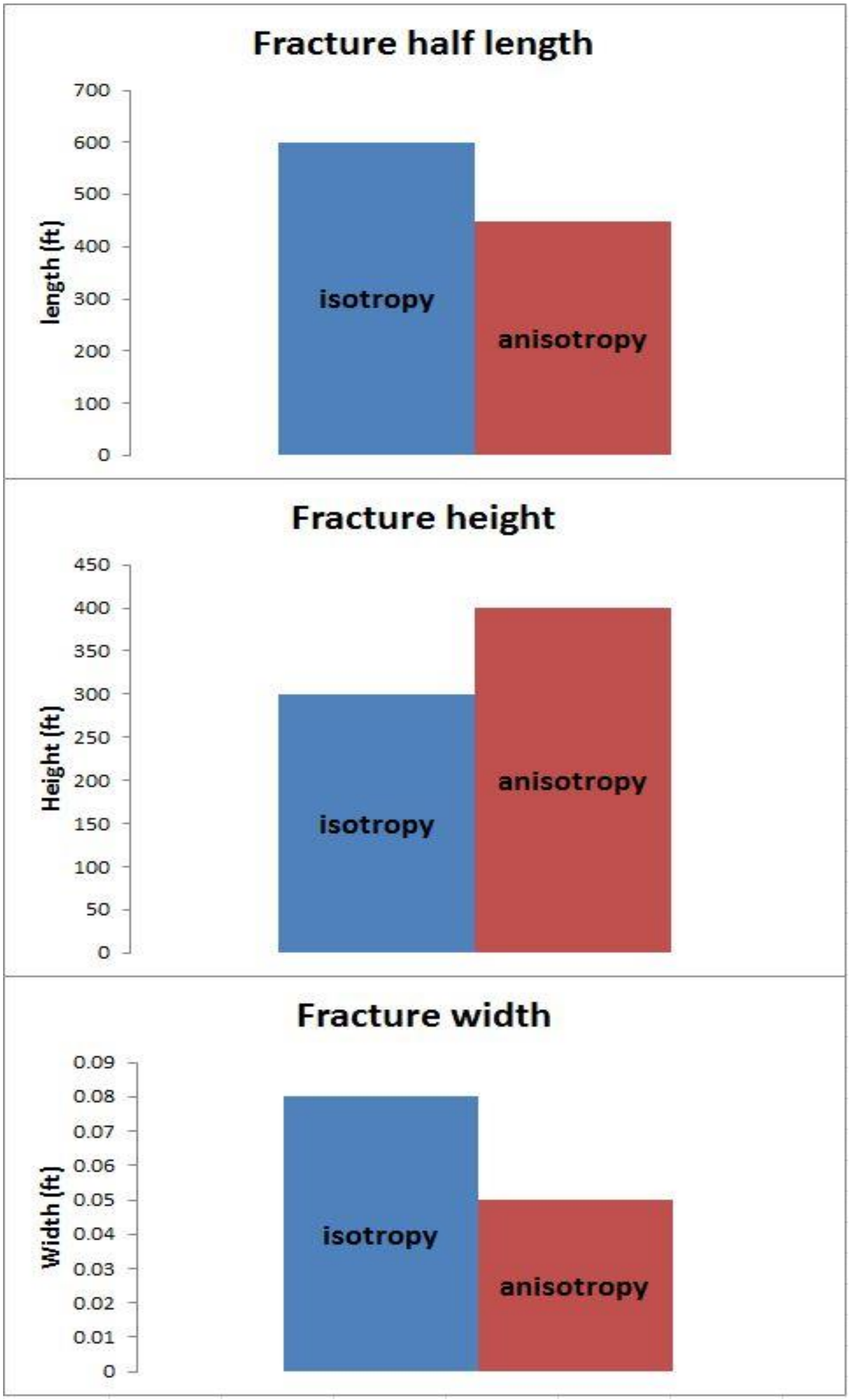

Figure 1.7. Difference in fracture geometry pedicted by isotropic and anisotropic models (after Khan, 2012)

1.2. CRITICAL REVIEW

Although extensive knowledge on different ways of hydraulic fracturing exists, there is a need to further enhance our knowledge on the relation between fracture spacing, rock property anisotropy and fracture width. Production from shales has a crucial role to play in meeting the ever increasing demand for energy. An important thing to note is that none of the shale plays are the same. The rock properties, rock response to various stress scenarios and the level of anisotropy differ from shale to shale. In this study, simulation of hydraulic fracturing is done via 3-Dimensional [3D] Finite Element Method [FEM]. Various 3D FEM numerical models are setup to simulate the creation of multiple hydraulic fractures simultaneously in a stage to investigate the factors controlling fracture width. The model uses cohesive elements to simulate the initiation and propagation of four hydraulic fractures in pre-defined fracture planes. The study uses generic 3D FEM models that are capable of showing the isolated influence of each parameter tested. The model setup can also be taken further to simulate the production rates and cumulative production of hydrocarbons after fracturing.

1.3. PURPOSE

This research investigates the controlling effects of fracture spacing and different levels of rock property anisotropy on the fracture aperture during simultaneous fracture initiation and propagation. A major objective of this research is to provide insight into the influence of fracture spacing on fracture aperture during simultaneous creation of fractures. Fracture spacing is increased in small intervals to analyze this effect. The second objective of this study is to provide insight into the influence of the varying ratio of rock property anisotropy (i.e. E, ν, k) on fracture apertures. Previous works present the consequences if anisotropy is neglected (Waters, 2011; Khan, 2012). This study additionally includes the individual effect property anisotropy has on the edge fractures and the center fractures. Due to the prevalence of different levels of anisotropy in different shale plays in the U.S, this study has a huge potential to be used as a guideline for the different shale plays.

2. THEORETICAL BACKGROUND

2.1. ROCK DESCRIPTION

The rock response to forces is the foundation of rock mechanics. All rocks have the ability albeit small to recover from deformations produced by external and internal forces. This characteristic of a material is called elasticity. For sufficiently small forces, the response of almost every material is linear. Linear elasticity is an important aspect of rock mechanics and failure related to Petroleum Engineering. The basic properties of rocks need to be understood first to have a clear understanding of rock responses and failure behavior related to hydraulic fracturing.

2.1.1. Rock Density. Rock density is defined as the amount of mass per unit volume. If ρ is the rock density in $\frac{\mathbf{kg}}{\boldsymbol{m^3}}$, M is the mass of the specimen of interest in kg and V is the volume in m3, the density is defined as:

$$\rho = \frac{M}{V} \tag{5}$$

Since porous materials may be partially or fully saturated with other fluids, other forms of density are commonly used for rock description. The most common of them is the bulk density. The bulk density (ρ_b) is defined as the ratio of the total mass (M_t) to the total volume (V_t) and is given in Equation 6.

$$\rho_b = \frac{M_t}{V_t} \tag{6}$$

The dry density (ρ_d) is defined as the density of the rock without any fluids occupying the pores of the rock. The dry density and the bulk density can be related using the pore fluid density (ρ_f) and the porosity (ϕ). The relationship is given in Equation 7 (Chapman, 1983).

$$\rho_b = (1 - \phi)\rho_d + \phi\rho_f \tag{7}$$

2.1.2. Porosity. Porosity is a measure of the pore spaces or void spaces in a rock. Porosity is defined as the ratio of the void space volume ($\boldsymbol{V_{void}}$) to the total volume ($\boldsymbol{V_{total}}$) as shown in Equation 8.

$$\phi = \frac{V_{void}}{V_{total}} \tag{8}$$

Another way of expressing the void space volume relative to the sample volume of the rock is the void ratio (e). It is the ratio of the void space volume (V_{void}**)** to the rock matrix volume (V_{matrix}).

$$e = \frac{V_{void}}{V_{matrix}} \tag{9}$$

Void ratio and porosity are related and the relationship can be derived by combining equation (8) and (9) and the resulting equation is given in Equation 10.

$$e = \frac{V_{void}}{V_{matrix}} = \frac{V_{void}}{V_{total} - V_{void}} = \frac{\frac{V_{void}}{V_{total}}}{1 - \frac{V_{void}}{V_{total}}} = \frac{\phi}{1 - \phi} \tag{10}$$

Not all pore spaces contribute to active fluid flow. Some of the pore spaces are interconnected and some are isolated. The percentage or ratio of pore spaces that actively contribute to fluid flow within the reservoir of the total pore spaces is known as the effective porosity. Another rock property that measures the ability of the rock to allow fluid flow is the permeability.

2.1.3. Rock Permeability. Permeability is a measure of the ability of a rock to transmit fluid flow through its pores. If only one fluid is present in the pore space, the permeability is known as the absolute permeability, if more than one fluid is present, permeability is measured using effective permeability of each of the immiscible fluids. Similar to permeability defined in Electrical engineering concepts, permeability represents the reciprocal of the resistance to flow offered by the medium. Darcy (1856) carried out experiments to investigate fluid flow through water. A simplified form of Darcy's law is given in Equation 11.

$$q = \frac{kA}{L\mu}(P_1 - P_2) \tag{11}$$

Where q is the flow rate of the fluid in $\frac{\mathrm{m}^3}{\mathrm{s}}$, A is the cross section area perpendicular to fluid flow direction in m^2, μ is the dynamic viscosity in Pa.s, k is the permeability in m^2, L is the length along the flow direction in m, and P1 and P_2 are the fluid pressures across both ends of the sample of length L in Pa.

Another way of measuring the rock's property that describes the ease with which a fluid can flow through its pores is by defining it in terms of 'Hydraulic conductivity' (K). The relationship between hydraulic conductivity (K) in $\frac{m}{s}$ and permeability (k) is given in Equation 12.

$$k = \frac{K\mu}{\rho_f g} \tag{12}$$

Where g is the acceleration due to gravity in $\frac{m}{s^2}$, and ρ_f is the density of the fluid. It should be noted here that the commonly used unit of permeability is darcy which has the dimensions of L_D^2 whereas the dimensions of hydraulic conductivity is L_D/T_D, where L_D is the length and T_D is the time in dimensions.

2.2. FUNDAMENTALS IN ROCK MECHANICS

The response of a material to forces by small deformations forms the basis of the theory of elasticity. A good understanding of stress and strain is necessary to understand the theory of elasticity.

2.2.1. Stress. For a resultant surface force F acting on an arbitrary surface of area A that is characterized by its unit normal vector ($\vec{\boldsymbol{n}}$), the traction is defined as shown in Equation 13.

$$\vec{T}\,(\vec{n}) = \frac{F}{A} \tag{13}$$

Traction is a measure of force intensity that acts at a point on an imaginary or a real surface of arbitrary orientation. Tractions are vector in nature. In order to define traction at a single point, a limit is imposed on Equation 13. Traction at a single point is defined as follows:

$$\vec{T}\,(\vec{n}) = \lim_{dA \to 0} \frac{d\vec{F}}{d\vec{A}} \tag{14}$$

Tractions, similar to surface forces, acting on a surface can be broken down into two components – shear and normal components. The traction component that acts along the surface is known as the shear traction. The one acting normal to the surface is called the normal traction.

Stress is also defined as a pressure or tension applied on a material i.e. force per unit area. Stresses represent a pair of equal and opposite tractions acting across a surface of specified orientation. Stresses are either compressive (a pair of tractions acting towards each other) or tensile in nature (acting away from each other). The mathematical definition of stress (σ) is given in Equation 15.

$$\sigma = \frac{F}{A} \tag{15}$$

The SI unit of stress is Pascal (N/m^2). It is also commonly expressed in psi (pounds per square inch) in the petroleum industry.

2.2.1.1 Stress tensor. The state of stress at a point is defined completely when all the traction vectors [$\vec{\boldsymbol{T}}$ ($\vec{\boldsymbol{n}}$)] associated with all the planes that pass through it are taken into account. This is achieved by the introduction of the Cauchy stress tensor. Nine stress components are required to fully describe the state of stress (SOS) at a point. The stress tensor is expressed as follows:

$$\sigma = \begin{pmatrix} \sigma_{xx} & \tau_{xy} & \tau_{xz} \\ \tau_{yx} & \sigma_{yy} & \tau_{yz} \\ \tau_{zx} & \tau_{zy} & \sigma_{zz} \end{pmatrix} \tag{16}$$

Where τ_{ij} is the shear stress acting on a surface normal to the 'i' direction and σ_{ii} is a normal stress acting perpendicular to a surface that is normal to the 'i' direction. The shear stress acting on a surface can be further divided into two components. For example, the shear stress acting on a surface normal to the x-direction can be broken down into τ_{xy} and τ_{xz} where τ_{xy} is the shear stress along the surface that is perpendicular to the z-direction and τ_{xz} is the shear stress along the surface that is perpendicular to the y-direction. The stress tensor illustration is shown in Figure 2.1. The SOS at a point and the resultant traction vector at that point are related as follows (Cauchy, 1827):

$$T_i = \sigma_{ij}.n_j \tag{17}$$

Where σ_{ij} is the stress tensor, T_i is the resultant traction vector and n_j is the unit normal vector passing through the plane.

2.2.1.2 Principal stresses. The SOS at a point can be expressed by choosing a particular coordinate system in which all the shear stresses vanish. Using this particular coordinate system, the SOS can be expressed purely in terms of the normal stresses perpendicular to each other. The remaining normal stresses are known as principal stresses. The stress tensor using the particular coordinate system is shown in Equation 18.

$$\sigma = \begin{pmatrix} \sigma_1 & 0 & 0 \\ 0 & \sigma_2 & 0 \\ 0 & 0 & \sigma_3 \end{pmatrix} \tag{18}$$

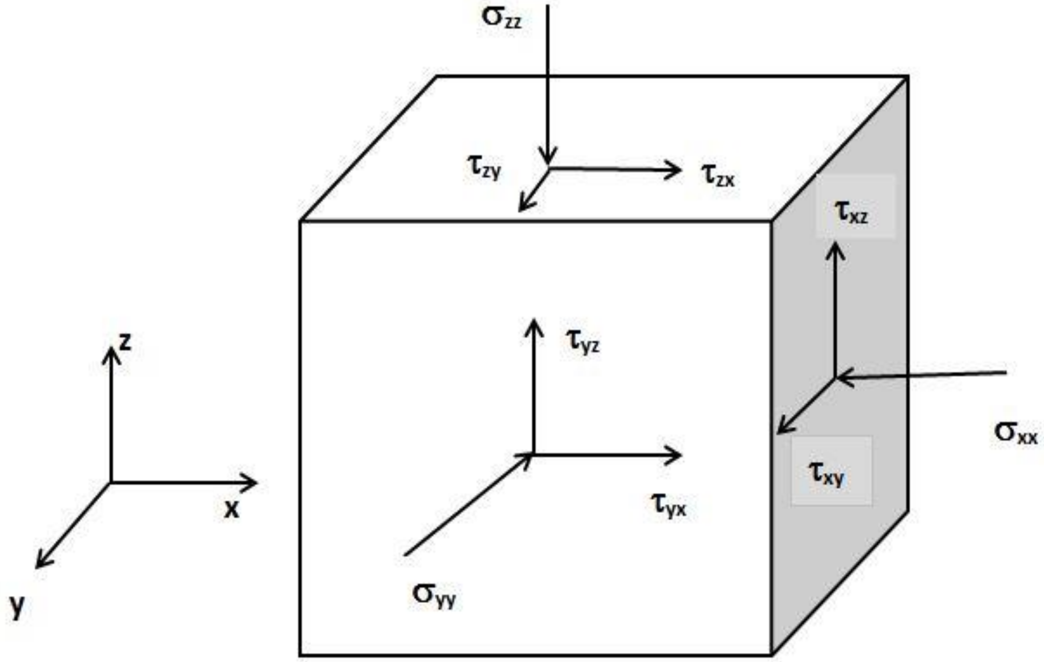

Figure 2.1. Illustration of stress tensor components

The fluids occupying the pore spaces in the earth are pressurized due to the acting overburden stress. This fluid pressure acts radially outward and mitigates or augments the existing stresses. The net stress or effective stress is responsible for any strain or deformation caused. The effective stresses (σ') become a key component in the stability and strength of various geologic settings. The effective stress (σ') is expressed as follows (Terazghi, 1936):

$$\sigma' = \sigma - P_P \tag{19}$$

The relation between rock failure and effective stresses can be best illustrated using the Mohr circle representation for a two dimensional state of stress as shown in Figure 2.2. An increase in Pore pressure (P_P) will cause the circle to slide towards the failure criterion thereby reducing stability and increasing the probability of failure.

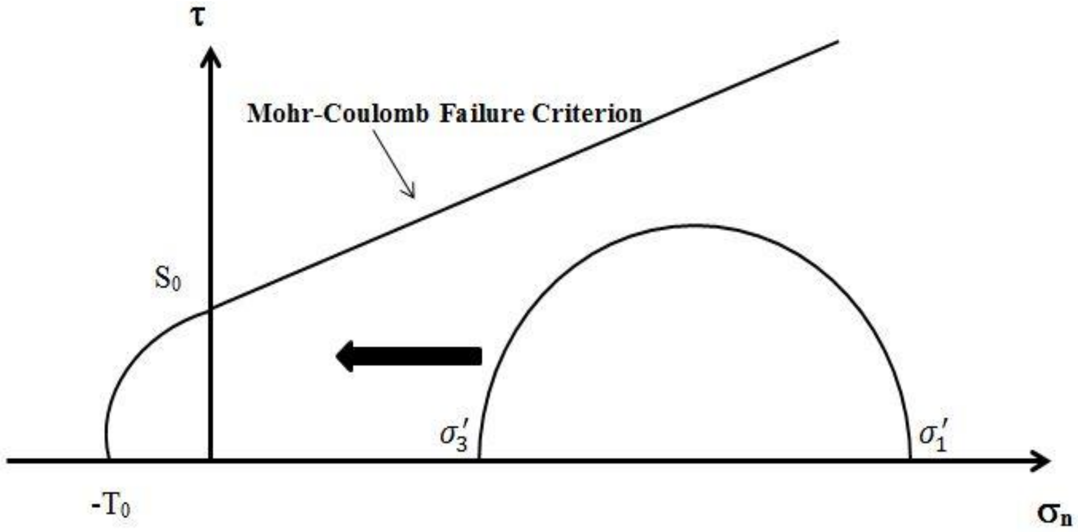

Figure 2.2. Mohr's circle representing a 2D state of stress.

2.2.2. Strain. Rock bodies, irrespective of size, deform when forces act on them. An important way of measuring the deformation is using strain. Figure 2.3 shows two points (A and B) in a sample rock showing the change of position due to the stress acting. If the relative position of the points within the sample is changed, the sample is said to be strained. Strain is defined as (Fjaer, 2008):

$$\varepsilon = \frac{L - L'}{L} = -\frac{\Delta L}{L} \tag{20}$$

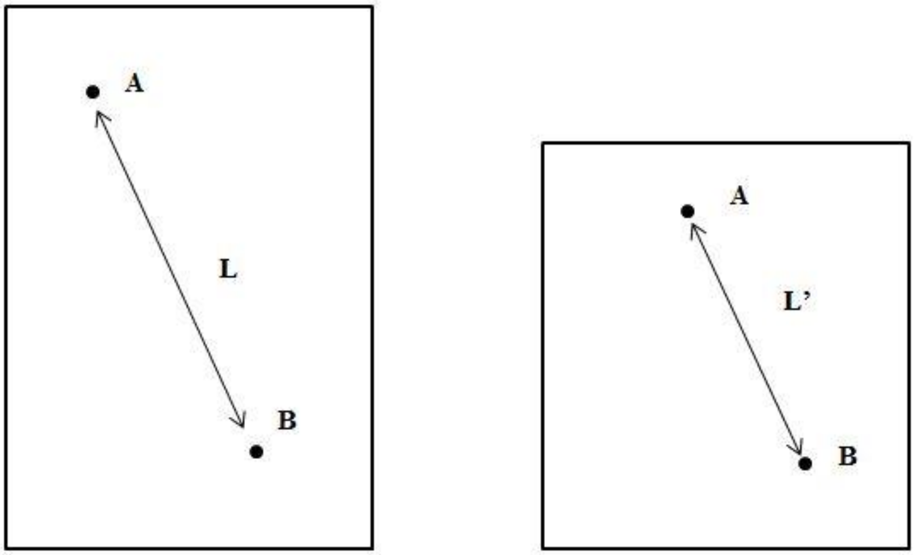

Initial Position

Shifted Position

Figure 2.3. Shifting of relative position due to deformation

Shear strain (Γ) is expressed as the change in the angle (ψ) between initially perpendicular directions as shown in Figure 2.4. The quantity is expressed as:

$$\Gamma = \frac{1}{2}\tan\psi \tag{21}$$

The strain tensor in 3D is as follows:

$$\overleftrightarrow{\varepsilon} = \begin{pmatrix} \varepsilon_{11} & \Gamma_{12} & \Gamma_{13} \\ \Gamma_{21} & \varepsilon_{22} & \Gamma_{23} \\ \Gamma_{31} & \Gamma_{32} & \varepsilon_{33} \end{pmatrix} \tag{22}$$

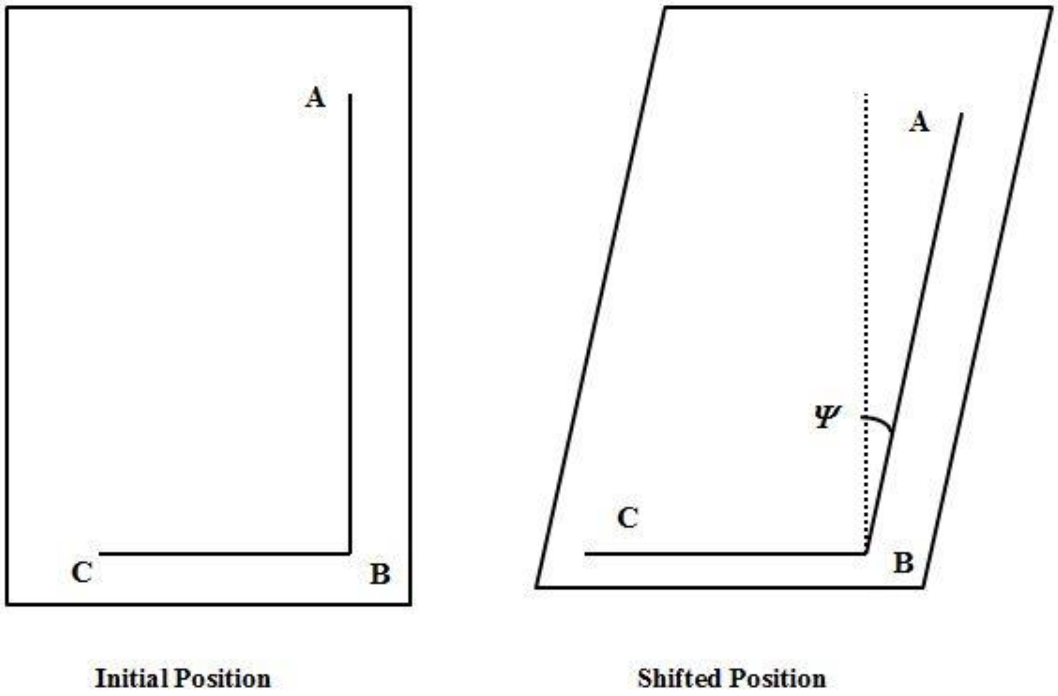

Figure 2.4. Illustration of shear strain

2.2.3. Linear Elasticity. Stress acting on a body causes deformation that is measured using strain. The relation between stress and strain is the foundation of the theory of elasticity and an integral part of continuum mechanics. The simplest and most commonly used form for the stress and strain relationships for rocks is that of linear elasticity where the strain is a linear function of the stress tensor. When a load is applied, rocks respond by deformation. Often, the loads applied cause a small deformation such that the stress strain relation can be safely assumed to be linear. This is illustrated in Figure 2.5. The response to stress is linear.

This relation can be explained using the Hooke's law. The modified and general form of Hooke's law for 3D is given in Equation 23.

$$\sigma_{ij} = C_{ijkl}\varepsilon_{kl} \tag{23}$$

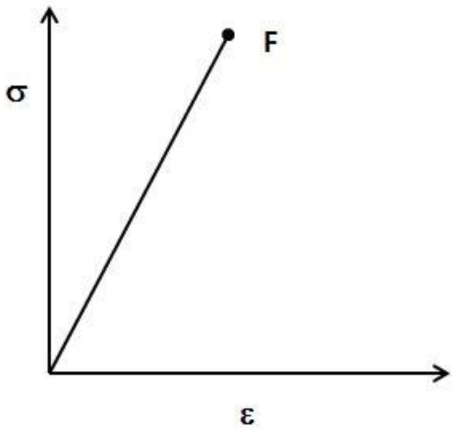

Figure 2.5. Linear elastic behavior with failure at F

C_{ijkl} is called the stiffness tensor that defines rock response to stress where i, j, k, l may each take the values 1, 2, or 3. It has 81 components of elastic constants. However the number of independent constants is considerably less due to constants being equal by symmetry. For an anisotropic medium, the number of constants is reduced to 21 (Fjaer, 2008). The stress strain behavior in a single direction, shown in Figure 2.5 can be represented as shown in Equation 24.

$$\sigma = E\varepsilon \tag{24}$$

Where E is a constant that measures the stiffness of an elastic material and is called the Young’s Modulus. It is defined as the slope of the stress strain curve of an elastic medium (Jager and Cook, 1979). Poisson’s ratio (ν) is another important elastic parameter that plays an important role in deformation of the rock. It is defined as the ratio of lateral strain to the longitudinal strain as shown in Equation 25. Poisson’s ratio is a positive number because a longitudinal compression would result in a transverse or lateral expansion and vice versa.

$$\nu_{ji} = -\frac{\varepsilon_i}{\varepsilon_j} \tag{25}$$

υ_{ji} can be interpreted as the ratio that characterizes transverse strain in i due to longitudinal strain in j (or when the material is stressed in the j direction). Another commonly used elastic modulus is the shear modulus (G) also known as the rigidity modulus (Fjaer, 2008). It is a measure of the materials stiffness against shear deformation. Mathematically, it can be expressed as follows:

$$\tau_{ij} = G\Gamma_{ij} \tag{26}$$

In Equation 26, τ_{ij} is the shear stress and Γ_{ij} is the shear strain caused by the stress.

2.2.3.1 In-situ stress. The in-situ state of stress of many sedimentary basins is given by the Andersonian stresses S_v, S_H and S_h. The stress regimes can be differentiated using the relative magnitudes of the principal stress or based on the type of faults that are created. The three stress regimes mentioned above are 1) Normal fault stress regime or Extensional stress regime, 2) Reverse fault stress regime and 3) Strike-slip fault stress regime. For a Normal stress regime, the overburden (S_v) is the maximum principal stress and S_H is the least principal stress. For a Reverse stress regime, S_H and S_v are the maximum and minimum principal stress, respectively. For a strike slip stress regime, the overburden is the intermediate principal stress while S_H and S_h are the maximum and minimum principal stresses. The relative magnitudes can be viewed in Table 2.1.

The overburden of vertical stress can be obtained by integrating the weight of the rock above the point of interest. The equation used to calculate the overburden is shown below in Equation 27.

$$\sigma_{ovb} = \int \rho_z \, g dz \tag{27}$$

Where dz is the change in depth and ρ_z is a density function in terms of z.

Table 2.1. Different stress regimes based on the relative magnitude of the principal stresses

Stress regime	Relative stress magnitudes
Normal	$S_V > S_H > S_h$
Reverse	$S_H > S_h > S_V$
Strike-Slip	$S_H > S_V > S_h$

2.2.3.2 Uniaxial strain (UAE). In order to define the horizontal stresses in an extensional state of stress, often the uniaxial strain model (UAE) is applied. The UAE model assumes that the tectonic contribution to the state of stress in many sedimentary basins is zero; i.e. the lateral strain is zero. Due to the Poisson's effect, stress in one direction will cause the body to expand in the other two directions and a horizontal stress results. Combining Equations 24 and 25 to calculate strain in a direction caused by stresses in all three directions.

$$\varepsilon_1 = \frac{\sigma_1}{E} - \frac{\nu\sigma_2}{E} - \frac{\nu\sigma_3}{E} \tag{28}$$

This is strain in one direction due to stresses acting in the other two directions. Equations for ε_3 and ε_2 can similarly be calculated. To simplify this three dimensional analysis to one, UAE and isotropy are assumed ($\varepsilon_3 \neq 0$, $\varepsilon_1 = \varepsilon_2 = 0$; $\sigma_2 = \sigma_3$).

$$\sigma_1{}' = \frac{\nu}{1-\nu}\,\sigma_3{}' \tag{29}$$

It is to be noted that the stresses mentioned in Equation 29 are effective stresses or the net stresses that actually cause strain. Applying Equation 29 to geologic models (where pore pressures are taken into account),

$$\sigma_h = \frac{\nu}{1-\nu}\left(\sigma_v - \alpha P_p\right) + \alpha P_p \tag{30}$$

α is the Biot's constant; P_p is the pore pressure; σ_h and σ_v are horizontal and vertical stresses, respectively. Equation 30 is the Eaton's modified equation (Britt, 2009) used by the oil and gas industry to estimate horizontal stresses from the overburden. It should be noted that for the modeling study presented in this thesis, an extensional state of stress based on the UAE model is assumed.

2.2.4. Isotropy. Isotropy is a condition where the parameter measured is constant irrespective of the direction in the material it is measured in. For simplicity reasons, the common approach for many rock mechanical applications is to assume isotropy of the reservoir rocks.

2.2.5. Orthotropic Materials and Transverse Isotropy. An orthotropic material is defined by the fact that the mechanical properties of the material are different in the three different mutually perpendicular axes. This means they have mutually orthogonal axes of rotational symmetry. Applying Hooke's law for this case, the following has to be satisfied:

$$C_{14} = C_{15} = C_{24} = C_{25} = C_{34} = C_{35} = C_{46} = C_{56} = 0 \tag{31}$$

The stiffness matrix of an orthotropic linear elastic material can be written as:

$$\begin{bmatrix} C_{11} & C_{12} & C_{13} & 0 & 0 & 0 \\ C_{21} & C_{22} & C_{23} & 0 & 0 & 0 \\ C_{31} & C_{32} & C_{33} & 0 & 0 & 0 \\ 0 & 0 & 0 & C_{44} & 0 & 0 \\ 0 & 0 & 0 & 0 & C_{55} & 0 \\ 0 & 0 & 0 & 0 & 0 & C_{66} \end{bmatrix} \tag{32}$$

Transverse isotropy is a special case of orthotropic isotropy characterized by a plane of isotropy at every point in the material. Within this plane, mechanical properties are the same in every direction. The number of independent constants in the stiffness tensor is reduced to 5 from 21 for a fully anisotropic material. Assuming that the properties are same in the x-y plane and are different in the z direction, the following is required:

$$C_{11} = C_{22} \tag{33}$$

$$C_{13} = C_{23} \tag{34}$$

$$C_{12} = C_{11} - 2C_{66} \tag{35}$$

$$C_{44} = C_{55} \tag{36}$$

Substituting Equations 33 through 36 into the elastic tensor in Equation 32 would give the stiffness tensor of a transversely isotropic material. Shales, because of the textured layering and depositional environment, are transversely isotropic in a horizontal plane of isotropy with a vertical axis (Waters, 2011).

The stiffness matrix in the case of transverse isotropy can be expressed in terms of elastic moduli E, ν and G. Due to the depositional nature and laminated structure of the shale matrix, the plane of isotropy is the horizontal plane (x-y plane). For this case, $E_1 = E_2$, $\nu_{31} = \nu_{32} = \nu_{12} = \nu_p$, $G_{13} = G_{23}$ and $\nu_{13} = \nu_{23} = \nu_t$. The stiffness matrix is given in Equation 37.

$$\begin{bmatrix} 1/E_1 & -\nu_p/E_1 & -\nu_p/E_3 & 0 & 0 & 0 \\ -\nu_p/E_1 & 1/E_1 & -\nu_p/E_3 & 0 & 0 & 0 \\ -\nu_t/E_1 & -\nu_t/E_1 & 1/E_3 & 0 & 0 & 0 \\ 0 & 0 & 0 & 1/G_{12} & 0 & 0 \\ 0 & 0 & 0 & 0 & 1/G_{13} & 0 \\ 0 & 0 & 0 & 0 & 0 & 1/G_{13} \end{bmatrix} \tag{37}$$

ν_p is the Poisson’s ratio that characterizes strain in the plane of isotropy due to a stress or load normal to it.

2.2.6. Tensile Failure. For sufficiently large stresses, the rock fails. The type of failure depends on the rock characteristics as well as the nature and direction of the stresses acting on it. Rocks endure a certain stress level before they fail. This stress level can be described as the strength of the rock. ‘Rock strength’ is generally understood as the stress level at which rock fails but has no specific definition and is not uniquely defined. Rock failure can be categorized and described by the type of failure and the nature of stress under which it happens. The most common of the failures are ‘shear failure’, caused by excessive shear stresses and ‘tensile failure’ caused by excessive tensile stresses.

Hydraulic fracturing involves tensile failure of the rock by increasing the acting fluid pressure on the rock. Tensile failure occurs when the acting extensional stresses exceed the ‘tensile strength’ of the rock. The uniaxial tensile strength ($\boldsymbol{T_0}$) is defined as the maximum tensile stress a rock can endure before it fails under the conditions where stress is applied in a single direction (Fjaer, 2008). The mathematical form of the statement above can be found in Equation 38. In general, the tensile strength of rocks is much lower than the shear strength (Kocher, et al., 2008). Figure 2.6 depicts tensile failure in a rock.

$$\sigma' = -T_0 \tag{38}$$

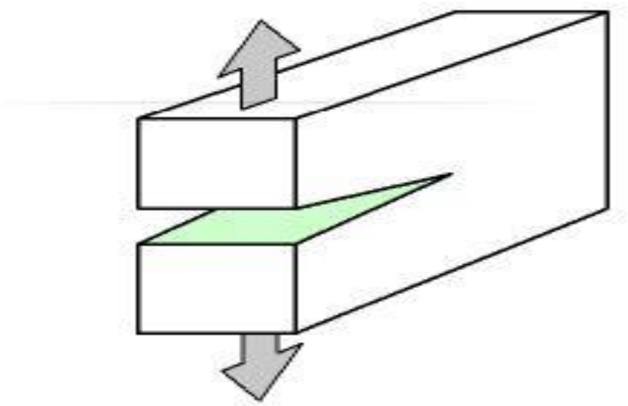

Figure 2.6. Tensile failure created in a rock due to extensional stresses

For the case of hydraulic fracturing, one important thing to note here is that the tensile stresses are induced by pumping fluids at a high volume rate. The minimum principal stress in the reservoir is the easiest stress to overcome to initiate failure. Hence the direction of the fracture plane is perpendicular to the minimal principal stress. Under continued pumping, the crack opens and propagates taking the path of the least resistance. For geologic settings over a large scale and for the case of $S_V > S_H > S_h$, this is the direction of the maximum horizontal stress. For general reservoir conditions, Equation 38 can be rewritten as shown in Equation 39.

$$\sigma_3' = -T_0 \tag{39}$$

2.3. HYDRAULIC FRACTURING

Hydraulic fracturing is a process that enhances production of hydrocarbons from underground reservoirs. In this process, fluid is pumped at a high pressure into the well at a depth that if of interest. A fracture is created when the pressure is high enough for rock failure to occur in tension, i.e. a hydraulic fracture is initiated. This fracture creates a highly conductive pathway in low permeability reservoirs that enhances hydrocarbon production rates as well as the total hydrocarbons that can be produced. An important part of hydraulic fracturing is to accurately predict the dimensions of the fracture based on existing knowledge of in situ stresses, reservoir properties and fracturing fluid properties.

Petroleum Engineers do not have the luxury of observing events and processes like hydraulic fracturing. Indirect analyses based on pump pressure readings, flow rates or other methods like microseismic monitoring help achieve the goal of understanding the ongoing events and make necessary changes. Observing pressure variation over time gives us a fair idea of reservoir conditions. Figure 2.7 shows bottomhole pressure increasing during fracturing and declining during leakoff. The closure pressure is defined as the pressure at which the fracture closes if the proppant is not in place. The net pressure (P_{net}) is defined as the difference between bottomhole pressure during fracture treatment and the closure pressure (Britt, 2009). Mathematical description of P_{net} is given in Equation 40.

$$P_{net} = P_w - P_c \tag{40}$$

P_w is the bottomhole pressure in Pa and P_c is the closure pressure in Pa. As depicted in Figure 2.7, the bottomhole pressure increases with time as fluid is pumped into the wellbore. A pressure decline is observed when pumping stops. This is because the fracture fluid that is used to drive the hydraulic fracture now leaks off into the formation through the fracture planes. This happens because of the pressure difference between the reservoir and inside the fracture. Hydraulic fracture treatments are done using a pressure that is higher than the breakdown pressure. The breakdown pressure is the pressure at which the rock matrix fails and is explained in detail in the sections below.

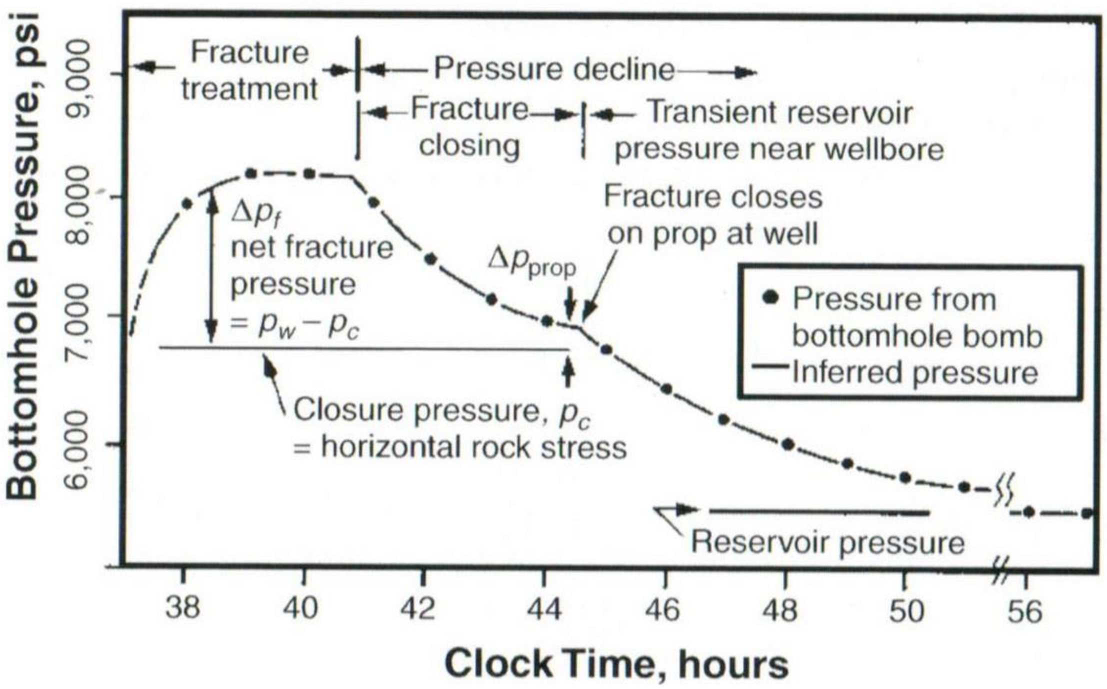

Figure 2.7. Bottomhole pressure versus time during a hydraulic fracture process (Britt, 2009)

The fracture stimulation design is achieved in three stages. The first stage includes pumping fluid into a hydraulically sealed section of the wellbore to initiate and propagate a fracture until it achieves the desired half length and width. The second stage consists of pumping a ‘proppant’ along with the fluid (Britt, 2009). Proppant is pumped in increasing concentrations to achieve a constant proppant concentration through the entire length of the fracture. A proppant represents a granular material as shown in Figure 2.8 that is used to keep the fracture open after the pumping of fluid ceases. The selection of proppant depends on the desired fracture permeability and the strength of the proppant material. The third stage is where the treatment is flushed to the perforations and the fluid is allowed to leak off into the formation before starting production.

Figure 2.8. High strength traceable ceramic proppant (CARBO Ceramics)

The fracture propagation depends on the in situ stress directions. As mentioned above, hydraulic fractures are always created perpendicular to least principal stress. Since, induced hydraulic fractures are in general created at considerable depths, they are vertical. At shallow depths or scenarios where the principal stresses have been altered by geologic activity like salt intrusions, the created fractures may be horizontal (Britt, 2009). The success of a hydraulic fracture treatment can be measured using well productivity and ultimate recovery. A dimensionless term called fracture conductivity (F_{CD}) is used for this purpose. It relates reservoir (k) and fracture (k_f) permeabilities, fracture half-length (x_f) and fracture width (w) and can be expressed as:

$$\mathrm{F}_{CD} = \frac{k_f w}{k x_f} \tag{41}$$

Optimum performance of wells in permeable reservoirs is observed when F_{CD} is 2.3. For low and ultra-low permeability reservoirs, fracture length determines the productivity of wells while the importance of F_{CD} is diminished.

2.3.1. Fracturing a Wellbore. Understanding the stresses around a borehole is critical to accurately calculate the fracture pressures of a vertical wellbore. Equations 42 and 43 (Kirsch, 1898) mathematically describe the stresses around a borehole in terms of radial stress and hoop stress. Radial stress ($\boldsymbol{\sigma_{rr}}$) is a stress that is perpendicular to the borehole wall at all times and a hoop stress ($\boldsymbol{\sigma_{\theta\theta}}$) is tangential to the bore hole wall. The kirsch equations, assuming that rock is a linear elastic medium, are given by Zhang (2006):

$$\sigma_{\theta\theta} = \frac{1}{2}(\sigma_1 + \sigma_2 - 2P_P)\left[1 + \frac{R^2}{r^2}\right] - \frac{1}{2}(\sigma_1 - \sigma_2)\left[1 + 3\frac{R^4}{r^4}\right]\cos 2\theta - \Delta P\frac{R^2}{r^2} \tag{42}$$

$$\sigma_{rr} = \frac{1}{2}(\sigma_1 + \sigma_2)\left[1 - \frac{R^2}{r^2}\right] + \frac{1}{2}(\sigma_1 - \sigma_2)\left[1 - 4\frac{R^2}{r^2} + 3\frac{R^4}{r^4}\right]\cos 2\theta + \Delta P\frac{R^2}{r^2} \tag{43}$$

$$\Delta P = P_{mud} - P_P \tag{44}$$

Where σ_2 is the minimum principal stress in Pa, σ_1 is the maximum principal stress in Pa, P_P is the pore pressure in Pa, P_{mud} is the mud pressure in Pa, R is the distance between the axis of the vertical wellbore in m and the point of interest, r is the radius of the wellbore in m and θ is the angle of deviation of point R away from the σ_H direction. For the case of $R = r$, we obtain the stresses at the borehole walls as shown in Figure 2.9. The hoop and radial stresses are calculated using Equations 45 and 46.

$$\sigma_{\theta\theta} = (\sigma_1 + \sigma_2) - 2(\sigma_1 - \sigma_2)\cos 2\theta - 2P_P - \Delta P \tag{45}$$

$$\sigma_{rr} = \Delta P \tag{46}$$

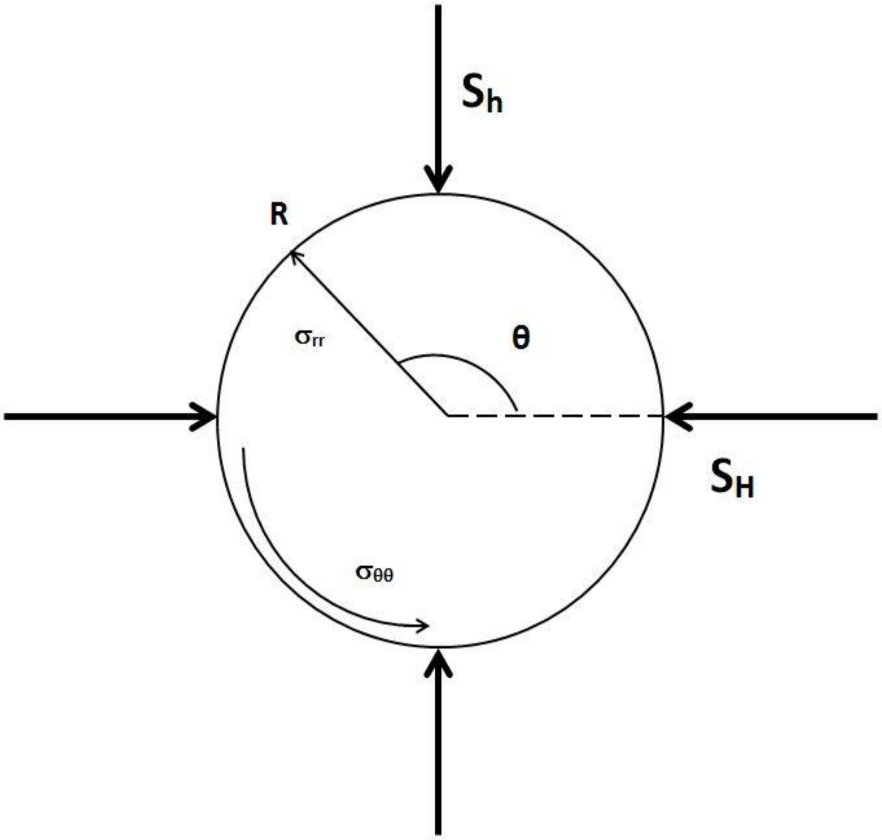

Figure 2.9. Illustration of stresses around a borehole

2.3.2. Hydraulic Fracturing in Horizontal Wells. Equations governing hydraulic fracturing in horizontal wells are based on the same principles as those governing hydraulic fracturing in vertical wells. The modified Kirsch equations given in Equations 45 and 46 for a horizontal well drilled in the intermediate principal stress direction in an extensional stress regime are given in Equations 47 and 48 (Zoback, 2010).

$$\sigma_{\theta\theta} = (\sigma_V + \sigma_h) - 2(\sigma_V - \sigma_h)\cos 2\theta - 2P_P - \Delta P \quad (47)$$

$$\sigma_{rr} = \Delta P \quad (48)$$

To initiate a tensile failure, the tangential or the hoop stress must be overcome. The fracture is created perpendicular to the minimum hoop stress direction. From Equation 47, it is deduced that the minimum hoop stress value is obtained at $\theta = 0$.

The breakdown pressure (P_b) of a rock is defined as the pressure required to initiate a fracture. Assuming that rock is a linear elastic medium with a uniaxial tensile strength of T_0, P_b for vertical wells can be calculated from Equation 47 with the value of θ as 0 and is shown in Equation 49. P_b for horizontal wells is shown in Equation 50 (Yew, 1997):

$$\mathrm{P}_b = 3\sigma_\mathrm{h} - \sigma_\mathrm{H} - P_P + T_0 \quad (49)$$

$$\mathrm{P}_b = 3\sigma_\mathrm{h} - \sigma_\mathrm{V} - P_P + T_0 \quad (50)$$

At greater depths, the tensile strength of the rock has a small effect on the magnitude of breakdown pressure compared to the stress magnitudes of σ_1 and σ_3. It is mainly dictated by the required pressure to overcome the compressive circumferential stresses around a borehole. The fracture propagates if the pumping of fluid continues. It is important to maintain a pump pressure greater than the breakdown pressure because the differential pressure is responsible for creating the opening in a fracture (Yew, 1997).

The greater the differential pressure between the bottomhole pressure (P_w) and the minimum in situ stress, the greater the fracture width. The fluid inside a fracture also leaks off into the formation at a rate known as the fluid leakoff rate.

Considering material balance and accounting for the total volume of fluid injected is important to mathematically predict fracture geometry based on pump parameters. The following relationship can be expressed that accounts for the total fluid pumped into the system:

$$V_P = V_f + V_L \tag{51}$$

Where V_P is the fluid volume pumped, V_f is the volume of fluid in the fracture, V_L is the volume that leaked off into the reservoir. They can be expressed as follows (Britt, 2009):

$$V_P = \mathrm{q} t_P \tag{52}$$

$$V_L = 2Ch_P L\sqrt{t} + 2LS_P h_p \tag{53}$$

$$V_f = whL \tag{54}$$

Where q is the fluid pump rate, is the pump time in minutes, C is the fluid loss coefficient, h_P is the permeable fracture height, w is the fracture width, S_P is the fluid loss per area before a filter cake is formed and h is the total fracture height. The rate of fluid lost into the formation is explained in detail in further sections.

Green (1963) proposed a solution that relates fracture width and pump pressure for a plane fracture in an infinite elastic medium. The solution is as shown in Equation 55.

$$\mathrm{w} = \frac{4(1-\nu)L}{\pi G}\left[\int_{f_L}^{1}\frac{f_2 df_2}{\sqrt{{f_2}^2-{f_L}^2}}\int_{0}^{f_2}\frac{p(f_1)df_1}{\sqrt{{f_2}^2-{f_L}^2}}-\frac{\pi}{2}\sigma_3\sqrt{1-{f_L}^2}\right] \tag{55}$$

Where G is the shear modulus, ν is the Poisson's ratio, f_1 and f_2 are fractions of the extent of fracture and σ_3 is the minimum principal stress. Greetsma and de Klerk (1969) used this equation for a circular crack and applied boundary conditions for a smooth fracture tip. A simplified form of that solution in isotropic conditions with proper boundary conditions is now commonly used in the industry to predict fracture width and is given in Equation 4.

2.3.3. Fracture Mechanics. A thorough understanding of the fundamentals in fracture mechanics is necessary to fully understand and replicate hydraulic fractures or any cracks in rocks.

2.3.3.1 Fracture energy approach. Fracture growth can be expressed in terms of the energy required to overcome the resistance of the material. Griffith (1920) was the first to study and present analyses using the energy approach, but Irwin (1957) is primarily responsible for the advances in the energy approach to fracture mechanics. This theory states that the fracture propagates when the energy release rate ($\boldsymbol{G}$) is equal or greater than the resistance of a material to fracture ($\boldsymbol{G_C}$). The energy release rate is defined as the rate of change in potential energy and can be expressed as follows (Anderson, 1995):

$$\mathrm{G} = \frac{\pi\sigma^2 a}{E} \tag{56}$$

Where a is the half length of the crack in a linear elastic medium subject to a tensile stress of σ and with a Young's Modulus of E as shown in Figure 2.10. At the moment of fracture, $\boldsymbol{G}$ equals $\boldsymbol{G_C}$ (a measure of Fracture toughness) and the magnitude of stress (σ) is known as failure stress (σ_f) and is shown in Equation 57.

$$G_c = \frac{\pi \sigma_f^2 a}{E} \quad (57)$$

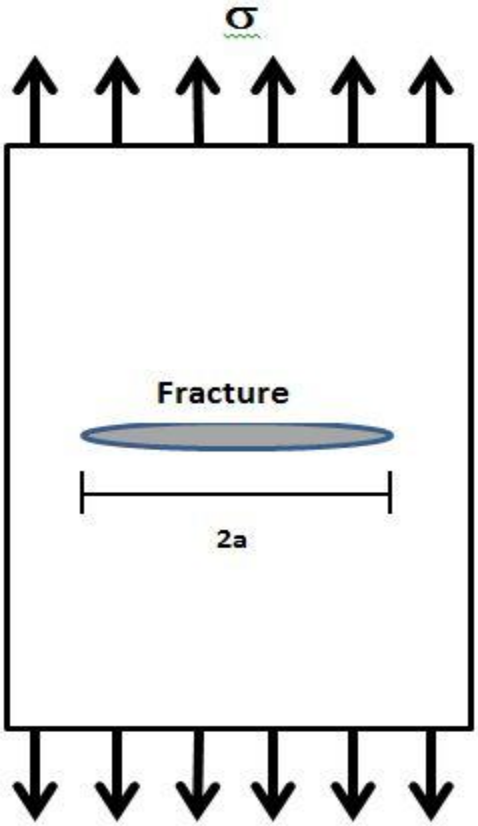

Figure 2.10. Fracture propagation in a linear elastic medium subject to tensile stress

The crack initiation can be defined in terms of a quadratic function of traction separation behavior. Nominal traction vectors represent averaged traction vectors over a given area. The tractions on fracture surfaces can be defined in terms of a normal traction vector (t_n) and two shear traction vectors (t_s and t_t). t_n^0, t_s^0 and t_t^0 are the maximum nominal tractions when the deformation is purely in one of the three principal directions. According to the traction separation law failure criteria (Camanho et al., 2003), fracture initiates when the following quadratic interaction function reaches a value of 1 as shown in Equation 58. The relation between fracture energy and tractions are further discussed in Section 3.3.2.

$$\left\{\frac{\langle t_n \rangle}{t_n^o}\right\}^2 + \left\{\frac{t_s}{t_s^o}\right\}^2 + \left\{\frac{t_t}{t_t^o}\right\}^2 = 1 \tag{58}$$

2.3.3.2 Stress intensity approach. Each component of a stress tensor at the tip of a crack or fracture is proportional to a constant called the Stress intensity factor ($\mathbf{K}_{\boldsymbol{I}}$). When this constant is known, the entire stress tensor at the tip can be calculated. The value of $\mathbf{K}_{\boldsymbol{I}}$ when the fracture further propagates is called the critical stress intensity factor ($\mathbf{K}_{\boldsymbol{IC}}$). $\mathbf{K}_{\boldsymbol{IC}}$ is also a measure of fracture toughness. $\mathbf{K}_{\boldsymbol{I}}$ can be expressed as follows in terms of stress acting on the crack tip (**$\boldsymbol{\sigma}$**):

$$\mathrm{K}_I = \sigma\sqrt{\pi a} \tag{59}$$

K_{IC} can be expressed as shown in Equation (60) in terms of failure stress (σ_{f})

$$\mathrm{K}_{IC} = \sigma_f\sqrt{\pi a} \tag{60}$$

Both K_I and G are a measure of fracture toughness. The relationship between them is as follows (Anderson, 1995):

$$\mathrm{G} = \frac{{\mathrm{K}_I}^2}{E} \tag{61}$$

2.3.3.3 Fracture propagation. Once a fracture is created, under further loading, the fracture propagates depending on the stresses acting on the body. There are many failure propagation criteria listed but as shales are transversely isotropic, the Benzeggagh-Kenane failure criterion (BK) best suits the conditions. The BK form assumes that the critical fracture energies along both the shear directions are equal as shown in Equation 63. The failure criterion is expressed in Equation 62 (Benzeggagh and Kenane, 1996):

$$G_n^C + (G_s^C - G_n^C)\left\{\frac{G_S}{G_T}\right\}^{\eta} = \mathrm{G}^C \tag{62}$$

$$G_s^C = G_t^C \tag{63}$$

Where G_n^C is the critical fracture energy in the normal direction to the fracture surface, G_s^C and G_t^C are the critical fracture energies in the shear directions, G_T is the total fracture energy i.e the sum of the normal (G_n) and two shear fracture energies (G_s and G_t), G_S is the sum of the two shear fracture energies (Dassault Systems, 2011).

2.3.3.4 Mechanics of fluids in fracture. The flow of fluids in a fracture can be described using tangential fluid flow and normal fluid flow as shown in Figure 2.11. Two main assumptions are made: (1) the fluid is assumed to be incompressible and follows the Newtonian rheology. (2) Constant fluid leakoff across the fracture surface with no increasing resistance due to 'caking' is also assumed. For a Newtonian fluid, the fluid continuity statement can be given as follows:

$$\mathrm{q}_f \mathrm{d} = -k_t \nabla p \tag{64}$$

q_f is the volume flow rate density vector in the tangential direction, d is the opening of the fracture, ∇p is the pressure differential across the fracture and k_t is termed the tangential permeability, i.e. the permeability that defines the resistance of fluid flow in the tangential direction. k_t is defined using a variation of the Reynold's equation in terms of d and μ (viscosity of fluid in facture). The mathematical definition is given below:

$$k_t = \frac{\mathrm{d}^3}{12\mu} \tag{65}$$

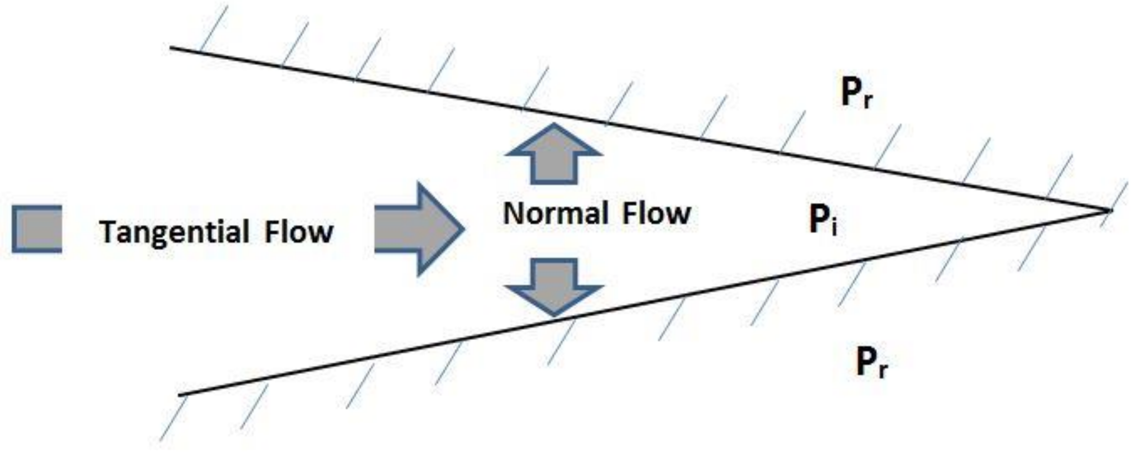

Figure 2.11. Components of fluid flow within a fracture

The normal flow in a fracture is driven mainly due to the pressure difference between the fracturing fluid and the pressure in the formation as shown in Figure 2.11. The flow rate of fluid leaking into the formation (q_L) can be given as:

$$q_L = C(P_i - P_r) \tag{66}$$

P_i and P_r are the pressure inside a fracture and in the formation, respectively. C is a measure of the permeability of the fracture surface i.e. the resistance to fluid flowing across the surface and is known as the ‘fluid leakoff coefficient’. The oil industry defines the leak off coefficient in oilfield units a little differently.

3. METHODOLOGY

3.1. NUMERICAL ANALYSIS

Advances in numerical methods and digital computational capacity have accelerated growth in technology and the ease of finding solutions to many engineering problems. Analytical solutions exist for simple physical processes but for real life engineering situations, complex boundary conditions are encountered where analytical solutions do not exist. A numerical method provides an approximate and yet dependable solutions to complex engineering problems. The process involves dividing the model domain into smaller units (called discretization), calculating approximate solutions at selected points in the domain and approximating values at all other points. Formative works on numerical modeling methods that lead to today's high capability simulators include significant contributions from Turner (1956), Clough (1960) and Zienkiewicz (1969). With the advent of numerical modeling methods, many complex analyses in petroleum engineering like wellbore stability, stress concentration studies, pore pressure prediction; fracture analyses etc. became much more reliable. Various numerical modeling techniques have been developed and can be distinguished based on the type of approximations made when arriving at a solution. Examples of widely used numerical methods include Finite element method (FEM), Finite difference method (FDM), Boundary element method (BEM) and Discrete element method (DEM).

3.2. FINITE ELEMENT METHOD

The FEM provides an approximate solution to the governing partial differential equations (PDE) of the process involved. A PDE is a mathematical expression of a continuous physical process in which a dependent variable is a function of more than one independent variable. The displacement method, where displacements (u) are assumed to be unknown and are solved for, is adopted for this project. The FEM process involves discretization of a body into smaller subdivisions called 'elements' or in this case 'finite elements'. The corners of these elements or joints where they intersect and are connected to other elements are known as 'nodes'. Figure 3.1 shows discretization of a 3D model of the reservoir used in this research.

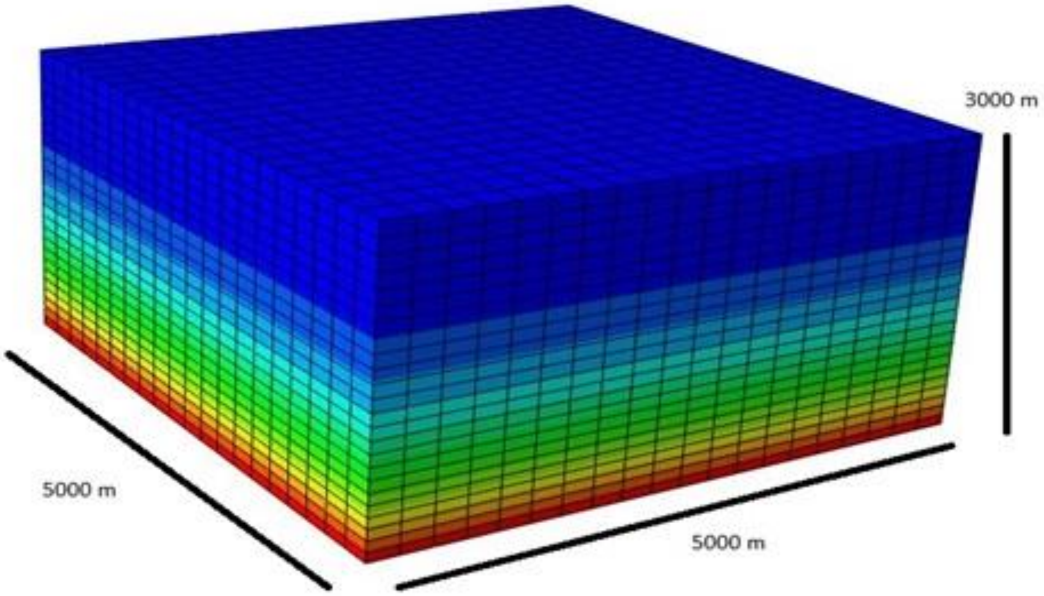

Figure 3.1. Discretization of the model showing nodes and elements

The general equation, for loads acting on a body in FEM, that is solved for is as follows:

$$q^e = K^e u^e + f^e \tag{67}$$

Where q^e is the nodal forces acting on the element, K^e is the element stiffness matrix, u^e is the displacement of the nodes and is the unknown in Equation 67 and f^e is the loading term on the nodes of the element. The same equilibrium equations for individual elements can be applied to the entire body by combining the forces and displacements of each element and is as follows:

$$q^G = K^G u^G + f^G \tag{68}$$

Here K^G is the global stiffness matrix or the stiffness matrix of the entire body, q^G is the nodal forces acting on the body, u^G is the displacement of the nodes and is the unknown in this equation and f^G is the loading term on the body. Classical methods like the Galerkin method and Raleigh Ritz method are used to solve for the equilibrium equations as mentioned in 57 and 58. Each term in Equation 68 represents a matrix. The global stiffness matrix is a square matrix with the dimensions n x n where n is the number of nodes in the system. The displacement function ($\vec{u}$) is a column matrix with n columns. The displacement function can be approximated as follows:

$$\vec{u} \approx \tilde{u} = \sum_a \overrightarrow{N_a} \widetilde{u_a^e} \tag{69}$$

The vector N_a represents the shape functions (or interpolation functions). When the coordinates of any node other than of the node itself are inserted into the shape functions, it results in a null matrix. The mathematical representation of this can be expressed as follows:

$$N_a(x_a, y_a) = I \tag{70}$$

$$N_a(x_b, y_b) = O \tag{71}$$

I is the identity matrix and O is the null matrix. Shape functions vary with the shape of the element and are derived for each element type. After shape functions are derived for each individual element, force equilibrium for all elements can be obtained by assembling the global set of equations (shown in Equation 72) and solving for u.

$$Ku + f = 0 \tag{72}$$

A further and more extensive review of the FE method is beyond the scope of this thesis and can be found in many standard textbooks, e.g. Zienkiewicz et al. (2005).

ABAQUS is a commercial finite element software package and was chosen to run the numerous hydraulic fracture simulations involved in this research.

3.3. MODEL DESCRIPTION

Great care should be taken when building geometries and models to simulate hydraulic fracturing in shales. Hydraulic fracturing in general is a complicated process to simulate because it involves complex boundary conditions that requires high computational systems. A balance has to be found by making simple assumptions, without compromising the accuracy of the solution, and realistic computational times.

Horizontal drilling increases the contact between hydrocarbon rich rock and the wellbore thereby increasing production rates. If hydraulic fractures are initiated, a huge network of conductive pathways that connects even more hydrocarbon bearing rock to the wellbore is being generated. Huge fractures are required to effectively produce from tight reservoirs like shale that usually extend up to a 1000 ft (reference) and sometimes more. The number of fractures depends on the fracture spacing for a reservoir of finite size and has a huge impact on how effectively the reservoir can be produced.

3.3.1. Model Geometry. All Finite Element models presented are variations of a base model which replicates a relatively simple scenario. Four fractures are assumed to be created in a horizontal wellbore drilled through a homogenous shale reservoir at a depth of 2100 m. 3D Pore pressure elements with reduced integration were used to model the shale while the fractures were modeled using cohesive elements. The diameter of the wellbore was chosen to be 9 inches (0.2286 m).

All models are a four fracture model where all the fractures planes are pre-defined. The aim is to study the fracture aperture and stress changes in and around the wellbore. Since the model is homogenous, computational time can be reduced by considering only half of the whole fracture + reservoir system by assuming a plane of symmetry in the y-z direction passing through the axis of the wellbore. The half models used for this research are depicted in Figure 3.2. A rectangular section of the reservoir around the borehole is modeled as shown in Figure 3.3.

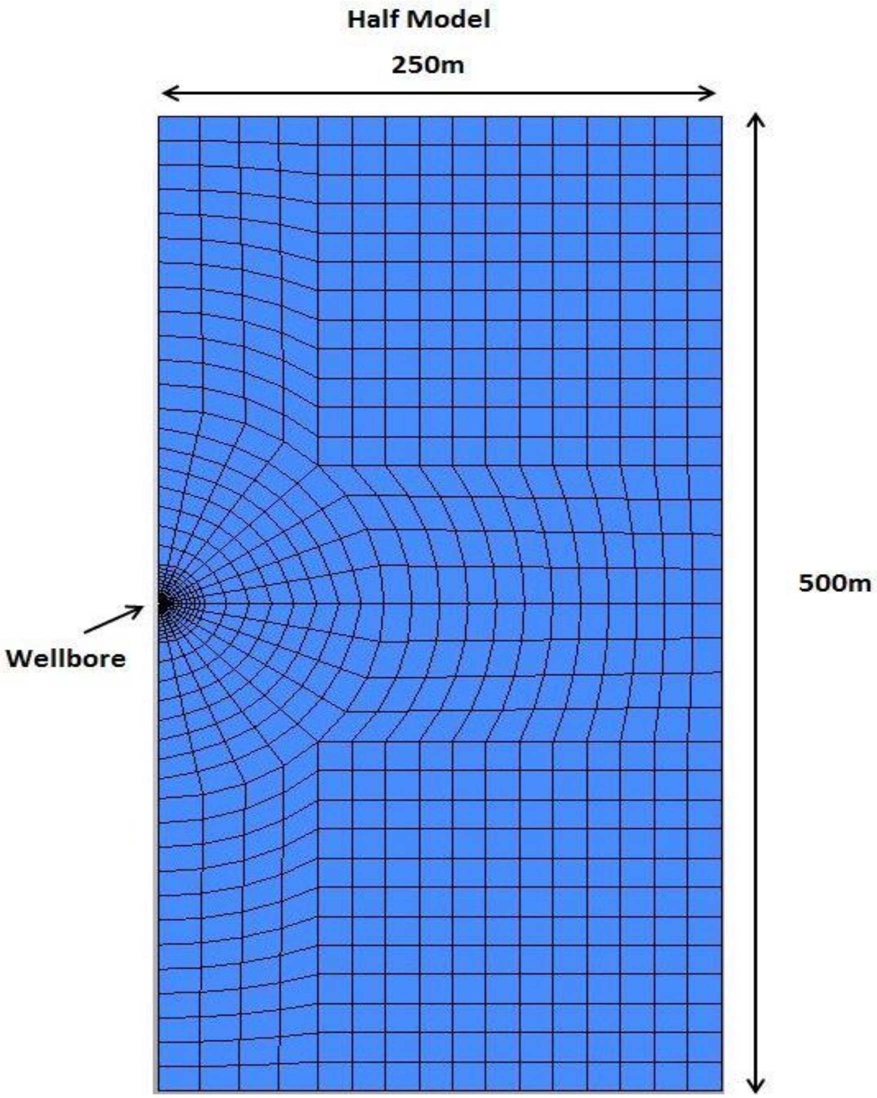

Figure 3.2. Dimensions of the model in x-z plane

Along the borehole axis 4 pre-defined fracture planes are included. The fracture height and half-length are 500 m and 250 m, respectively i.e. the end to end length of the fracture is equal to the fracture height. This makes the fracture a radial fracture where it propagates radially outward from the wellbore. The model has to accommodate the huge fractures and thus have the dimensions of 250m X 500m in the x-z plane. The length of the horizontal wellbore or the depth of the geometry in the y direction varies depending on the distance between fractures.

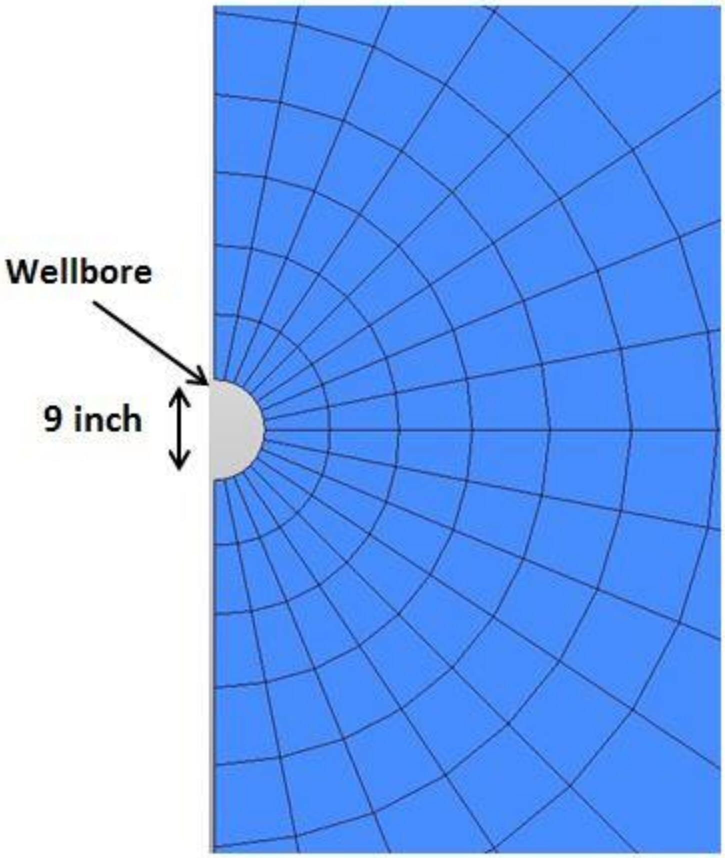

Figure 3.3. Figure depicting only half of the wellbore and reservoir model to save computational time

For the fracture spacing study (FSS), five models with increasing spacing between fractures were built. The dimensions of all models in FSS are the same with exception of depth in the y direction. The models have a fracture spacing of 40, 50, 60, 80 and 100 feet, respectively with all other input parameters being the same. For the anisotropy study (AS), the 60 ft model was used for the entirety of this section with introduction of different levels of anisotropy in each re-run. Only a quarter of the full model was considered to further reduce computational time as shown in Figure 3.4. The top half of the half model was considered because the focus is on the maximum widths of the fractures and it is encountered only in the top half.

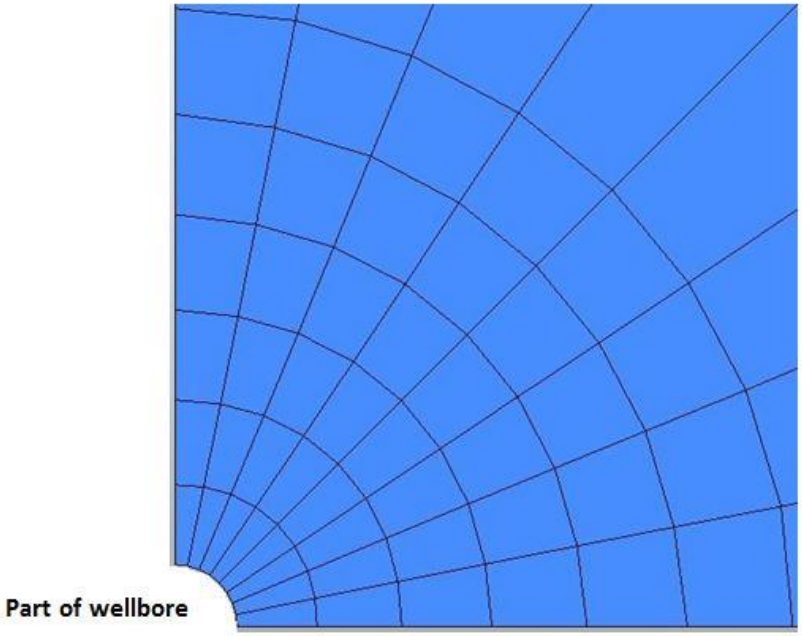

Figure 3.4. Part of the quarter model enlarged to show a quarter of the wellbore

The fractures, based on their position in the model, can be termed as ‘edge’ and ‘center’ fractures for clarity reasons and ease of analysis. The ‘edge’ fractures are the two fractures closest to the model boundary or ‘edge’ and the other two are called ‘center’ fractures as shown in Figure 3.5. In every model, the distance between the edge fracture and the boundary of the model was maintained as twice the distance between any two fractures.

3.3.2. Cohesive Elements. Cohesive elements were developed to successfully model adhesives, bonded interfaces and rock fractures (Hilberborg, 1976). One of the initial works that used cohesive elements to model a rock fracture was by Shet and Chandra (2002). The constitutive response of the cohesive elements is based on certain assumptions about the deformation. For this research, cohesive elements are described using the traction-separation law.

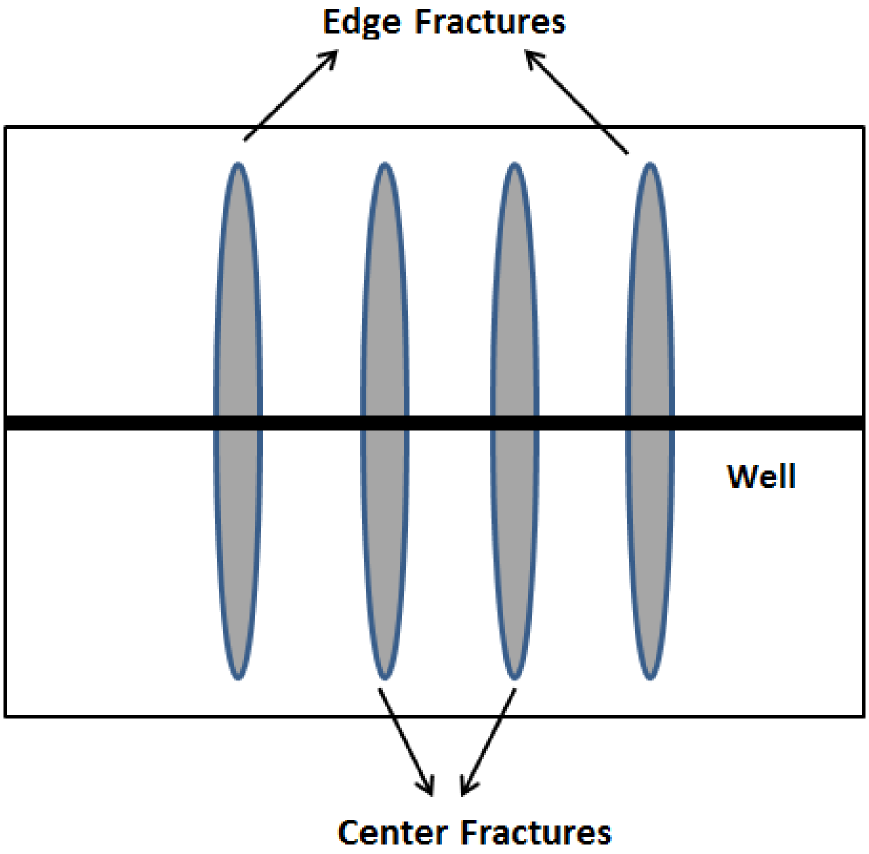

Figure 3.5. Figure depicting edge and center fractures in the model

Traction separation law is typically designed to model bonded surfaces where the cohesive elements are modeled with negligible thickness (in this case with 1mm thickness) as the intermediate glue material. The cohesive elements can model the initiation and propagation of damage leading to failure using concepts from fracture mechanics. Traction separation in ABAQUS follows three steps depending on the loads. If the stress acting is high enough to cause damage, ABAQUS models linear elastic behavior first followed by fracture initiation modeling and fracture propagation modeling, respectively. The elastic behavior is defined using a constitutive matrix that relates nominal stresses to the nominal strains across the interface.

The traction response to increasing separation is the basis for the traction separation law. Figure 3.6 depicts a typical traction separation response where the traction increases with increasing separation until it reaches a maximum value and then decreases. The strength of the cohesive elements is given in terms of maximum nominal stress it can withstand. Traction increases linearly with separation until the nominal stress reaches a maximum value. When the load increases to a point where the cohesive elements cannot transfer any further load, the stiffness matrix gradually drops to zero.

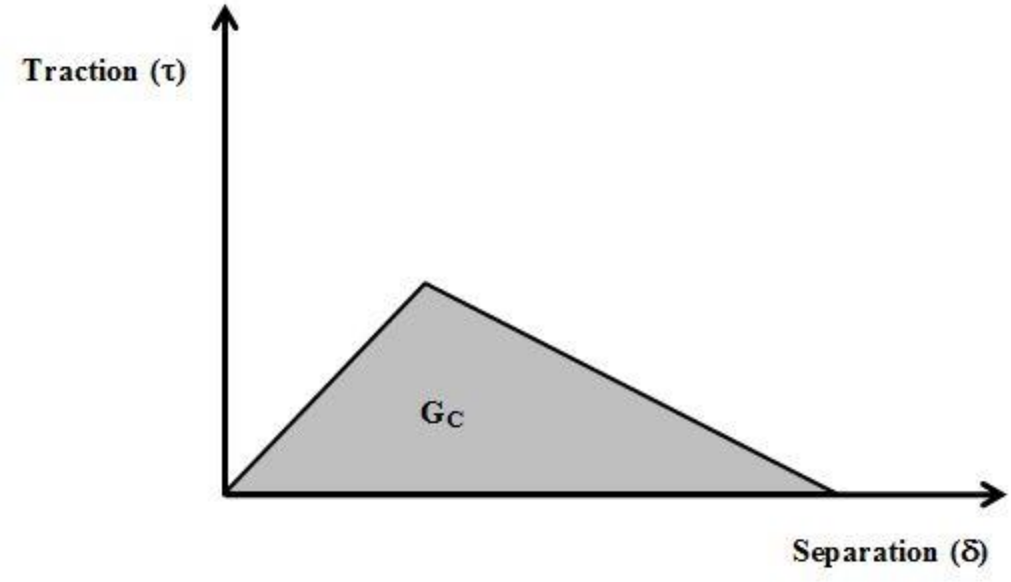

Figure 3.6. Traction separation law for a typical tensile failure

Here δ denotes the separation in m and traction is denoted by τ. The critical failure energy (G_c) is the area under the traction separation curve. The relation between fracture energy and the failure criterion given in Equation 58 is shown in Equation 73. Assuming the final displacement under a certain stress condition is δ_f (Rice, 1968).

$$\int_0^{\delta_f} \tau d\delta = G_C \tag{73}$$

The criterion for the failure initiation and damage evolution (propagation) in cohesive elements follow the same concepts in fracture mechanics. It is discussed in detail in Section 2.3.3.

3.3.3. Material Properties. The simulation was setup as a three step process. 1) The first step simulates the static state of stress in the reservoir. 2) In the second step fluid is pumped into a sealed section of the wellbore. The pump rate and pump time is calculated based on strength parameters of the reservoir and the desired value of fracture length. For this research, the fluid is pumped into the wellbore at a rate of .36 m^3 per second or approximately 136 barrels per minute for a period of 20 minutes (1200 seconds). That amounts to a total pumped volume of 432 m^3 or 2717.2 barrels of fluid. Since only a half model was constructed, the rate of fluid flowing into the model is 0.18 m^3 per second. In addition to this, assuming equal distribution of fluid between all four fractures, the rate of fluid flowing into each fracture is .045 m^3 per second. The increase in pore pressure will initiate the separation of the cohesive elements and the hydraulic fracture is propagated. 3) In the third step, the fluid pumped into the fracture leaks off into the formation while the fracture faces are held in place to simulate an effective placement of proppant in the fracture to prevent the fracture closing again.

As one of the main goals of the generic model setup is to be able to represent a variety of shale types, all material properties were carefully chosen well within the ranges of material property values as reported for Baxter shale and Marcellus shale (Higgins, 1988; Boyer, 2006; Waters, 2011; Eshkalak, 2013). For the FSS, the material properties used for all the models are listed in Table 3.1.

For the AS, the property values of shale are slightly varied (still within the range of values reported) such that all values are still within the range of reported properties even for large anisotropy ratio. Table 3.2 reports values used for the isotropic model. These values are standard values for all models in the AS, except cases reported in Tables 3.3 through 3.6.

Table 3.1. Material properties of shale in FSS models

Density of shale (ρ_b)	2250 $\frac{\mathrm{Kg}}{\mathrm{m}^3}$
Porosity (ϕ)	16.667%
Young’s Modulus (E)	30 GPa
Poisson’s Ratio (ν)	0.25
Permeability (k)	.05 µd
Density of pore occupying fluid (ρ_f)	1000 $\frac{\mathrm{Kg}}{\mathrm{m}^3}$
Fluid Leak-off Coefficient (C)	5.8 x 10^{-13} $\frac{m}{Pa.s}$
Fracture energy	28000 $\frac{N}{m}$

Table 3.2. Material Properties used for AS models

Bulk Density of shale (ρ_b)	2250 $\frac{\mathrm{Kg}}{\mathrm{m}^3}$
Porosity (ϕ)	16.667%
Young’s Modulus (E)	18 GPa
Poisson’s Ratio (ν)	0.25
Permeability (k)	6 µd
Density of pore occupying fluid (ρ_f)	1000 $\frac{\mathrm{Kg}}{\mathrm{m}^3}$
Fluid Leak-off Coefficient (C)	5.8 x 10^{-13} $\frac{m}{Pa.s}$
Fracture energy	28000 $\frac{N}{m}$

Five models were constructed to study the effect of anisotropy in Young's Modulus on fracture aperture. The Young's Modulus magnitudes were varied as shown in Table 3.3 while all other values are the same as listed in Table 3.2

Table 3.3. Variation in Young's Modulus magnitudes based on anisotropy ratio values

Anisotropy Ratio	Horizontal Young's Modulus (Gpa)	Vertical Young's Modulus (Gpa)
1	18	18
1.5	27	18
2	36	18
2.5	45	18
2.9	52.2	18

Two additional models were included in the study to investigate the effect of the magnitude of Young's Modulus while keeping the anisotropy ratio constant at 2.0 as shown in Table 3.4.

Table 3.4. Variation in Young's Modulus magnitudes keeping anisotropy ratio constant

Anisotropy Ratio	Horizontal Young's Modulus (Gpa)	Vertical Young's Modulus (Gpa)
2.0	36	18
2.0	50	25
2.0	60	30

Six models (including the isotropy) were included to study the permeability anisotropy effect. The values of permeability chosen are shown in Table 3.5.

Table 3.5. Variation in permeability values to study different levels of anisotropy

Anisotropy Ratio	Horizontal permeability (μd)	Vertical permeability (μd)
1	6	6
0.8	6	4.8
0.6	6	3.6
0.4	6	2.4
0.2	6	1.2
0.1	6	0.6

Three levels of anisotropy in Poisson’s ratio were also included with the Poisson’s ratio varying as mentioned in Table 3.6.

Table 3.6. Poisson's ratio anisotropy

Anisotropy Ratio	Out of plane Poisson’s ratio (ν_t)	In-plane Poisson’s ratio (ν_p)
0.8	0.25	0.2
1	0.25	0.25
1.2	0.25	0.3
1.4	0.25	0.35

When defining transverse isotropy using ABAQUS, anisotropy in shear modulus also needs to be defined because the two are interlinked in ABAQUS. The relation between the three elastic moduli defined by ABAQUS for orthotropic and transversely isotropic materials is defined as follows:

$$G_i = \frac{E_i}{2(1+\nu_i)} \tag{74}$$

Where G_i is the shear modulus and i denotes either the in-plane direction (plane of isotropy) or the transverse direction.

3.3.4. Pre-Stressing. The reservoir is in a state of equilibrium with its surroundings before any drilling or completion operations that may alter the state of stress. Drilling a borehole will affect that equilibrium and the stresses change in the area around the borehole to achieve equilibrium again. The first step in most oil related numerical simulations is to simulate the state of equilibrium of a reservoir with its surroundings using realistic boundary conditions. Hence, during numerical simulations, applying any load on the model will cause deformation and the model to re-achieve equilibrium. When gravity is applied to the reservoir, the instantaneous application and lack of any previous state of stress will result in unrealistic deformation (i.e. vertical compaction as shown in Figure 3.7). To avoid unrealistic vertical displacements, we specify the stress tensor of each element of the reservoir model as an initial condition before gravity is applied. The results for a simple 3D model with a depth of 1000 meters, with and without pre-stressing, are shown in Figure 3.7 and 3.8.

The reservoir is in a state of equilibrium with gravity acting on it but results from Figure 3.7 show that the applying overburden stress and gravity alone will cause a displacement of upto 1.5 m in a model that is 1000m below the surface. Pre-stressing the model yields results as shown in Figure 3.8 where the displacements suggest that the model is in equilibrium with its surrounds while under the influence of overburden stress and gravity. The pre-stress model is a much more accurate representation of the reservoir in its initial state than the model from Figure 3.7.

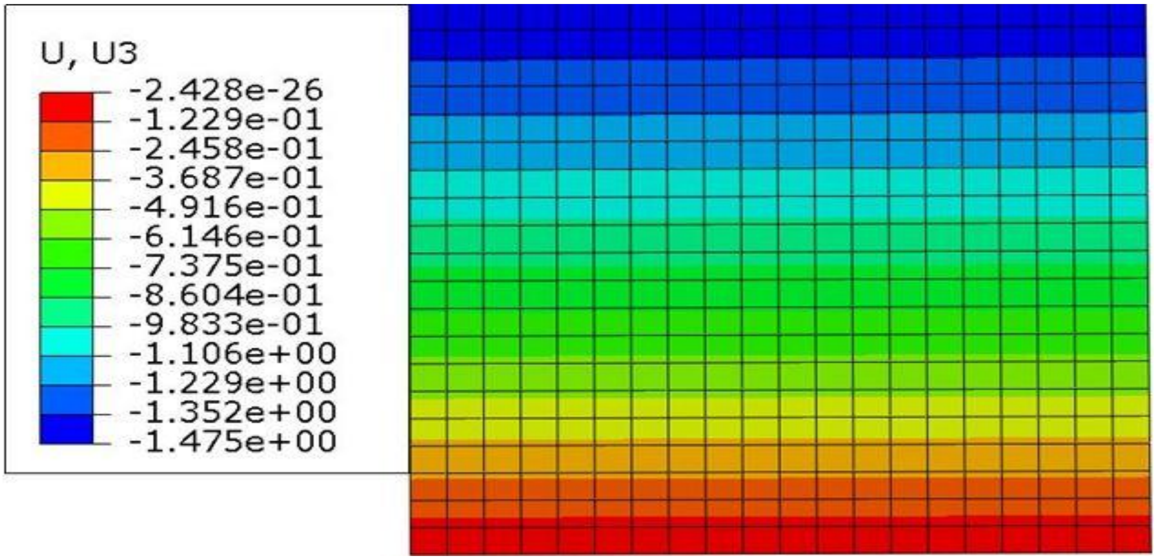

Figure 3.7. Displacement in Z direction in meters before pre-stressing

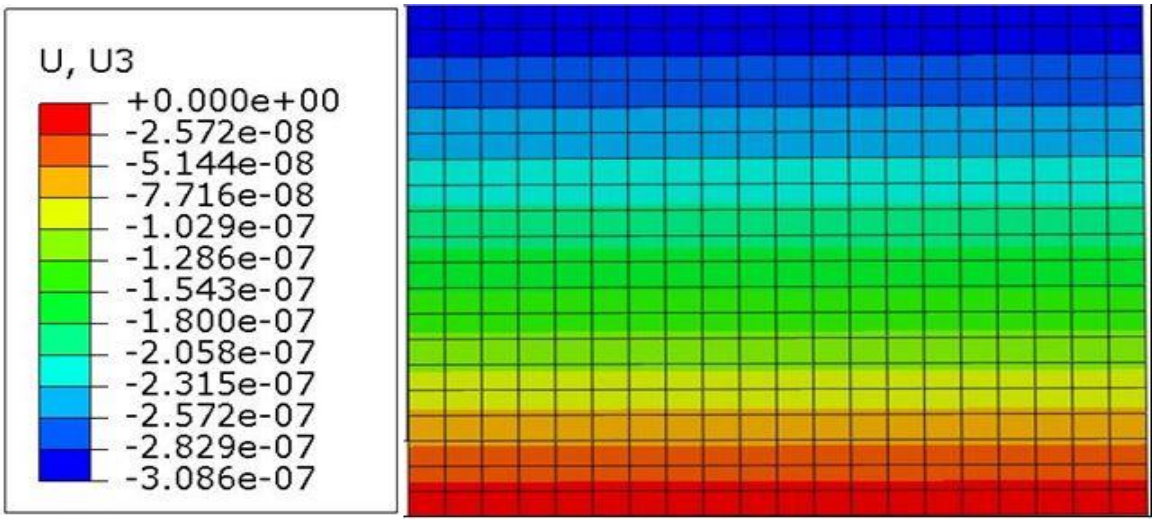

Figure 3.8. Displacements in Z direction in meters after pre-stressing

3.3.5. Loads and Boundary Conditions. As mentioned above, the numerical simulation of multiple hydraulic fracturing is achieved in a three step process with appropriate loads and boundary conditions acting in each step. The first step is a static step to simulate the initial state of the reservoir. The second step is to create a hydraulic fracture by pumping fluid into the perforations and the third step is to simulate the propped open fracture and the fluid leak off into the reservoir. In the following sections, the loads and boundary conditions applied will be discussed in detail.

3.3.5.1 Loads. The primary load acting in the first step is the load due to gravity. Other loads that are applied in the first step are the overburden and the wellbore pressure caused by the mud weight. Since the chosen reservoir for this model was assumed to be 2100 m below the surface, assuming the average bulk density of overlying to be 2500 $\frac{\mathrm{Kg}}{\mathrm{m}^3}$, the effective overburden acting on top of the model was given as 27.222 Mpa. Mud weight is the density of the drilling fluid chosen carefully to prevent formation fluids entering the wellbore which could prove to be fatal. The formation fluids are under pressure and the wellbore could act as a release causing the formation fluid to violently rise up the wellbore to the surface (kick out) causing damage to the surface equipment and personnel. The pressure acting on the borehole surface was chosen to be the same pressure as the pore pressure (at 2100m depth, P_p = 20.601 MPa) because that would prevent any fluid leaking off into the formation or any formation fluids from entering the wellbore.

In the second step, in addition to the already acting loads mentioned above, the pumping of fluid is defined as a load. The rate at which fluid is pumped is given as a load at certain nodes in the cohesive elements. The rate of fluid pumped into each fracture is given as 0.045 m^3 per second.In the third step, all loads acting in the first step are still active while the pump rate of fluid is changed to zero. This allows time for the fluid to leak off into the formation.

3.3.5.2 Boundary conditions. Since the model is built assuming uniaxial strain, no out of plane displacements are allowed on the boundaries of the model for all the steps. This is achieved using rollers. Rollers are a way of describing boundary conditions where the nodes are free to move inside the plane but the out of plane displacements are zero. In contrast, pins are a way of describing boundary conditions that fix or pin the nodes not allowing displacements in any direction.

In the first step, all model boundary faces are constrained using rollers so as to not allow any out of plane displacements. In the second step, the boundary conditions mentioned for the first step are still in place. Additional boundary conditions for pore pressure are assigned for the top surface (18.148 MPa) and bottom surface (20.601 MPa). This is to prevent any unrealistic pore pressure changes caused by the continuous pumping of fluid into the model domain.

In the third step, since the fracture is already formed, boundary conditions are used to simulate the proppant placement that prevents the fracture from closing again. For this purpose, the nodes of all cohesive elements are pinned so as to not allow movement in any direction. In the third step, the fluid leaks off into the formation while the fracture surfaces are held in place to simulate a 100% effective proppant placement.

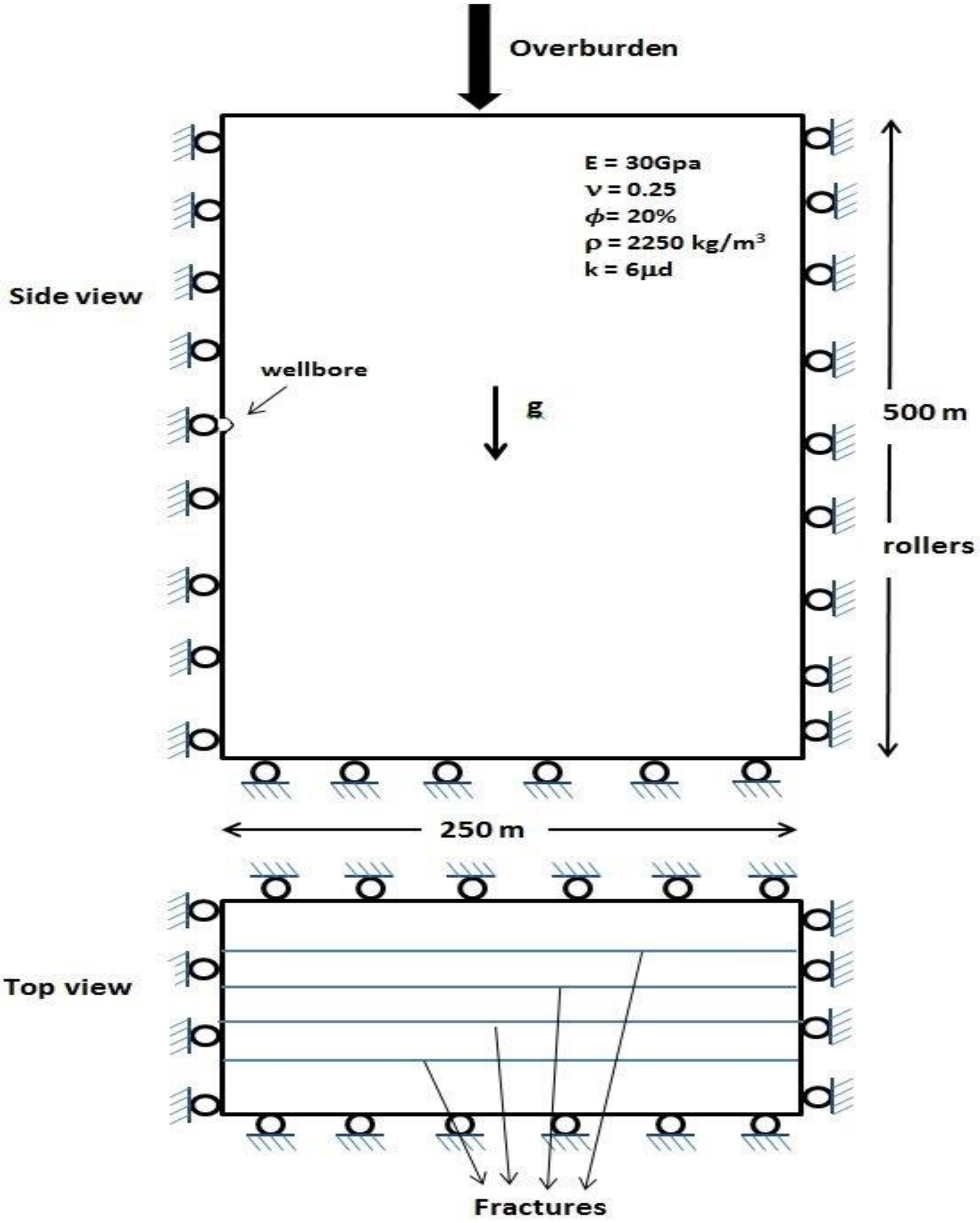

Figure 3.9. Model sketch of the hydraulic fracture simulation model

4. RESULTS

4.1. BOUNDARY EFFECT

Numerical simulations of hydraulic fracturing are done to extensively study the fracture width and its relation to fracture spacing and anisotropy of Young’s Modulus, Poisson’s ratio and permeability. The results included in this thesis are for a set of data chosen within the range of values reported for shales in the U.S. The numerical models can be used for a set of data specified by the user to study the fracture widths.

The aim of the study is to investigate the controlling effect the edge fractures have on the center fractures. While the center fractures are affected by the stress shadows caused by the edge fractures, the edge fractures must not be under the influence of any boundary effect to fully justify this study. Considering the computational time involved for each simulation, a harmony has to be found to keep the computational time realistic while minimizing the boundary effect on edge fractures.

To understand the effect the boundaries of the reservoir have on the fracture widths of edge and center fractures, two additional models were built with different spacing between the edge fractures and the model boundary. The ratio of distance between fractures (fracture spacing) to distance between edge fracture and the model boundary (boundary spacing) is 1.5 for the narrow model and 2 for the standard model. The fracture width results to study the effect of model boundaries on edge and center fractures are listed in Table 4.1.

Table 4.1. Fracture widths of edge and center fractures for the standard and narrow models

Ratio of fracture spacing to boundary spacing	Edge fracture width (m)	Center fracture width (m)
1.5 (narrow)	1.02×10^{-2}	8.05×10^{-3}
2.0 (standard)	1.15×10^{-2}	8.11×10^{-3}

The results observed in Table 4.1 indicate that there is a significant increase in fracture widths for edge fractures of around 1.3 mm while the change in widths of center fracture fractures is around 0.06 mm. This proves that the boundary effect for models with fracture spacing to boundary spacing ratio of 2.0 is much smaller compared to the model with a ratio of 1.5, thereby minimizing the effect if not completely eliminating it. The change is depicted in Figure 4.1 for comparison.

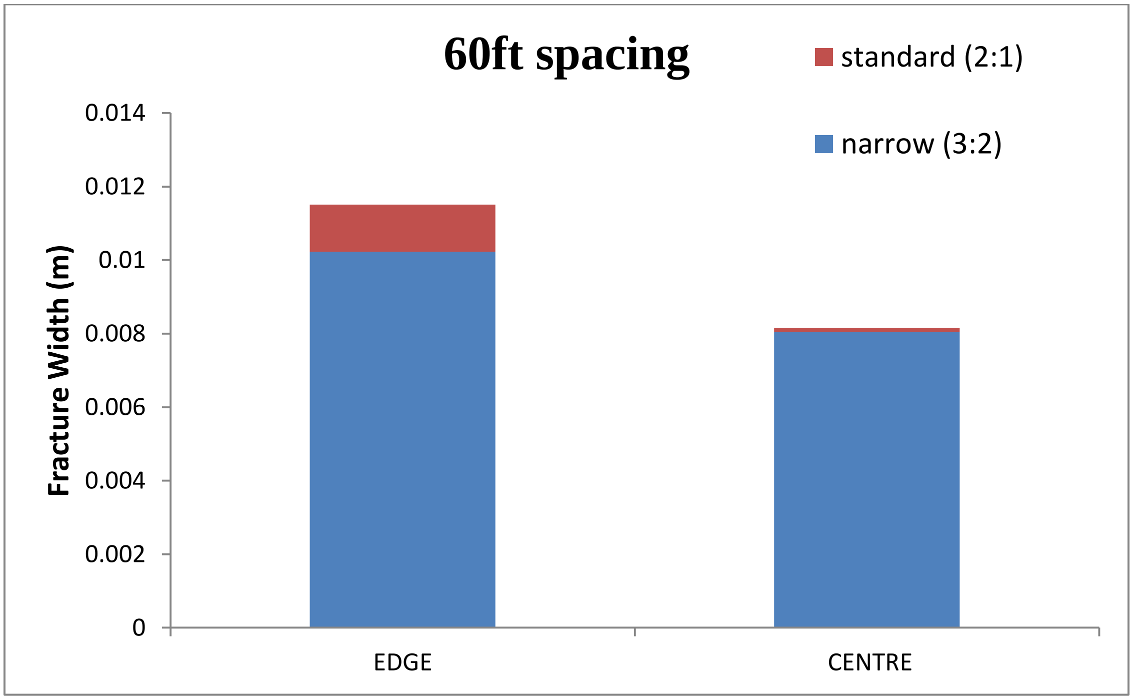

Figure 4.1. Difference in fracture width based on model dimensions

All results that are presented here in later sections are associated with models with the fracture spacing to boundary spacing ratio of 2.0 to justify the observations and ensure that the boundary effect has a minimal role. This, however, comes at a cost in terms of computational time as these models take approximately 30-36 extra hours of real time computing for the simulation to be completed.

4.2. FRACTURE WIDTH RESULTS

This research can be divided into two major parts: ‘Impact of fracture spacing on fracture width’ and the other being ‘Anisotropy effects on fracture spacing’. Hereby, they will be referred to as the fracture spacing study [FSS] and anisotropy study [AS], respectively.

As observed in Figure 4.2, the maximum fracture width in a fracture plane is observed at the top of the fracture plane away from the borehole region. Previous studies and observations report that the maximum fracture width is almost always observed in the near wellbore region for vertical wells (Yew, 1997; Warpinski, 1991) and horizontal wells (Chen and Economides, 1995). Due to software capability limitations, all models are setup in such a way that the fracture is first created in the fracture plane and when the fluid pump rates are maintained at a constant rate after the creation of fracture, the fracture is propped open further. Due to the extensional stress state (based on the uni-axial strain model) considered, the horizontal stress increases with depth and the maximum fracture width is observed at the top where the lowest horizontal stress magnitudes occur. The typical fracture plane observed across all models depicting fracture widths are shown in Figure 4.1. All values presented below are the maximum fracture widths encountered in a fracture plane.

The method of fracturing employed in this study yields realistic results that are similar in magnitude and range of fracture width values reported in other studies. Numerical analysis by Cheng (2009) report edge fracture widths of about 10mm and center fracture widths of about 5mm while an analytical study by Khan (2012) on a single fracture report fracture width values of 15 mm. The approximate fracture widths of edge fractures in this study are 12 mm and that of center fractures are 8mm which are similar in magnitude and in agreement with the other findings.

4.3. STRESS RESULTS

The stresses in and around a fracture change significantly when fractures are created. In this study, the stress component in the direction that is perpendicular to the fracture planes and along the horizontal borehole is studied. The numerical results and analytical results of effective stresses are compared before and after perforation at the borehole wall and shown in Figure 4.3. The numerical results and analytical results for the stress magnitude along the wellbore wall are in perfect agreement before the creation of fractures. The analytical solution of effective stress change in the minimum horizontal direction around a fracture depending on the fracture width and fracture spacing is unavailable at this point of time.

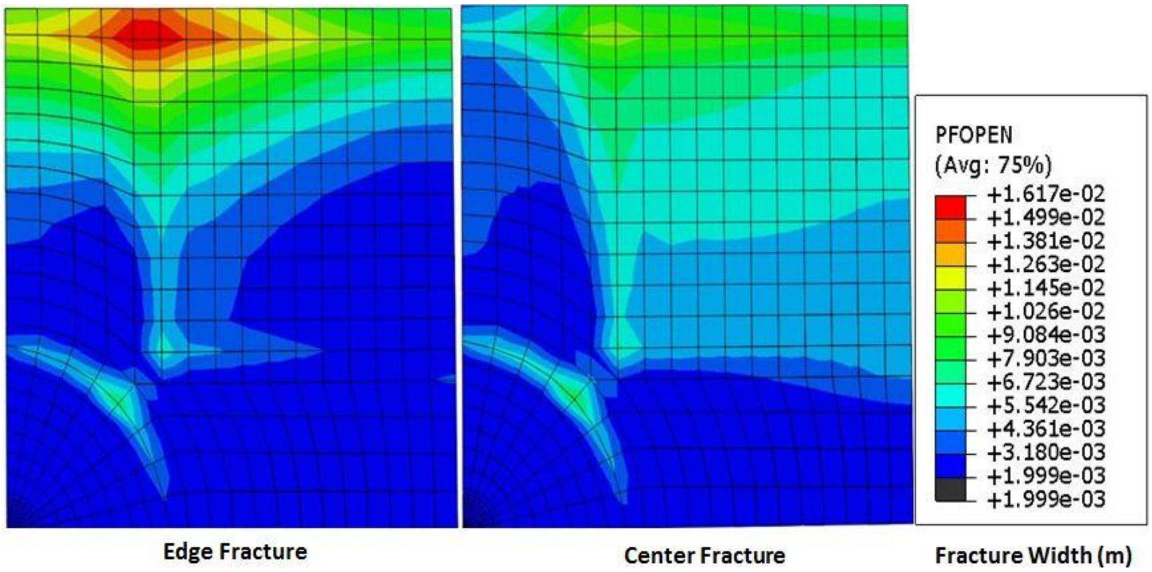

Edge Fracture **Center Fracture** **Fracture Width (m)**

Figure 4.2. Contour plots of fracture planes of edge and center fractures depicting fracture widths

In the minimum horizontal stress direction i.e. the direction perpendicular to the fracture planes, the minimum horizontal stress changes over a wide range all the way up to the boundaries of the model domain. The stress change is highest in and around a fracture depicting the stress interference or stress shadow.

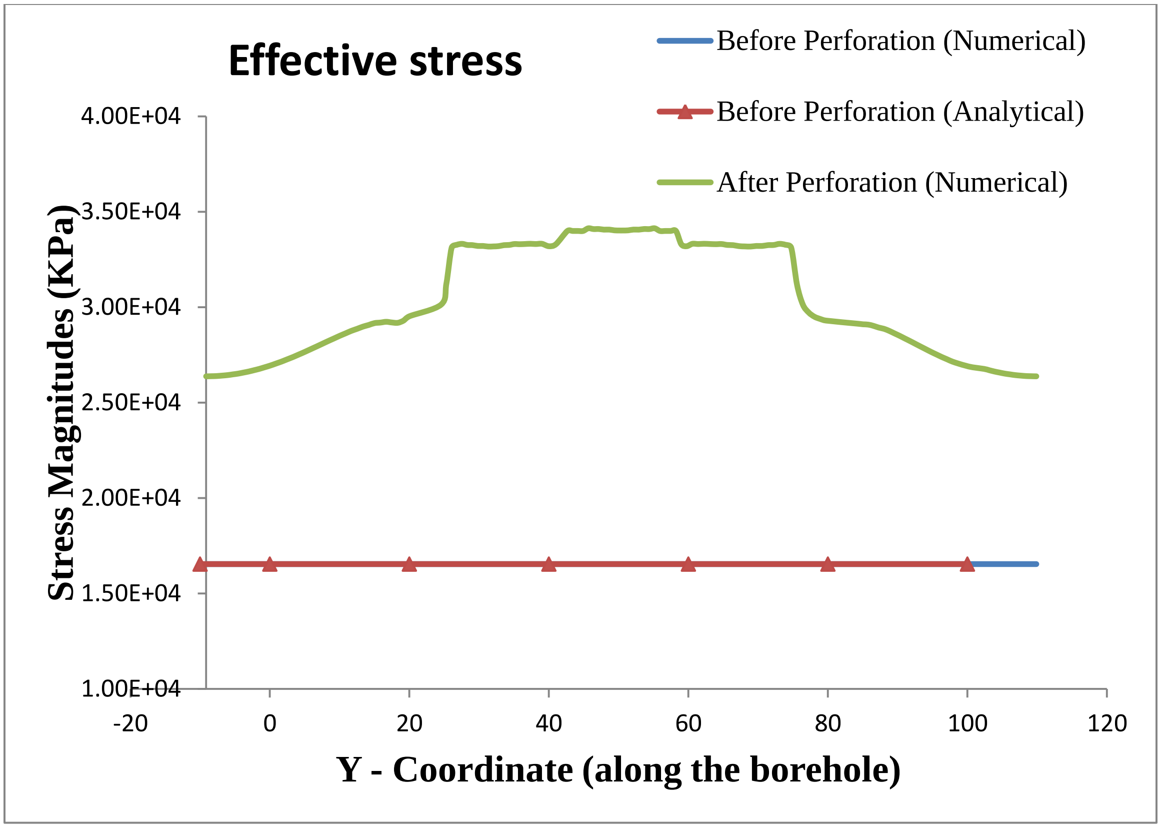

Figure 4.3. Minimum horizontal effective stress variation along the borehole before and after perforation comparing numerical and analytical results

The minimum horizontal stress change increases around the fractures particularly between the center fractures. The magnitude of stress change is at its highest near the center fractures reaching values of around 17.5 MPa. Figure 4.4 depicts the stress change in the model. The stress change in this model suggests that the stresses developing in an around fractures impede the fracture widths.

4.4. FRACTURE SPACING

The results of numerous simulations to study the effect of fracture spacing on fracture widths are presented here. The maximum fracture widths encountered in the fracture planes of both edge fractures and center fractures are compared. The results are shown in Table 4.2. Five models with increasing spacing between fractures were studied for this case.

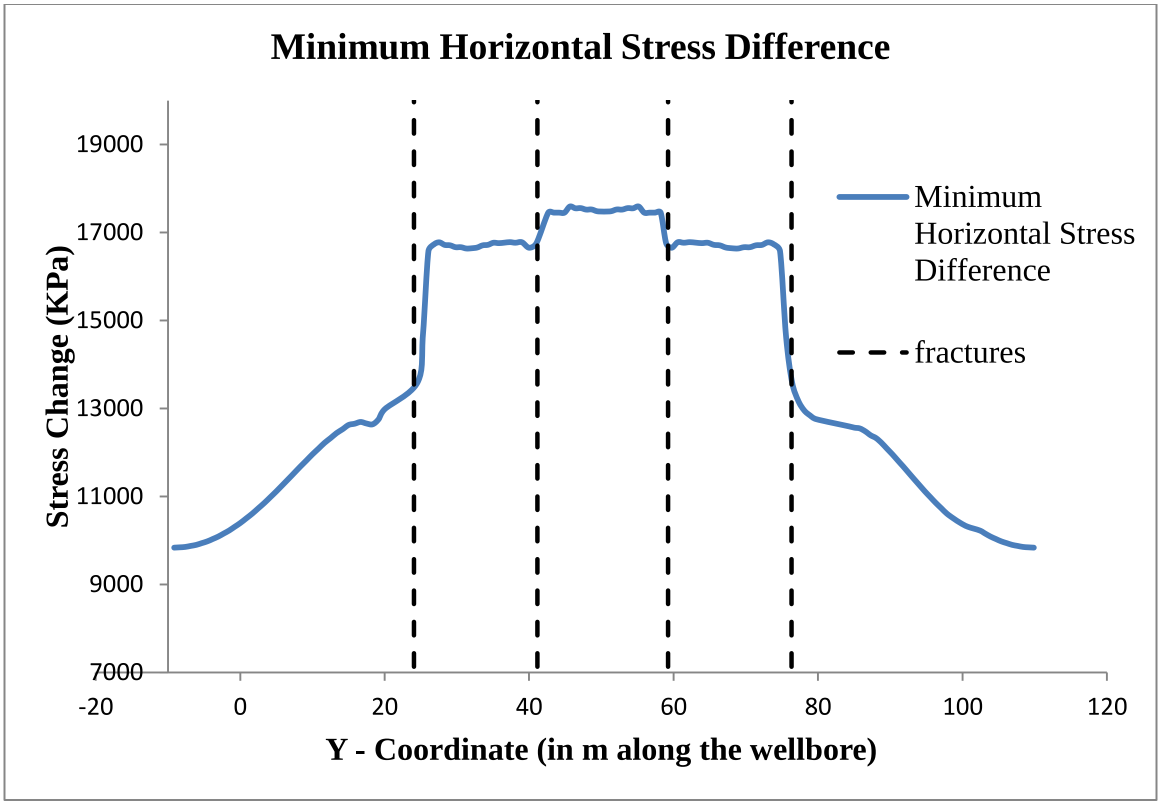

Figure 4.4. Minimum horizontal stress change in the model along the wellbore

Table 4.2. Fracture width results in m for different models with varying fracture spacing

Fracture Spacing (ft)	Edge fracture width (m)	Center fracture width (m)
40	9.87×10^{-3}	5.00×10^{-3}
50	1.06×10^{-3}	6.25×10^{-3}
60	1.15×10^{-2}	8.16×10^{-3}
80	1.30×10^{-2}	1.15×10^{-2}
100	1.33×10^{-2}	1.26×10^{-2}

The results in Table 4.1 show that there is a consistent increase in fracture widths of both center and edge fractures with increasing fracture spacing. The increase in fracture widths of center fractures increases by more than a factor of 2 over the spacing range of 40 to 100 ft. the center fracture widths increase by 7.6 mm while the edge fractures increase by just 3.4 mm over the entire range of fracture spacing. The change in fracture width is shown in Figure 4.5.

The effect on center fractures is higher compared to the edge fractures. As the fracture spacing increases, the difference between the fracture widths of center and edge fractures decrease.

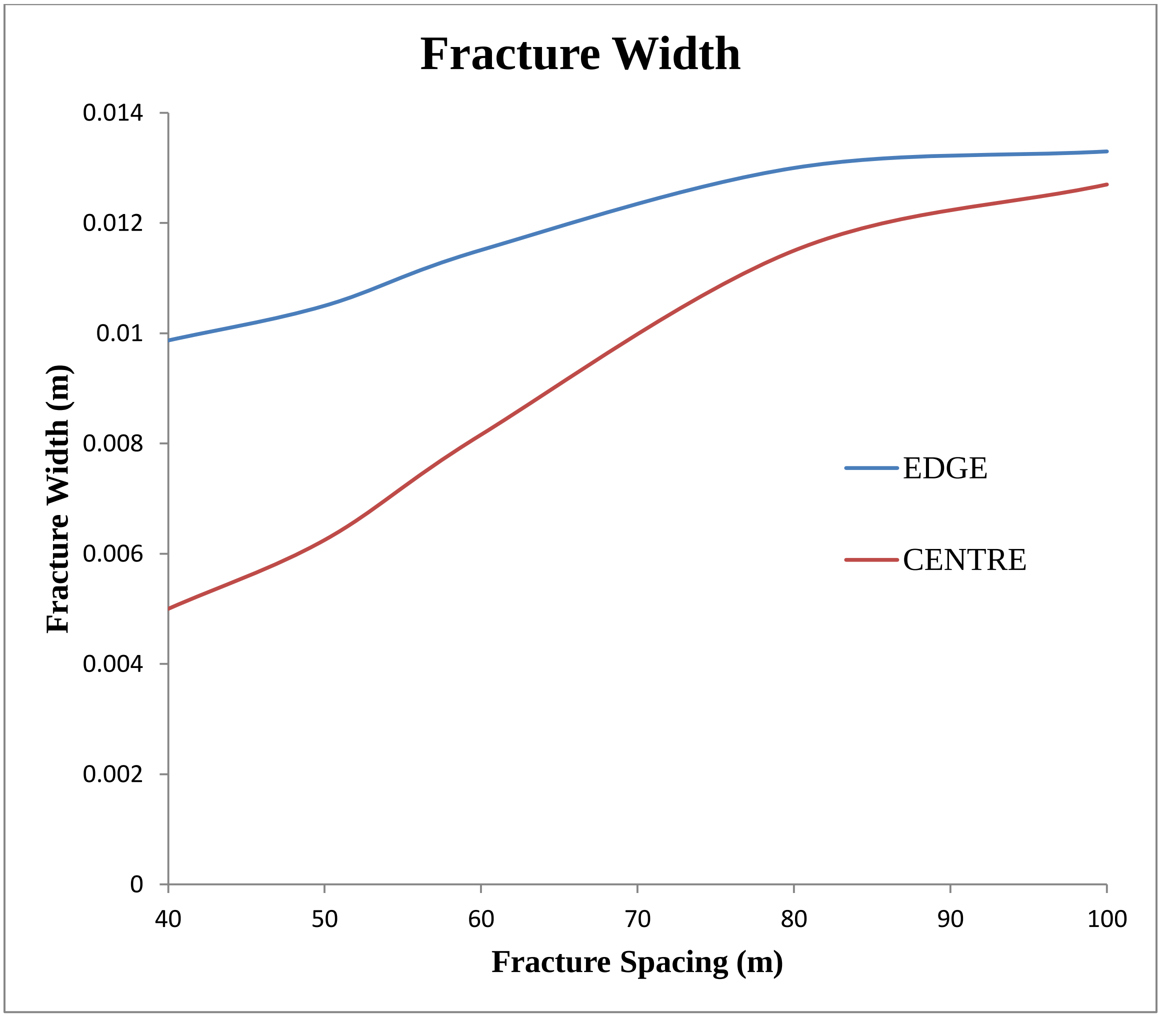

Figure 4.5. Fracture width variation in edge and center fractures based on fracture spacing

4.5. ANISOTROPY RESULTS

Results from numerical models that include different levels of anisotropy in Young's Modulus, Poisson's ratio and permeability are presented below. Anisotropy in shales is combined with multiple hydraulic fracturing that allows investigation of the effect of anisotropy individually on edge and center fractures. All simulations for this part (AS) are done using the standard 60 ft fracture spacing models.

4.5.1. Young's Modulus Anisotropy. Shales are transversely isotropic regarding Young's Modulus where the magnitudes are similar in the horizontal directions but vary in the vertical directions. The commonly observed characteristic of shale is that the Young's Modulus in the horizontal direction is higher than the vertical counterpart. A basic isotropic model where the values remain constant irrespective of direction is included to enable us to compare the results with anisotropic models. The levels of anisotropy are measured using the anisotropic ratio. In this case, the ratio is the horizontal Young's Modulus to the vertical Young's Modulus is modified in each model from 1.0 to 3.0. The fracture widths of simulations with the Young's Modulus anisotropy are shown in Table 4.3.

The effect of Young's Modulus change on fracture widths is significant as observed in Table 4.3. With increasing anisotropy ratio in Young's Modulus, the fracture widths of both edge and center fractures decrease. There is a significant change in the fracture widths of center fractures. The change is depicted in Figure 4.6.

Two additional models were included in this study to investigate the effect of the magnitude of Young's Modulus for the same anisotropy levels. The anisotropy ratio was kept constant at 2.0 and the E magnitudes were altered. The results for this are presented in Table 4.4.

The results in Table 4.4 depict that there is a significant change in fracture widths. Increasing Young's Modulus magnitudes whilst keeping the anisotropy ratio constant does have a significant effect on the fracture widths of both center and edge fractures. Increasing magnitudes in Young's Modulus result in decreasing fracture widths for both edge and center fractures. The drop in edge fracture widths across the range of Young's modulus change is 3.5 mm. The change in width for center fractures is more than twice than that of edge fractures at 7.2 mm. A probable explanation is that increasing Young's Modulus, whilst the external forces remain the same, inhibits fracture width growth.

Table 4.3. Fracture width results of edge and center fractures with varying levels of anisotropy in Young's Modulus

Anisotropy ratio $(\frac{E_h}{E_v})$	Edge fracture width (m)	Center fracture width (m)
1	1.59×10^{-2}	1.29×10^{-2}
1.5	1.64×10^{-2}	8.51×10^{-3}
2.0	1.60×10^{-2}	7.49×10^{-3}
2.5	1.52×10^{-2}	7.28×10^{-3}
3.0	1.46×10^{-2}	7.25×10^{-3}

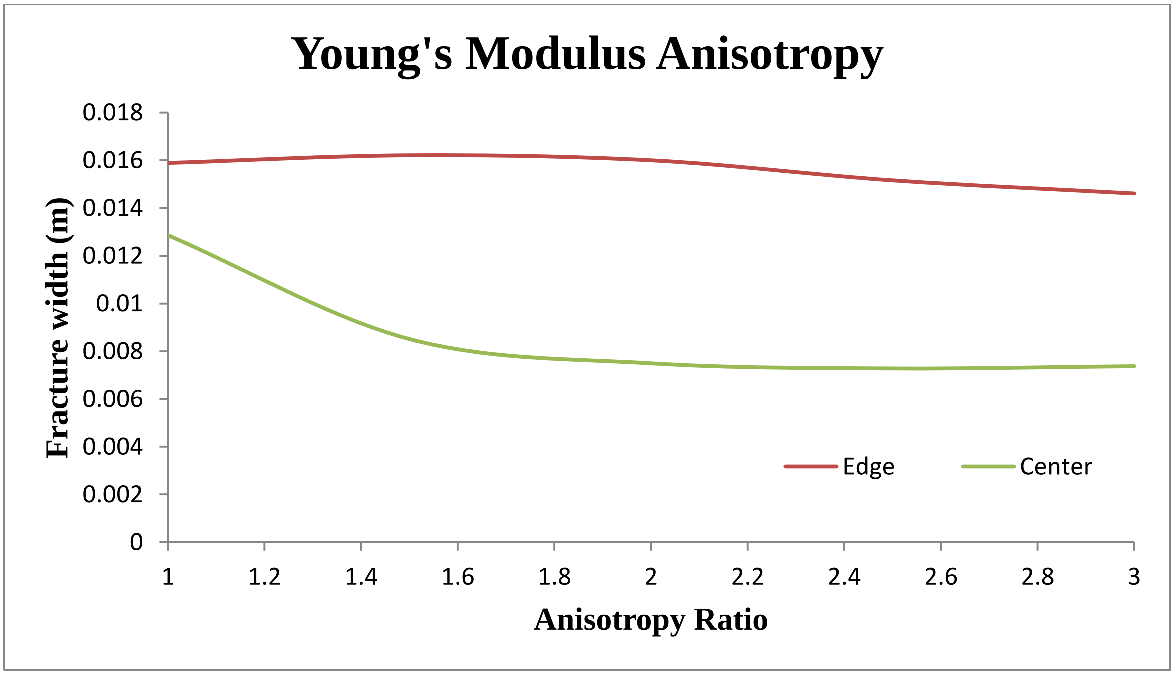

Figure 4.6. Fracture aperture variation with anisotropy ratio

Table 4.4. Fracture width results of edge and center fractures for different magnitudes of Young's Modulus with same anisotropy

Anisotropy ratio ($\frac{E_h}{E_v}$)	Edge fracture width (m)	Center fracture width (m)
$\frac{36}{18}$	1.59 x 10^{-2}	7.49 x 10^{-3}
$\frac{50}{25}$	1.35 x 10^{-2}	6.81 x 10^{-3}
$\frac{60}{30}$	1.24 x 10^{-2}	6.77 x 10^{-3}

4.5.2. Permeability Anisotropy. Shales are flaky in nature and are well consolidated which causes the vertical permeability (k_v) to be much lower compared to the horizontal permeability (k_h). The aim is to investigate the effect permeability anisotropy has on the fracture widths combined with the fracture spacing between fractures. The anisotropy in this case is measured in terms of the ratio between vertical permeability to horizontal permeability. Several simulations were conducted with anisotropy ratio varying between 1 and 0.1. The fracture width results are listed in Table 4.5.

The difference in fracture widths is not very significant in both edge and center fractures. The variation in the fracture width for the entire range of permeability ratios is less than 1mm. The same is depicted in Figure 4.7.

4.5.3. Poisson's Ratio Anisotropy. For transversely isotropic materials like shales, the Poisson's ratio varies with direction. Poisson's ratio is a material property that quantifies strain in directions perpendicular to the direction of the acting stress. Two different Poisson's ratio is to be defined for a transversely isotropic material. In this case, first is the one that quantifies strain in the horizontal plane of isotropy due to stress in the transverse direction and the other quantifies strain in the transverse direction due to stress. One is called the in-plane Poisson's ratio and the other is called out of plane Poisson's ratio.

Table 4.5. Fracture width results of edge and center fractures for different levels of permeability anisotropy

Anisotropy ratio ($\frac{k_v}{k_h}$)	Edge fracture width (m)	Center fracture width (m)
0.1	1.61 x 10^{-2}	1.206 x10^{-2}
0.2	1.66 x 10^{-2}	1.258 x10^{-2}
0.4	1.63 x 10^{-2}	1.267 x10^{-2}
0.6	1.63 x 10^{-2}	1.294 x10^{-2}
0.8	1.60 x 10^{-2}	1.286 x10^{-2}
1.0	1.59 x 10^{-2}	1.285 x 10^{-2}

Three anisotropic levels in addition to the isotropic model are built for this purpose. Table 4.6 presents the results for anisotropy in Poisson's ratio. The Poisson's ratio variation does not seem to have any significant effect of fracture widths of either edge or center fractures. The variation of width in edge fractures is less than 0.3 mm while the variation in center fractures is around 1.5 mm. The fracture widths are shown in Figure 4.8.

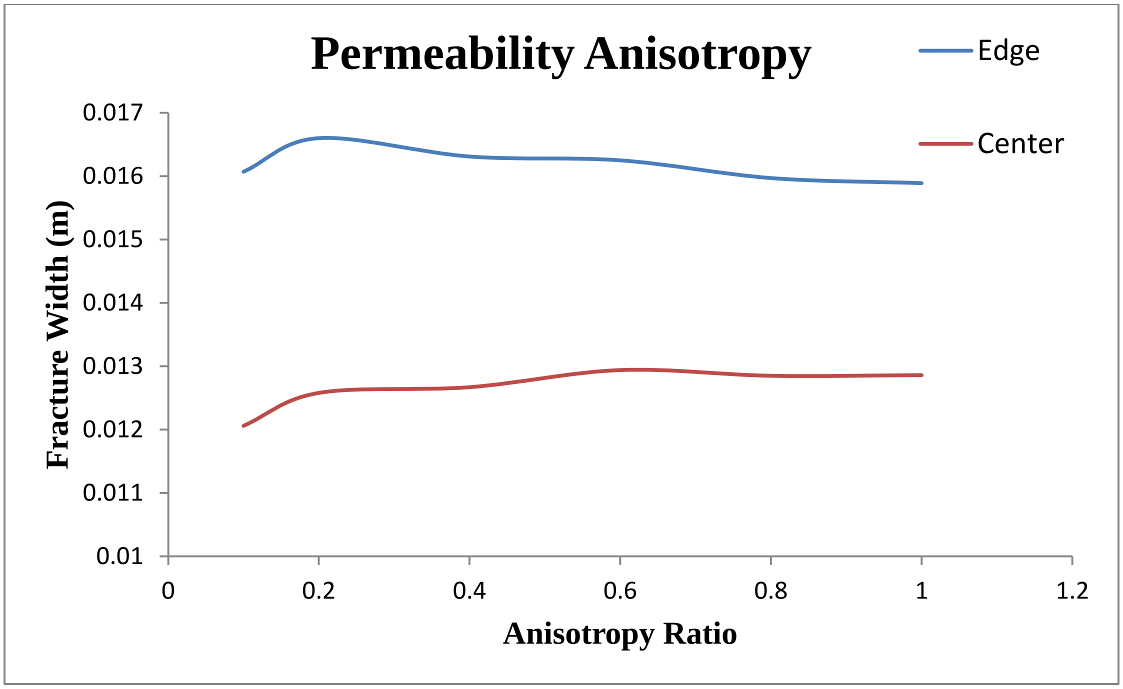

Figure 4.7. Edge and center fractures width variation with permeability anisotropy ratio

Table 4.6. Results of edge and center fractures for anisotropy in Poisson's ratio

Anisotropy ratio ($\frac{\nu_p}{\nu_t}$)	Edge fracture width (m)	Center fracture width (m)
0.8	1.617 x 10^{-2}	1.449 x10^{-2}
1.0	1.589x 10^{-2}	1.286 x10^{-2}
1.2	1.612 x 10^{-2}	1.32x10^{-2}
1.4	1.614 x 10^{-2}	1.451 x10^{-2}

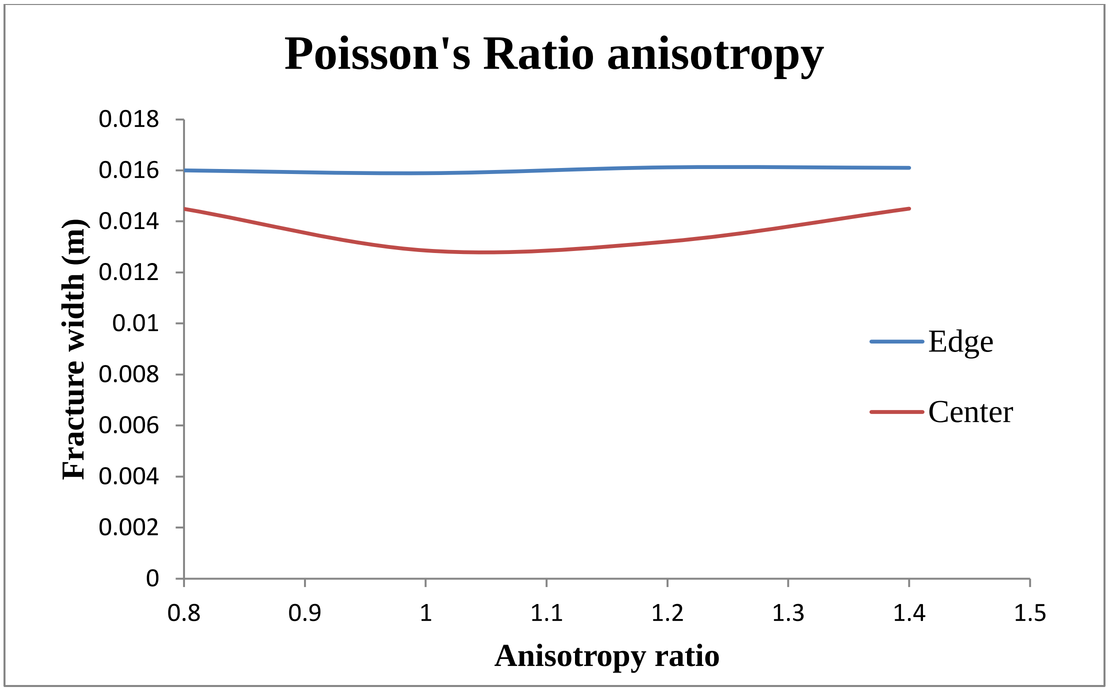

Figure 4.8. Fracture width variation for different Poisson's ratio anisotropy levels

5. DISCUSSION

The optimal way to develop an ultra-low permeability shale reservoir is to create multiple transverse fractures in a horizontally drilled well. This research studies the controlling effects of fracture spacing on fracture aperture and the stress variations around a fracture. It also focuses on the combined effect of fracture spacing and effect of different levels of elastic and permeability anisotropy that is inherent to shales on fracture aperture. The effect of anisotropy will be studied for edge and center fractures individually. Previous studies investigated the effect of fracture spacing on fracture aperture, most notably by Cheng (2010). The relation between net production of hydrocarbons from a reservoir and number of fractures has been discussed at length by Soliman (1999) and Ozkan (2009). The results for fracture spacing studies (FSS) and Anisotropy studies (AS) have been presented in Section 4.

5.1. FRACTURE SPACING

Table 4.1 presents results of the fracture apertures of edge and center fractures for different spacing between the fractures. The edge fractures have considerably higher fracture apertures compared to the center fractures. This matches observations from previous studies (Cheng, 2009). Each created fracture affects the stress around it as shown in Figure 5.1. Any fracture created within this area is affected and has a lower fracture aperture compared to a fracture created without impediment (Nagel, 2013). The stress affected area around a fracture is termed the stress shadow. The numerical model results mimic the findings of a similar three fracture model by Cheng (2009). Figure 5.2 depicts the fracture widths of both center and edge fractures in comparison with the modeling results by Cheng (2009).

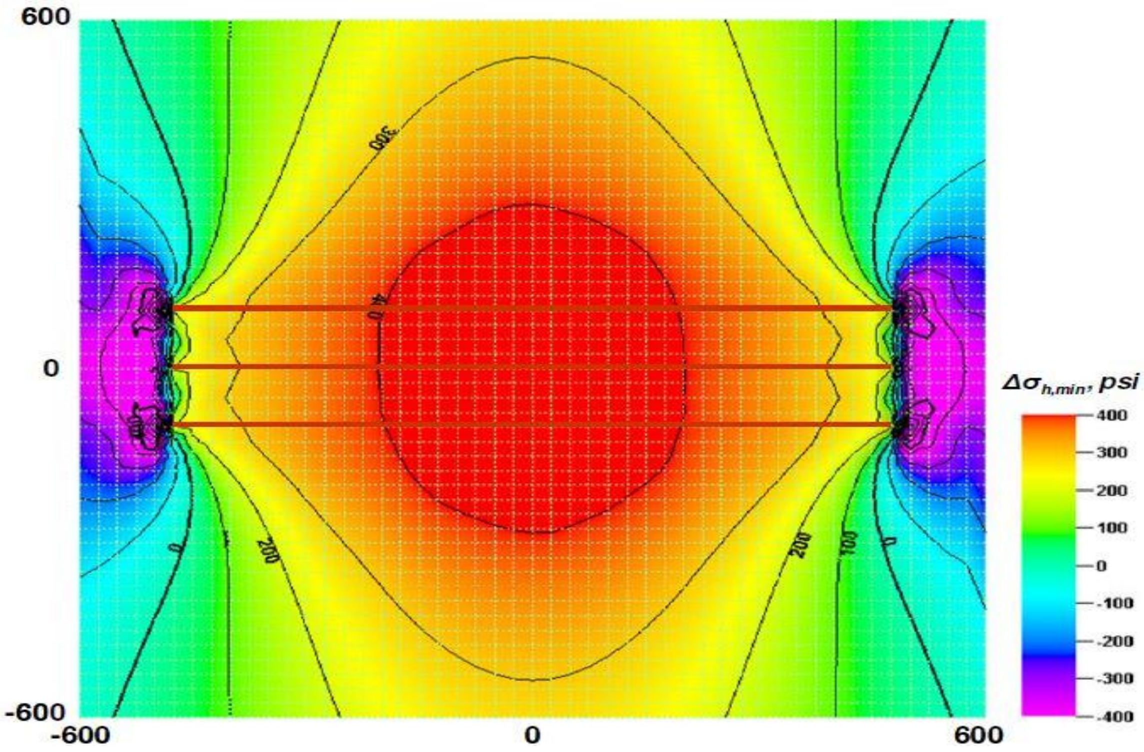

Figure 5.1. Minimum horizontal stress change in a three fracture model (Cheng, 2009)

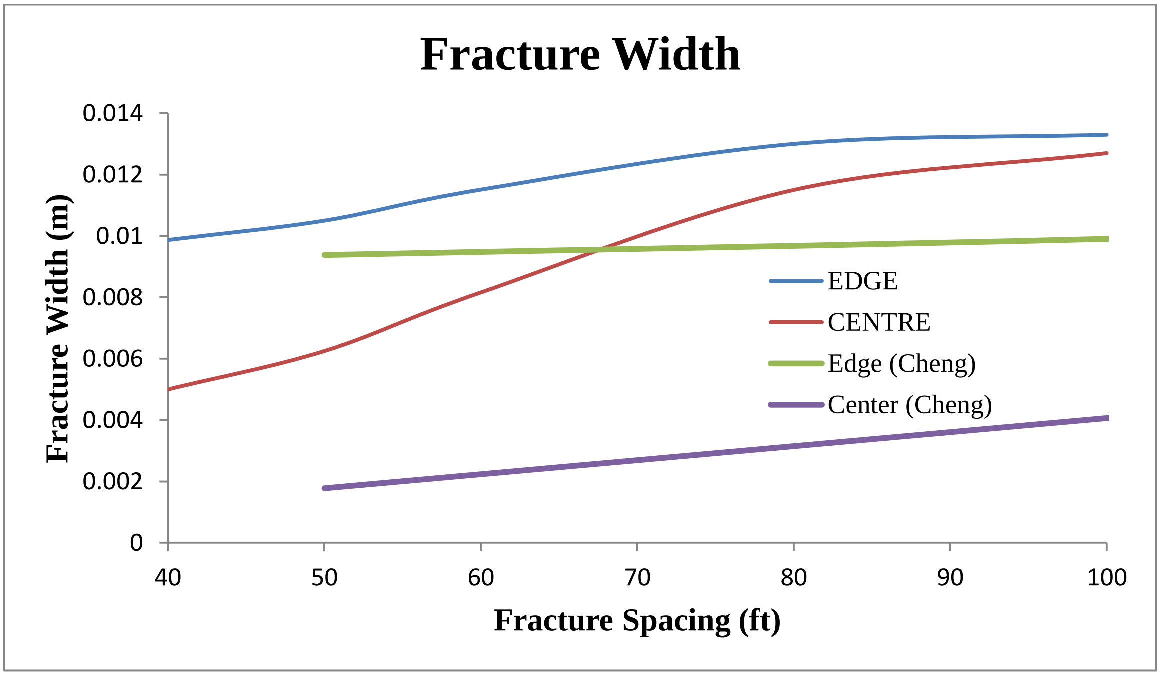

Figure 5.2. Fracture width results compared to results by Cheng (2009)

It is evident from Figure 5.2 that fracture aperture of the edge fractures is higher than the fracture aperture of the center fractures and this is also observed for results reported by Cheng (2009). The fracture apertures increase with increasing spacing and the effect seems to be far greater on the center fractures compared to the edge fractures in both sets of results. The difference between the fracture apertures is very large for narrow spacing and the difference seems to decrease with increasing spacing to a point where the difference between fractures apertures of edge and center fractures is very low.

When the results are compared to results presented by Cheng (2009), there is a higher difference between fracture widths of edge and center fractures in the three fracture model (Cheng, 2009) compared to findings of this study. In the three fracture model, with increasing spacing between fractures, the fracture width increase is higher for the center fracture than that of edge fractures. For a fracture spacing of 100 ft, the difference between edge and center fracture widths is still significant compared to the difference observed in this study. Differences in model setup, number of fractures and shale properties used could be a possible explanation for such differences as discussed in detail later in this Section.

To fully understand the stress effect of edge fractures on center fractures, a new term was defined known as the ‘fracture width ratio’ (FWR). The FWR is the ratio of the edge fracture width to the center fracture width. For fractures spaced far away so that they have no effect on each other, the FWR will have a value of 1 as the edge and center fractures will have the same widths. In contrast, for small fracture spacing, the FWR will have a value greater than 1 because the widths of the edge fractures are greater than that of center fractures. The FWR variation with fracture spacing is shown in Figure 5.3.

For 40 ft spacing, the value of the FWR is 1.97 which illustrates that the center fractures are well within the stress shadows of fractures on either side. The fracture width of edge fractures is twice the fracture width of center fractures with a spacing of 40 ft. As the spacing increases, the FWR reduces rapidly and at a spacing of 100 ft, the value of FWR becomes 1.05. This shows that the fractures, when placed 100ft apart, have minimal effect on each other. If the fractures were placed further apart, the effect also shrinks further to a point where each fracture behaves individually. At this point the value of FWR will become 1 since the fracture widths of both edge and center fractures are the same.

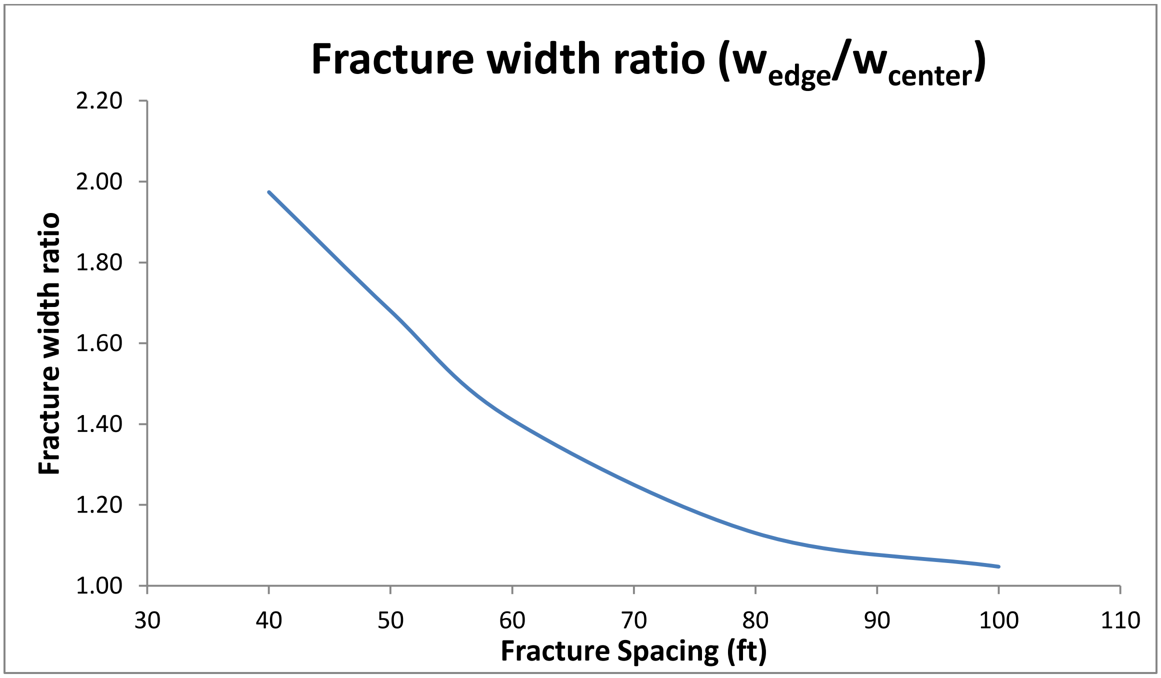

Figure 5.3. Fracture width ratio (FWR) variation with fracture spacing

For the fracture spacing range used in this study, the center fractures are created in the stress shadows of the fractures to either side of it. Similar to the center fractures, the edge fractures are affected by the stress shadow of the fracture next to it on one side and the model boundary on the other. The stress variation or the stress change intensity in a stress shadow is at its highest just around the fractures and fades away as the distance between the fracture and the point of observation increases. From Figure 5.2, it is observed that the edge fracture width variation for models with fracture spacing greater than 70 ft is very modest while the center fracture width variation is still significant. This is because for models with fracture spacing 80 and 100ft, the edge fractures have a boundary that is 160 ft and 200ft away making the effect of the model boundary negligible. The only effect is by the stress shadow of the center fractures, which is also significantly reduced because the fractures are spaced well apart compared to models with spacing of 40, 50 and 60 ft, respectively.

Plotting a FWR for results from the Cheng model, we observe that it follows the same trend although the ratio values are much higher compared to the FWR from this study. The Fracture width ratios calculated using results from a study by Cheng (2009) are depicted in Figure 5.4. The fact that the FWR follows the same pattern and yet the ratios and the magnitudes of the fracture widths themselves vary widely reiterates the importance of devising a custom plan for a hydraulic fracturing job based on the locally prevailing rock properties and anisotropy ratios.

The FWR values of this study and those calculated using results presented by Cheng (2009) differ significantly. Both studies were performed using an isotropic linear elastic medium. Although both studies analyze the effect of fracture spacing on edge and center fracture geometries, the differences in numerical studies cannot be neglected. Analysis by Cheng (2009) was based on the boundary element method where a three fracture model was setup. The fracture width results are based on a model with two edge fractures and a single center fracture. Comparing the three fracture model (Cheng, 2009) with a five fracture model (Cheng, 2012), it is evident that the stress concentrations are at its peak at the inner most fractures. Multiple fractures enhance the stress shadows due to which the lowest fracture width is observed at the innermost fracture (Cheng, 2012). More fractures, since they are under the influence of enhanced stress shadows, result in smaller differences between the fracture widths of edge and center fractures. Actual magnitudes of fracture widths from this study cannot be compared to the results by Cheng (2009) due differences in model setup and material properties used.

Furthermore, a slightly more compressive stress regime ($S_v > S_H = 0.8\ S_v > S_h = 0.6\ S_v$) was used throughout the study by Cheng (2009, 2012) while an extensional stress regime (uni-axial strain model where $S_h = S_H = 0.6\ S_v$) was used in this study. Since, the horizontal stresses in both models are a function of the overburden, the magnitude of vertical stress at the borehole plays a significant role. The difference in the in-situ stress regimes affect the fracture widths of both edge and center fractures and is further discussed in Section 5.3.4. Material properties, especially the elastic moduli like the Young's modulus, play an important role. Fracture widths are directly proportional to the rate of fluid pumped into the wellbore. Difference in injection rates used in this model and by Cheng (2012) could be a major factor in the difference in magnitudes of fracture widths observed by both models. Fluid injection rate used in this study is 136 barrels per minute while the magnitude of injection rate used by Cheng (2012) is unavailable. Such fundamental differences are the possible causes for differing fracture widths of both edge and center fractures. Moreover, the intention of this study is not to present precise fracture width values but to present relative magnitudes and differences between edge and center fractures.

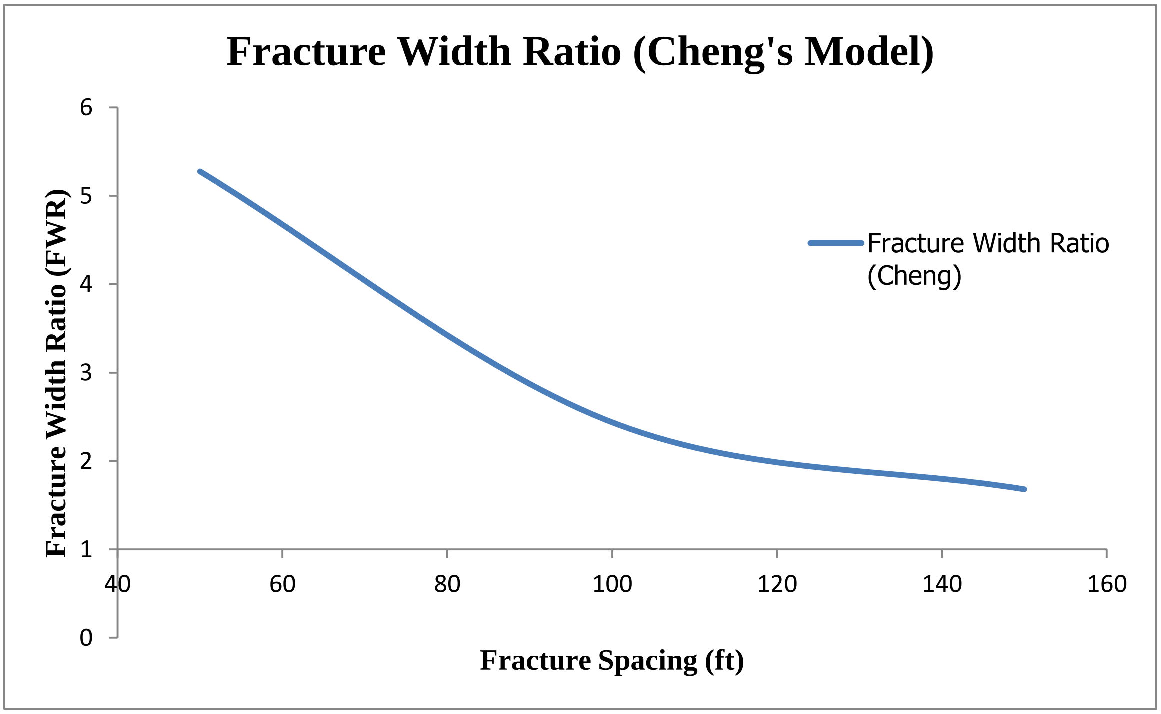

Figure 5.4. Fracture width ratios calculated from results reported in Cheng (2009)

5.2. STRESS ANALYSIS

As reported in Section 4.3, the stress change is highest in and around a fracture depicting the stress interference or stress shadow. The minimum horizontal stress change increases around the fractures particularly between the center fractures. This is because of the stress interference and overlapping of the stress shadows.

The same phenomenon is also reported in another study done by Cheng (2010). The results depict the minimum horizontal stress change on the borehole wall along the borehole that is perpendicular to the fracture planes as shown in Figure 5.5

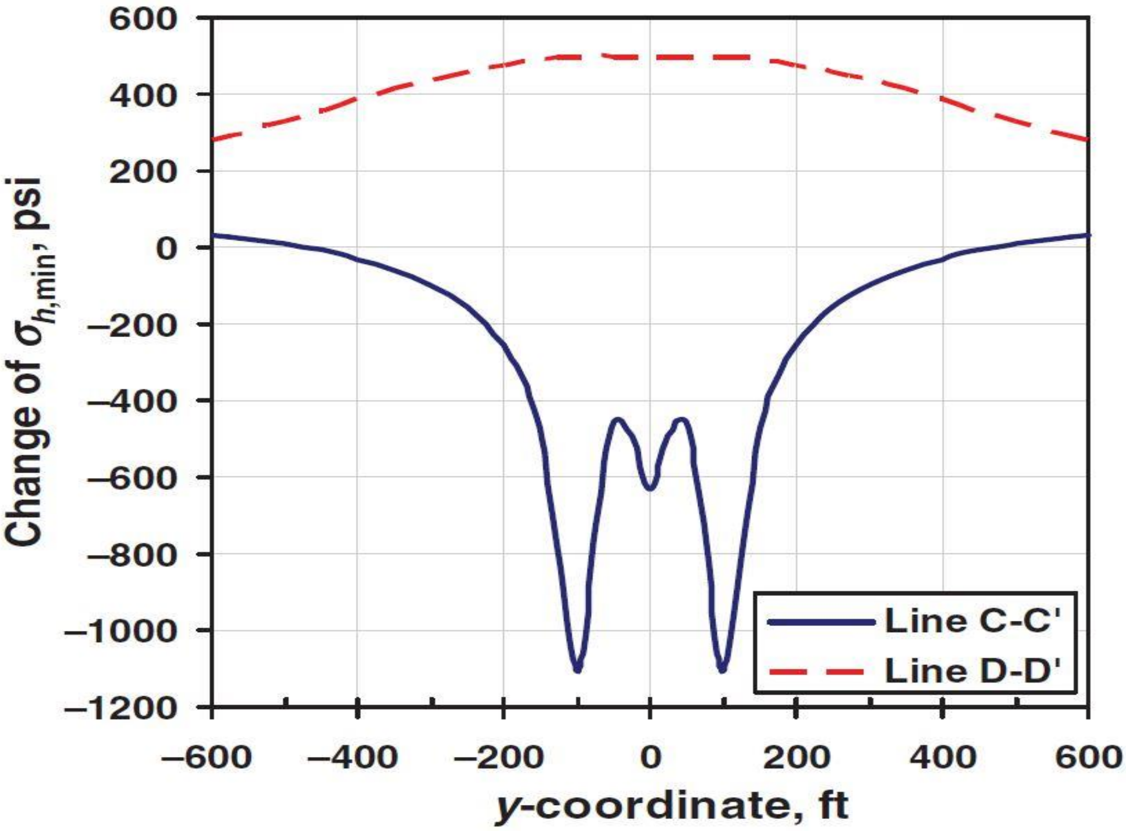

Figure 5.5. Change in minimum horizontal stress at borehole wall and at the tips of fractures as reported by Cheng (2009)

Figure 5.5 depicts minimum horizontal stress change both at the borehole wall and at the fracture tip. Line D-D’ is indicative of stress change at the borehole wall and line C-C’ is indicative of stress change at the fracture tips. The changes in stress at the tips of the fractures show that the stresses are tensile in nature. Stress analysis at fracture tips is beyond the scope of this project. The stress change at the borehole wall follows a similar pattern where the stress change is highest near the center fracture and gradually decreases as the distance from the fractures increases. The stress change results from this study also follow a similar pattern and are shown in Figure 5.6.

This logic is extended to fracture models where more than four fractures are created simultaneously to prove that the stress change is highest and the fracture width is lowest near the innermost fractures (Cheng, 2010).

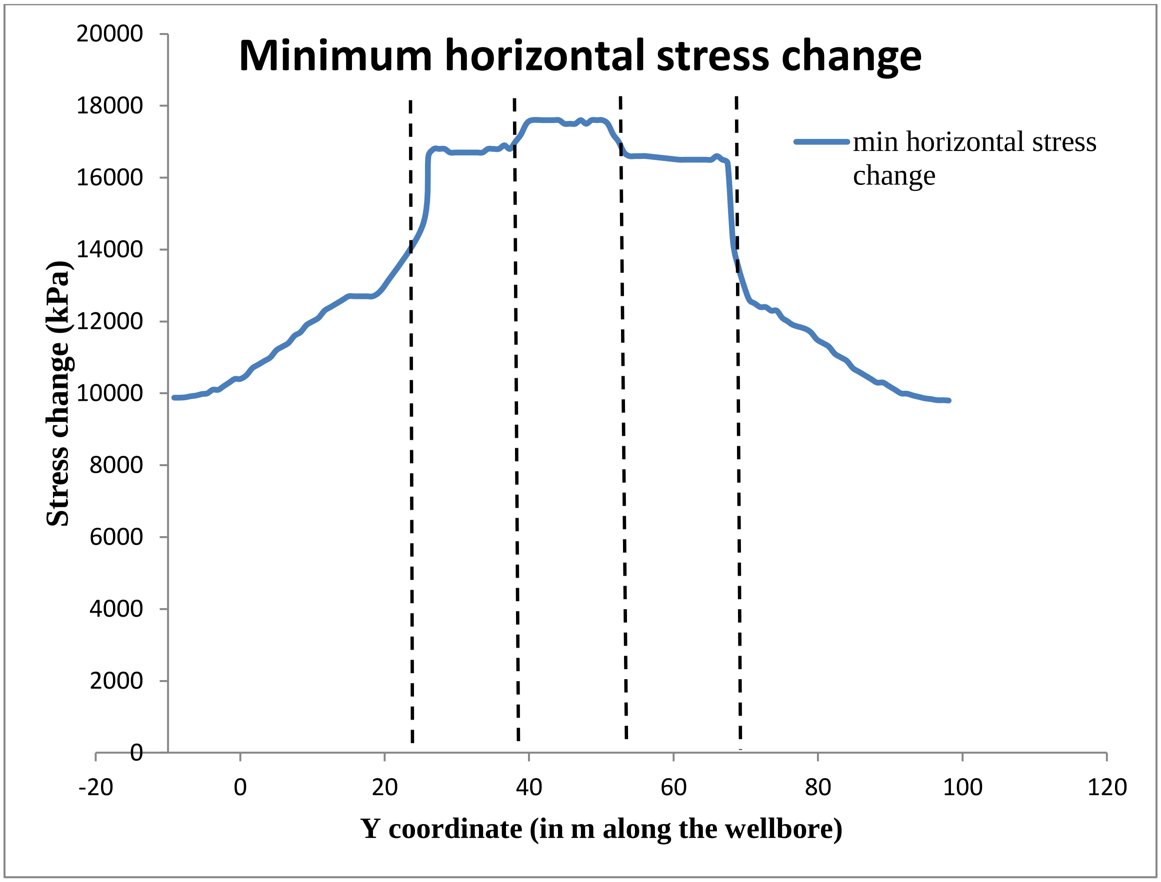

Figure 5.6. Minimum horizontal stress change along the wellbore

The minimum horizontal stress change analysis by Cheng (2009) using a three fracture model with a spacing of 100 ft reported a maximum stress change of 500 psi or 3.45 MPa around the center fracture. Stress analysis in this study, performed on a four fracture model with a spacing of 60 ft, reported a minimum horizontal stress change of 17.5 MPa between the center fractures. Such a huge difference in stress change magnitudes is due to the combined effect of fracture spacing and the number of fractures. In addition to the fractures being well within the stress shadows of its neighbors, presence of four fractures compared to three (Cheng, 2009) enhanced the stress concentrations between the center fractures.

5.3. ANISOTROPY STUDIES

Elastic and permeability anisotropy is inherent to shales due to the laminated structure of its matrix. The horizontal Young's Modulus of shales is higher than its vertical counterpart. Likewise, the vertical permeability is much lower than the horizontal permeability. This is characteristic to all shales irrespective of the type of shale in question. A sensitivity analysis is performed to investigate the effects of anisotropy on the fracture widths

5.3.1. Permeability Anisotropy. The common practice in the industry is to utilize the average reservoir permeability when predicting fracture dimensions or hydrocarbon production. This study was included to observe the fracture behavior for the combined effect of multiple fractures and different levels of anisotropy. As mentioned in Section 4.5.2, the average permeability was kept constant at 6md while the ratio of the vertical to horizontal permeability was varied between 1 and 0.1. The individual effect on edge and center fractures is shown in Figure 5.7 while the fracture width ratio (FWR) for different anisotropy levels is shown in Figure 5.8.

The change in FWR is minimal but an interesting observation is that the FWR increases with increasing anisotropy. Given the scale of change in the fracture widths of both edge and center fractures, the level of permeability anisotropy has little effect on fracture apertures. The permeability values chosen for this study are typical of shale formations but do not represent the entire range of permeability values found in shales across the United States.

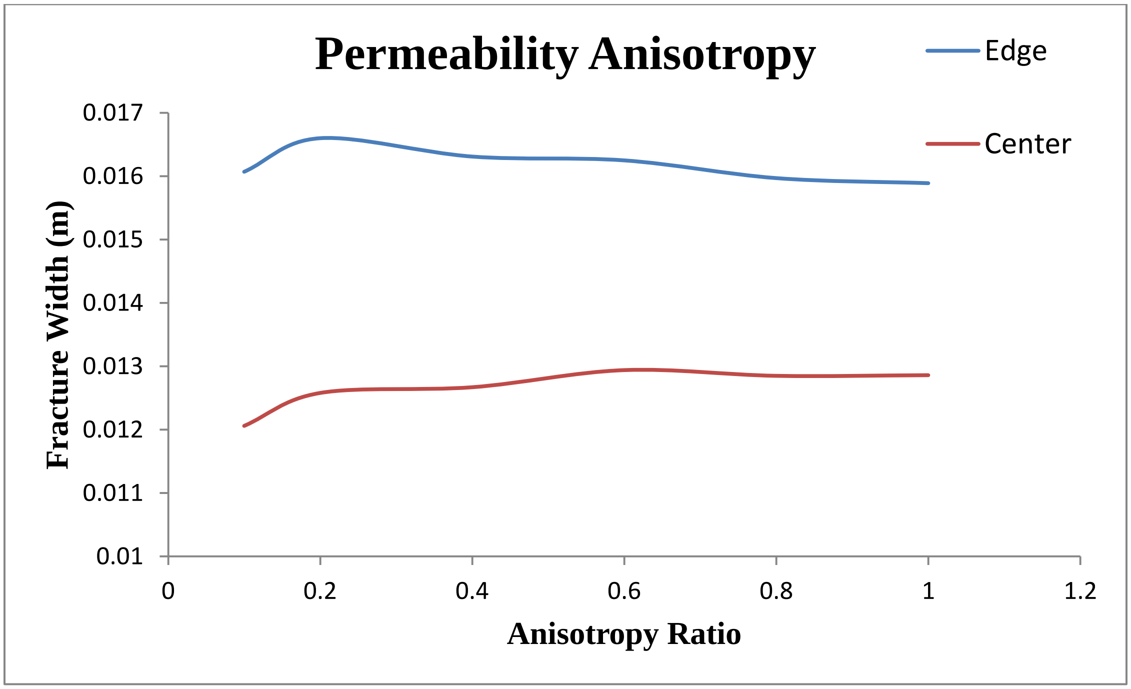

Figure 5.7. Edge and center fractures width variation with permeability anisotropy ratio

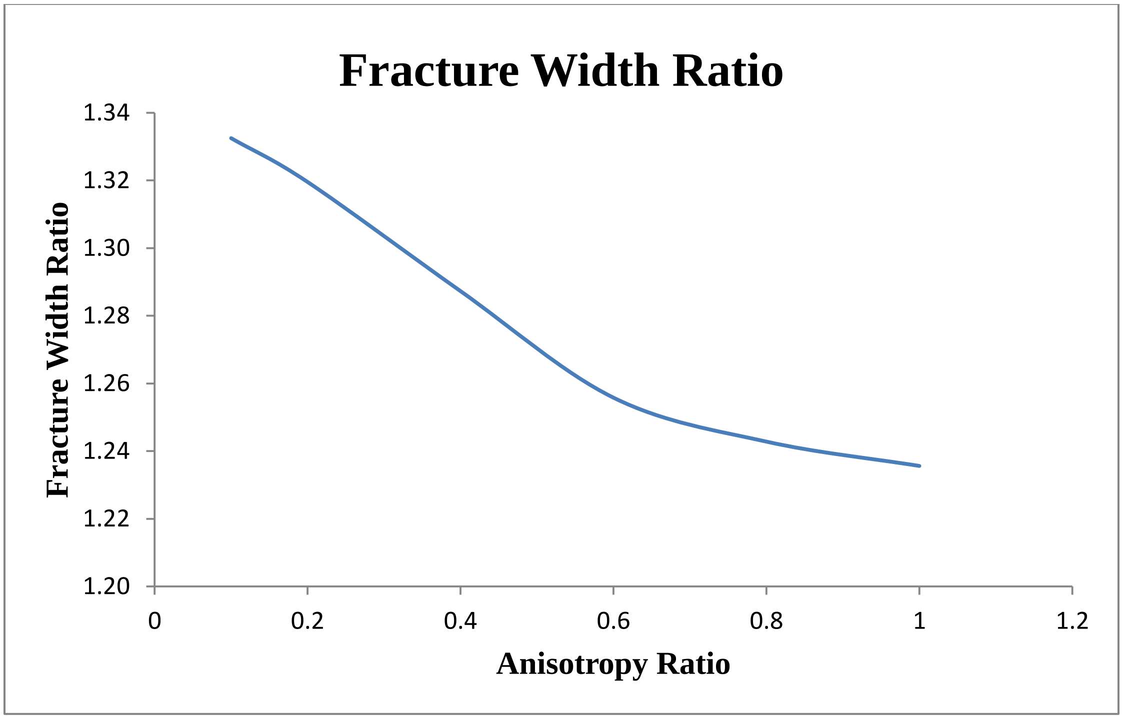

Figure 5.8. Fracture width ratio (FWR) variation with permeability anisotropy ratio

The minimal effect of permeability anisotropy on fracture widths could be due to the fact that the shale in this model was considered to have a very low permeability of 6μd. Therefore, it is premature to conclude that permeability has no effect on fracture apertures for all formations. An extensive study has to be done for a very wide range of permeability to fully understand the relation between permeability and fracture aperture and is outside the scope of this research.

5.3.2. Young's Modulus Anisotropy. Detecting horizontal Young's Modulus to be much higher than vertical Young's Modulus is commonplace for shale formations. Cases where the ratio of horizontal to vertical Young's Modulus is as high as 3.5 are reported (Higgins, 2008). Results from Section 4.5.1 show that this has a substantial effect on fracture widths especially on the center fractures as shown in Figure 5.9.

The widths of fractures when anisotropy in Young's Modulus is prevalent vary significantly when compared to the isotropic models. The width of edge fractures decreases only slightly as the anisotropy level increases, the center fracture widths, however, drop significantly as the anisotropy ratio increase. The widths of center fractures for all anisotropic models are very similar. This shows that predictions based on isotropic assumptions overestimate the fracture widths of center fractures. Developing a fracture treatment plan and selection of proppant assuming isotropy could prove to be ineffective in terms of production and could lead to economic losses. The fracture width ratio (FWR) for Young's Modulus anisotropy is shown in Figure 5.10.

The center fracture widths drop significantly in anisotropic models compared to the isotropic models. For anisotropic ratios higher than 2.0, the change in center fracture widths seem minimal. The drop is consistent for increasing anisotropic ratio up to 2.0. This could be because of the fact that the model was setup as a closed model with no fluid leaking out of it.

The FWR demonstrates that the difference between edge and center fractures increases significantly with increasing Young's Modulus anisotropy. An analytical study by Khan (2012) that proposes that isotropic models overestimate the fracture width backs the result as shown Figure 5.11.

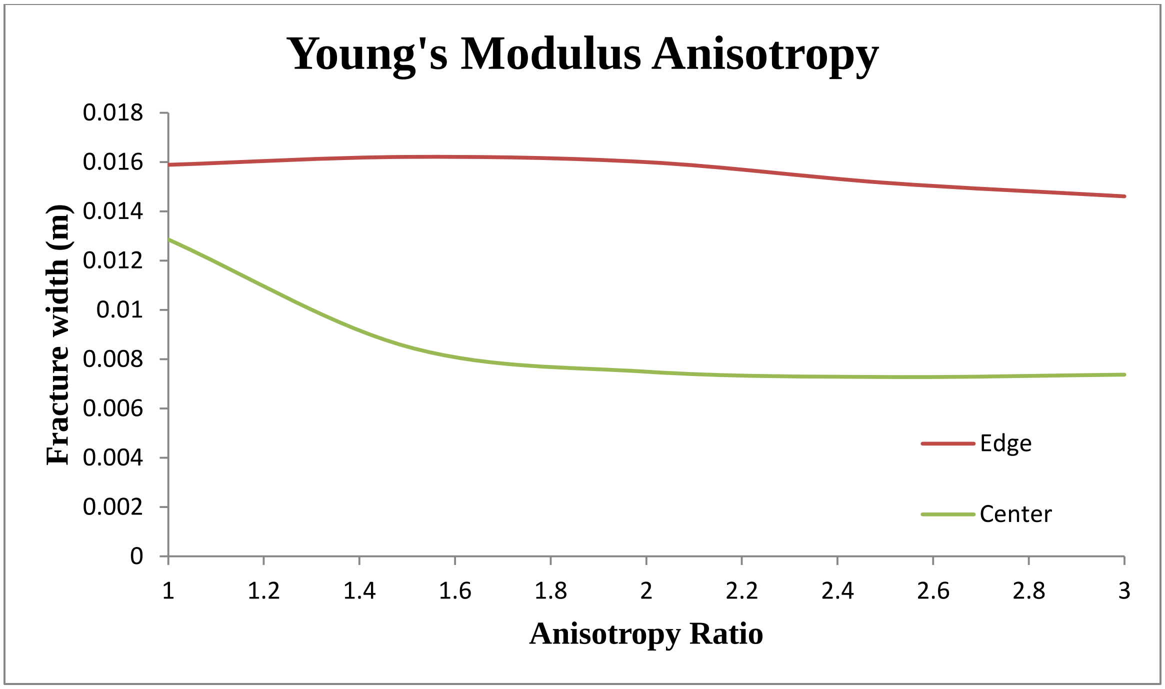

Figure 5.9. Fracture aperture variation with anisotropy of Young's Modulus

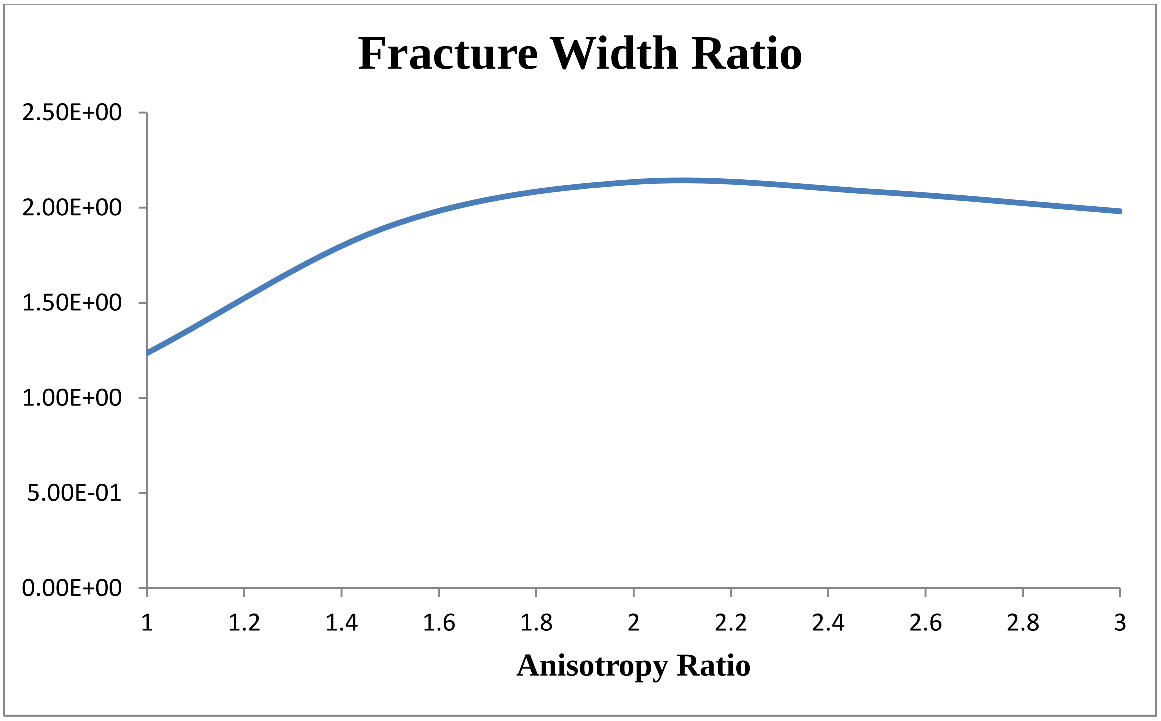

Figure 5.10. Fracture width ratio (FWR) for models with Young's Modulus anisotropy

Another study by Riviera (2011) proposes that the fracture widths solely depend on anisotropic ratios and not the actual magnitudes itself tested. The results presented in Section 4.5.1 contradict the findings as shown in Figure 5.12.

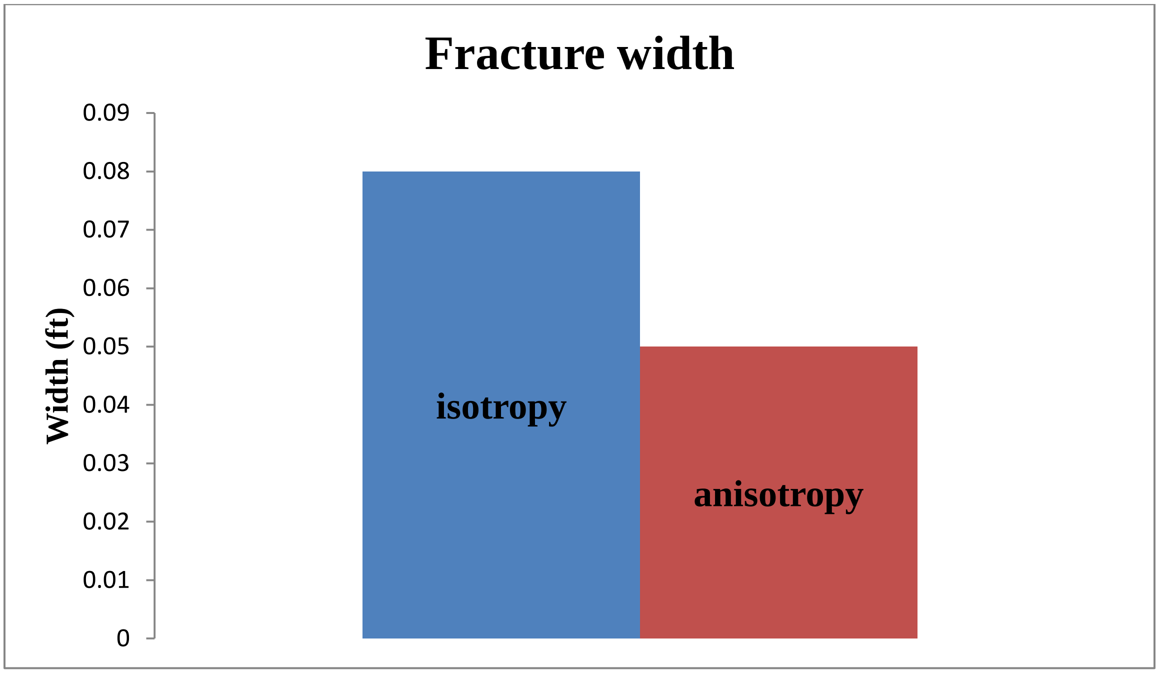

Figure 5.11. Analytical results depicting difference in fracture width of isotropic and anisotropic models (Khan, 2012)

Figure 5.12 suggests that the magnitude of Young's Modulus has a prominent effect on fracture width especially on the edge fracture width while the center fracture width is seemingly unaffected. Since the pump rates are kept constant across all models, the external stress or load applied remains constant. Any deformations caused, in this case it is the opening of the fractures, which will be dependent on the elastic modulus of the deforming material. The numerical results prove that the fracture apertures vary with varying elastic modulus.

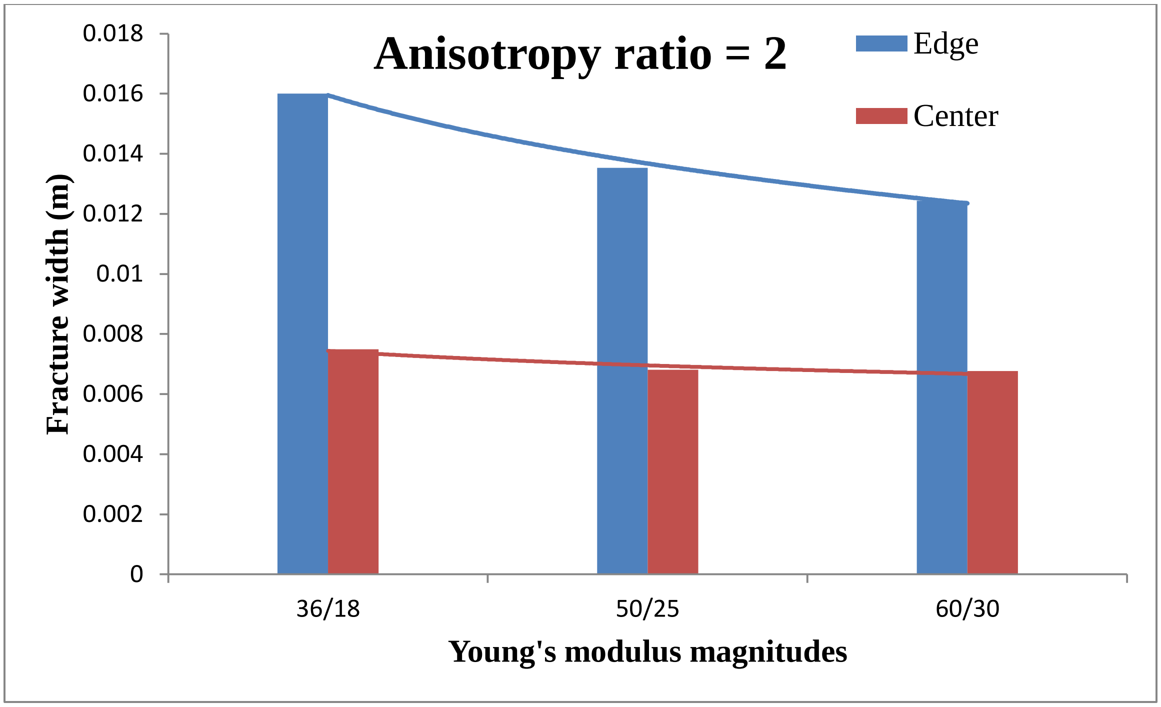

Figure 5.12. Fracture widths of constant anisotropy ratio with varying Young's Modulus magnitudes

5.3.3. Poisson's Ratio Anisotropy. Poisson's ratio variation with direction in shales is not very distinguishable. Reported anisotropy levels of vertical to horizontal Poisson's ratio vary between 0.8 and 1.4. The change in Poisson's ratio is taken into account for this study and the results of fracture width variation are presented in Section 4.5.3 and are shown in Figure 5.13.

The edge fracture width remains constant while the center fracture width seems to have higher widths for all anisotropy levels compared to the isotropic model although the magnitudes only differ by approximately 1mm across the entire range of anisotropy included in this study. Poisson's ratio measures the deformation magnitude in transverse direction due to stress applied in the lateral direction.

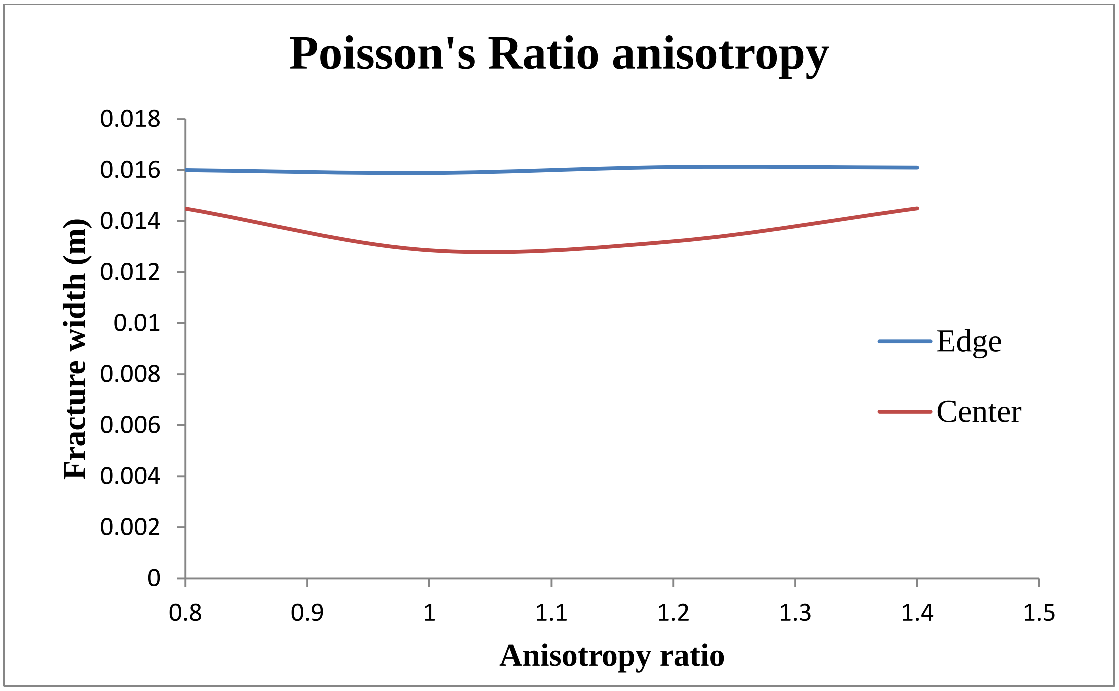

Figure 5.13. Fracture widths variation due to change in Poisson's ratio anisotropy

Hydraulic fracturing is caused by tensile stresses acting normal to the fracture faces. Stresses applied and the resulting deformations are in the normal direction. Change in Poisson’s ratio for rock formations under similar conditions do not affect the hydraulic fracturing process but certainly have a role to play in determining the horizontal stresses for the same overburden.

Since the fractures are created because of stress applied by fracturing fluid normal to the fracturing plane, the Poisson’s ratio change has minimal effect on fracture width. To study the isolated effect of Poisson’s ratio, the Young’s Modulus was kept constant which could also be the reason that the deformation is identical in all cases.

5.3.4. Stress Regime Influence. The state of stress has an important role to play in determining the fracture widths of edge and center fractures. Two additional models were built to analyze the effect. In a uni-axial strain model with constant pore pressure and overburden, the horizontal stresses depend solely on the Poisson’s ratio. Simulation of additional models with a Poisson’s ratio of 0.375 and 0.444 was performed. Due to change in Poisson's ratio, the horizontal stresses acting in the model change but the overburden remains the same in both models resulting in different states of stress. Fracture widths of both models are compared to study the change in both edge and center fractures based on different states of stress. The findings are shown in Table 5.1. Higher Poisson's ratio causes a state of stress with higher magnitudes of horizontal stresses that are extensional in nature. As observed in Table 5.1, fracture widths of both edge and center fractures differ when there is a change in the state of stress. For a state of stress with lower magnitudes of extensional horizontal stresses, the fracture widths increase significantly. The effect on center fractures seems to be more profound compared to the effect on edge fractures.

Table 5.1. Fracture width variation with a change in the state of stress

Poisson's ratio (ν)	Edge fracture width (m)	Center fracture width (m)
0.375	1.224×10^{-2}	9.88×10^{-3}
0.444	1.311×10^{-2}	1.238×10^{-32}

5.4. IMPLICATIONS FOR PRODUCTION AND DESIGN

Since shales have very low permeability, multistage hydraulic fracturing is essential to effectively drain the reservoir and have high hydrocarbon recovery rates. A common perception of the oil industry was that higher recovery can be achieved by increasing the number and density of hydraulic fractures in a horizontal well section. Often each fracture is assumed to have the same fracture width when multiple fractures are created simultaneously. Some of the initial work on the effect of stress shadows, by Fisher (2004) and Cheng (2009), observes that the internal fractures do not have the same fracture width as the edge fractures.

A key aspect to successful hydraulic fracturing is not just creating the fractures but the effective transport of proppant deep into the fracture to ensure the fractures are propped open (Economides, 2005). Understanding the fracture widths of fractures is important during the selection of proppant size. Underestimating the fracture width and choosing an oversized proppant will lead to a pre-mature screen out where higher pump pressures are encountered and the fracture is not effectively propped as well. This will result in lower cumulative production and hydrocarbon recovery. Overestimating the fracture width will ensure an effective proppant placement but will result in lower hydrocarbon recovery compared to an effective proppant placement of the right size (Cheng, 2012).

The key to maximum cumulative production and higher production rates is to create maximum number of effective fractures. A reservoir simulation study by Cheng (2012) observes that a model with three fractures per stage and a total of ten stages significantly improves production rates, cumulative production and ultimate recovery of a reservoir compared to a model with five fractures per stage and six stages.

Similarly, since shales are inherently anisotropic, a fracture design that considers the effect of stress shadowing but neglects anisotropy could lead to economic losses or an ineffective treatment job. Both anisotropy and fracture spacing have to be considered to accurately estimate fracture width before designing a hydraulic fracture design or choosing a proppant. Since shale properties and the state of stress vary from region to region and also varies depending on the type of shale, a custom hydraulic fracturing design has to be developed depending on the local state of stress and properties encountered. An analysis similar to the one included in this study has to be performed to accurately estimate fracture widths before executing a fracture design job.

5.5. LIMITATIONS AND FUTURE WORK RECOMMENDATIONS

To successfully investigate the relation between fracture width and other parameters in a complex process like the numerical simulation of hydraulic fracturing included in this study, certain assumptions are made. The hydraulic fractures are created and propagated in predefined planes. The fracture growth pattern caused by the stress interference of other fractures is beyond the scope of this study. Studies on the deviation of fractures due to stress interference that cannot be defined in a single plane have been done by many authors (Soliman, 2008; Kresse, 2012). The geometry of the fracture namely the half-length and height are also pre- determined. The intention of this study is to fully investigate the fracture width and the relation between width and fracture spacing.

The numerical models are generated to closely replicate the hydraulic fracturing process within the limitations imposed by the available computational capacity. The maximum fracture width observed is not at the wellbore due to the shortcomings of an otherwise very robust FEA software suite. Fractures in all the models are created with a very low fracture width, but with continuous pumping of fluid, the already created fracture is propped open. Since, a uniaxial strain model was used, the horizontal stresses are at its minimum at the top of the model due to which, maximum fracture width is observed at top of the models.

The analysis of maximum horizontal stress or shear stress around the fractures is beyond the scope of this study and so is the stress analysis near the fracture tips. For this study, fractures run through the entire model domain. A uniaxial strain model was chosen for the entirety of this study. The magnitudes of fracture widths and their variation may change for other stress regimes. Further investigation into the relation of fracture magnitude variation based on anisotropy and fracture spacing needs to be done in other stress regimes. Since shale behavior differs from region to region and since each region is under the influence of a different stress regime, similar analysis has to be done on each shale play to devise a custom reservoir development plan that maximizes the output.

A high performance computing server was used for all simulations involved. 64 processors were kept busy simultaneously using 96 Gb RAM for each simulation. Each simulation lasted 90-140 hours with a few simulations exceeding 5 days of computing.

All parameter magnitudes were chosen to include extreme cases of anisotropy and the magnitudes of parameters themselves. The actual parameter magnitudes encountered in the field may or may not exhibit the entire range of parameter magnitudes involved in this study.

6. CONCLUSIONS

This study investigates the effect of fracture spacing and mechanical parameter anisotropy on fracture widths when fractures are created simultaneously. Numerous finite element models simulating hydraulic fracture propagation have been built to achieve this. The variations in fracture width were studied by varying fracture spacing and the level of anisotropy of different mechanical parameters.

Stress interference or stress shadows affect the fracture widths of both edge and center fractures. Increasing fracture spacing increases the fracture widths of both center and edge fractures. The effect of stress shadows on center fractures is higher compared to the effect on edge fractures. The difference between fracture widths of edge and center fractures decreases with increasing fracture spacing. Multiple fractures enhance the stress shadows around the inner fractures. The maximum stress change in the minimum horizontal stress direction is observed between the center fractures.

Young’s modulus anisotropy has a significant effect on the fracture geometries of the fractures. The edge fractures seem to be relatively insensitive to change in Young’s Modulus anisotropy while the effect on center fractures seems significant. Increasing levels of anisotropy resulted in reduced fracture widths of center fractures. For constant anisotropy levels, increasing Young’s Modulus resulted in decreasing fracture widths for both center and edge fractures. The change in magnitude while keeping the anisotropy ratio constant had a bigger impact on center fractures compared to edge fractures.

Permeability anisotropy ratios were varied within the range of permeabilities observed in shales and seemed to have little impact on fracture width. The effect of Poisson’s ratio anisotropy on fracture widths of both edge and center fractures seemed negligible.

Focus has to be on creating more number of effective fractures during multi stage hydraulic fracturing because increasing the number of fractures does not necessarily mean increased production. Anisotropy and stress shadow effects have to be considered when estimating fracture width and choosing a proppant size to ensure maximum production rates and recovery rates. Fracture design must be optimized by taking the fracture widths of both edge and center fractures into account.

BIBLIOGRAPHY

[1] Abass, H.H., Hedayati, S., Meadows, D.L. 1996. Nonplanar Fracture Propagation From a Horizontal Wellbore: Experimental study. *SPE Production and Facilities*, August, pp. 133-137.

[2] Aboaba, A., Cheng, Y. 2010. Estimation of Fracture Properties For a Horizontal Well with Multiple Hydraulic Fractures in Gas shale. SPE Eastern Regional Meeting, Morgantown, WV, 12-14 October.

[3] Anderson, T.L. 1995. *Fracture Mechanics*. 2nd ed. Florida, CRC Press.

[4] Britt, L.K., Jones, J.R. 2009. *Design and Appraisal of Hydraulic Fractures.* Texas, Society of Petroleum Engineers.

[5] Cauchy. 1827. De la pression ou tension dans un corps solide, [On the pressure or tension in a solid body], *Exercices de Mathématiques*, vol. 2, pp. 42.

[6] Cheng, Y. 2009. Boundary Element Analysis of the Stress Distribution Around Multiple Fractures: Implications for the Spacing of Perforation Clusters of Hydraulically Fractured Horizontal Wells. SPE Eastern Regional Meeting, Charleston, WV, 23-25 September.

[7] Cheng, Y. 2012. Mechanical Interaction of Multiple Fractures—Exploring Impacts of the Selection of the Spacing/Number of Perforation Clusters on Horizontal Shale-Gas Wells. *SPE Journal*, December: pp. 992-1001.

[8] Dassault Systèmes, 2011. ABAQUS® User Manual (version 6.11). SIMULIA, a division of Dassault Systèmes, Providence, Rhode Island.

[9] Desai, C.S., Abel. J.F. 1973. *Introduction to the Finite Element Method*. New York: Van Nostrand Reinhold Publishers.

[10] Economides, M.J., Martin, T. 2007. Modern Fracturing: Enhancing Natural Gas Production. Houston, TX, *Energy Tribune*, Chapters 11-12.

[11] Fisher, M. K., Hienze, J. R., Harris, C. D., Davidson, B. M., Wright, C. A. 2004. Optimizing Horizontal Completion Techniques in the Barett Shale Using Microseismic Facture Mapping. *SPE ATCE*, Houston, 26-29 September.

[12] Fjaer, E., R.M. Holt, P. Horsrud, A.M. Raaen and R. Risnes. 1992. *Petroleum Related Rock Mechanics.*. 2nd ed. New York: Elsevier B.V.

[13] Gatens, J.M., Lee, W.J., Hopkins, C.W. 1991. The Effect of Permeability Anisotropy on the Evaluation and Design of Hydraulic Fracture Treatments and Well Performance. *SPE Gas Technology Symposium*, Houston, TX, 22-24 January.

[14] Green, A.E., Sneddon, I.N. 1950. The Distribution of Stress in the Neighborhood of a Flat Elliptical Crack in an Elastic Solid. *Mathematical Proceedings of the Cambridge Philosophical Society* 46 (1): pp. 159-163.

[15] Griffith, A.A. 1920. The Phenomenon of Rupture and Flow in Solids. *Philosophical Transaction*, Series A, Vol. 221, pp. 163-198.

[16] Higgins, S., Goodwin, S., Donald, A. 2008. Anisotropic Models Improve Completion Design in the Baxter Shale. *SPE ATCE*, Denver, CO, September 21-24.

[17] Holditch, S.A., Tschirhart, N.R. 2005. Optimal Stimulation Treatments in Tight Gas Sands. *SPE ATCE*, Dallas, TX, 9-12 October.

[18] Irwin, G. R., 1957. Analysis of Stresses and Strains near the End of a Crack Traversing a Plate. *Journal of Applied Mechanics*, pp. 361-364.

[19] Jaeger, J. C. & Cook, N. G. W, Fundamentals of Rock Mechanics. Chapman and Hall, London, 1979.

[20] Khan, S., Williams, R., Ansari, S., Khosravi, N. 2012. Impact of Mechanical Anisotropy on Design of Hydraulic Fracturing in Shales. *Abu Dhabi Intl. Pet. Conf. and Exhibition*, Abu Dhabi, UAE, 11-14 November.

[21] Kirsch, G. 1898. Die Theorie der Elastizitaet und die Beduerfnisse der Festigkeitslehre. *Zeitschrift des Vereines Deutscher Ingenieure.* 42: 707.

[22] Kresse, O., Weng, X., Wu, R., Gu, H. 2012. Numerical Modeling of Hydraulic Fractures Interaction in Complex Naturally Fractures Formations. 46th U.S. Rock Mechanics/Geomechanics Symposium, Chicago, IL, 24 – 27 June.

[23] Mehdi Rafiee, Soliman, M.Y., Pirayesh, E., Meybodi, H.E. 2012. Geomechanical Considerations in Hydraulic Fracturing Designs. *SPE Canadian Unconventional Resources Conference,* Calgary, Alberta, Canada 30 October – 1 November.

[24] Meyers, B. Bazan, L.W., Jacot, R.H., Lattibeaudiere, G. 2010. Optimization of Multiple Transverse Hydraulic Fractures in Horizontal Wellbores. *SPE Unconventional Gas Conference*, Pittsburgh, PA, 23-25 February.

[25] Mohr,O . 1914. Abhandlungen aus dem Gebiete der Technische Mechanik [Treatise on Topics in Engineering Mechanics],2nd ed.,Er nst und Sohn,Berlin.

[26] Molenaar, M.M., Hill, D.J., Fidan, E. 2012. First Downhole Application of Distributed Acoustic Sensing for Hydraulic-Fracturing Monitoring and Diagnostics. *SPE Drilling and Completion*, March, pp. 32-38.

[27] Nagel, N., Zhang, F., Sanchez-Nagel, M. 2013. Stress Shadow Evaluations for Completion Design in Unconventional Plays. SPE Unconventional Resources Conference, Alerta, Canada, 5-7 November.

[28] Ozkan, E., Brown, M., Raghavan, R., Kazemi, H. 2011. Comparison of Fractured Horizontal-Well Performance in Tight Sand and Shale Reservoirs. *SPE Reservoir Evaluation & Engineering*. April: pp. 248-259.

[29] Pabon, J., Pistre, V., Kinoshita, T. 2005. A Modular Wireline Sonic Tool for Measurements of 3D (Azimuthal, Radial and Radial Formation Acoustic Properties). SPWLA, New Orleans, LA, 26-29 June.

[30] Sayers, C.M. 2005. Seismic Anisotropy in Shales. *Geophysical Prospecting*, March, pp. 667-676.

[31] Sierra, J., Kaura, J., Gualtieri, D., Sarkar, G. 2008. DTS Monitoring Data of Hydraulic Fracturing: Experience and Lessons Learned. *SPE ATCE*. Denver, CO, 31 October - 2 November.

[32] Soliman, M.Y., East, L. Adams, D. 2008. Geomechanics Aspects of Multiple Fracturing of Horizontal and Vertical Wells. *SPE Drilling and Completion*, September: pp. 217-228.

[33] Soliman, M.Y., Hunt, J.L., Mehdi, A. 2012. Fracturing Horizontal Wells in Gas Reservoirs. *SPE Production*. November: pp. 277-283.

[34] Suarez-Rivera, R., Deendayalu, C. Chertov, M. 2011. Improving Horizontal Completions on Heterogeneous Tight-Shales. *Canadian Unconventional Resources Conference,* Alberta, Canada, 15-17 November.

[35] Warpinski, NormanR. 1991. Hydraulic fracturing in tight fissured media. *JPT*. February: 146-151, pp. 208-209.

[36] Warpinski, N.R., Wolhart, S.L., Wright, C.A. 2004. Analysis and Prediction of Microseismicity Induced by Hydraulic Fracturing. *SPE Journal*, March, pp. 24-33.

[37] Waters, G.A., Lewis, R.E., Bentley, D.C. 2011. The Effect of Mechanical Properties Anisotropy in the Generation of Hydraulic Fractures in Organic Shales. *SPE ATCE*, Denver, CO, 30 October-2 November.

[38] Wei, Y., Economides, M.J. 2005. Transverse Hydraulic Fracture From a Horizontal Well. *SPE Annual Technical Conference*, Dallas, TX , 9-12 October.

[39] Wood, D.B., Junki, II, G. 1970. Stress and Displacement around Hydraulically Fracture Wells. *SPE Annual Fall Meeting*, Houston, TX, 4-7 October.

[40] Yew, C.H., Liu, G.F., 1991, “The Fracture Tip and KIC of a Hydraulically Induced Fracture”, *SPE Production Engineering Journal*, August, pp. 171-177.

[41] Yew, C. 1997. *Mechanics of Hydraulic fracturing*, TX, Gulf Publishing Company.

[42] Zhang, J., W.B. Standifird, K., Adesina, and G. Keaney. 2006. Wellbore Stability with consideration of pore pressure and drilling fluid interactions. In *41st U.S. Symposium on Rock Mechanics, Golden, CO, 17-21 June.*

[43] Zienkiewicz, O. C., R. L. Taylor, and J. Z. Zhu. 2005. The finite element method: its basis and fundamentals. 6th ed. Butterworth-Heinemann.

[44] Zoback, M.D. 2007. *Reservoir Geomechanics* 5th prtg. New York: Cambridge University Press.

VITA

Deepak Varma Gokaraju earned his Bachelor’s degree in Chemical Engineering from Birla Institute of Technology and Science (India) in Spring 2010. He pursued a Master’s degree in Petroleum Engineering at Missouri University of Science and Technology. He was awarded the Master’s Degree in May 2014.